Computational Modelling of Cardiac Function and Myocardial Infarction

James MBewu

Thesis presented for the degree of Master of Science
in the Department of Mathematics and Applied Mathematics

University Of Cape Town

August 2012

Plagiarism Declaration

'I know the meaning of plagiarism and declare that all of the work in the thesis, save for that which is properly acknowledged, is my own':

Signature: .....

Date: .....

Abstract

Cardiovascular disease is a leading cause of death in South Africa [1]. In particular non-fatal myocardial infarction is a key determinant for future cardiac failure due to adverse remodelling and electrophysiological dysfunction [2,3]. Computational modelling of the electrophysiology and mechanics of the heart can provide useful insights into the causes of cardiac failure and the efficacy of treatments designed to combat myocardial infarction.

A computational model of the healthy and infarcted left ventricle of a rat was developed using the eikonal diffusion equation to simulate the electrophysiology [4]; a continuum mechanical model incorporating a passive mechanical model of Usyk to describe the nonlinear, anisotropic and nearly compressible nature of cardiac tissue [5]; and an active stress model of Guccione to model the contraction of cardiac tissue [6]. Boundary conditions modelling the blood pressure on the heart wall were applied to simulate the cardiac cycle.

An idealised geometry of an ellipsoid was used to model the structure of the rat left ventricle. The element-free Galerkin method (EFGM) was used to interpolate functions in the domain [7]. Both the eikonal diffusion equation and mechanics equations were solved using the Newton-Raphson Method. The boundary collocation method for EFGM was used to enforce boundary conditions [8]. The model was implemented within SESKA, parallel in-house mechanics code written in C++. Simulations were run on the Centre for High Performance Computing (CHPC) SUN Cluster using up to 64 cores.

The eikonal diffusion equation was validated and calibrated so that results qualitatively matched experimental results [9, 10]. The healthy mechanical model was validated using data from experimental studies in literature [11–13]. The full cardiac cycle of the healthy rat left ventricle was then simulated with end diastolic volume, end systolic volume and ejection fraction compared well with literature [14–18].

Lastly, a model of the rat left ventricle during the ischaemic phase of myocardial infarction was simulated. An increase in end diastolic volume from the healthy left ventricle was shown as has been found experimentally [19]. Additionally evidence of characteristic over-stretching in the infarcted region during contraction has been shown in the computational model [20].

Acknowledgements

First and foremost I would like to thank my supervisors Prof. Daya Reddy and Dr Sebastian Skatulla for giving me the opportunity to study this interesting and challenging topic. Throughout the past year and a half valuable advice and discussions were integral to this thesis. I would also like to thank all the students and staff at the Centre for Research in Computational and Applied Mechanics, UCT for numerous discussions over cups of coffee.

I am grateful for the funding provided by the National Research Foundation throughout my Masters studies. Opinions expressed and conclusions arrived at are my own and are not necessarily to be attributed to the NRF. I would also like to thank Prof. Reddy and Dr Skatulla for writing numerous reference letters they have written in support of funding.

And last but not least, I would like to especially thank my family for helping me through the final stages of writing this thesis and my dear friends for making life enjoyable and listening to my ramblings on maths and the heart (clearly more related than they previously may have thought).

Contents

List of Figures

List of Tables

Nomenclature

action potential the potential difference across the a biological membrane (mV).

active mechanics mechanical behaviour during contraction of the heart.

active stress a mathematical description of the contribution of the contraction of myocytes to the total stress.

active tension tension developed by the myocyte due to active forces (kPa).

aorta a large artery leaving the left ventricle and sending blood to the rest of the body.

aortic valve a valve separating the left ventricle from the aorta.

apex the bottom tip of the left ventricle.

atria the two smaller cavities of the heart pumping blood to the ventricles.

base the top of the left ventricle near the aortic valve.

branch bundle block when the Purkinje network is damaged and there is asynchronous contraction of the heart.

cell membrane the membrane around the cell separating intracellular from extracellular fluid.

collagen a protein, the main constituent of the extrcellular matrix.

coronary artery artery transporting blood to the heart.

crossbridge connection between actin and myosin proteins that causes contraction.

depolarisation time the time at which a myocyte begins contracting (s).

diastole the phase of the cardiac cycle when ventricles do not contract.

eikonal diffusion equation a mathematical model describing the depolarisation time in the heart.

ejection phase of the cardiac cycle when the ventricles contract and the aortic valve is open.

ejection fraction the ratio of stroke volume to end-diastolic volume.

electrophysiology electro-chemical dynamics of the heart.

element-free Galerkin method a numerical method similar to the finite element method that does not use elements.

end-diastole the end of diastole (before contraction begins).

end-systole the end of systole (before relaxation begins).

endocardium the inner layer of the myocardium.

epicardium the outer layer of the myocardium.

extracellullar pertaining to the outside of a cell.

extracellular matrix the mesh of connective tissue, primarily collagen, that supports myocytes.

fibre directions the average orientations of myocytes in the myocardium.

gap junctions pores connecting adjacent myocytes through which ions are transported.

injection therapy a therapy for myocardial infarction where a gel is injected into the infarcted tissue.

intracellular pertaining to the inside of a cell.

ion channel a channel in a cell through which ions can pass.

ischaemia the first stage of myocardial infarction.

isovolumetric contraction phase of the cardiac cycle when the ventricles contract while valves are closed and the ventricular volume is constant.

isovolumetric relaxation phase of the cardiac cycle when the ventricles relax while valves are closed and the ventricular volume is constant.

mitral valve valve connecting the left atrium and left ventricle.

modified boundary collocation method a method for applying boundary conditions in the element-free Galerkin method.

monodomain equation a mathematical model describing the spatial and temporal evolution of the action potential.

myocardial infarction tissue death usually caused by the restriction or blockage of blood flow from the coronary arteries to a part of the heart tissue.

myocardium the muscle tissue of the heart.

myocyte (cardiomyocyte) specialised muscle cell that is found in the heart.

orthotropic a material that has differing material properties in two or three orthogonal directions.

passive mechanics mechanical behaviour when there is no contraction.

preload the initial pressure applied at the beginning of diastolic filling (kPa).

pressure-volume loop the pressure plotted as a function of volume, forming a closed loop over the cardiac cycle.

propagation speed speed at which the electrical signal is propagated through the myocardium ($mm\,ms^{-1}$).

Purkinje cell a specialised myocyte with high conduction speed.

Purkinje muscle junction (PMJ) connection between a Purkinje cell and the myocardium of the ventricle.

Purkinje network network of Purkinje cells spread over the endocardium of the ventricle.

relaxation time the time from maximum active tension to no active tension (s).

residual stress stresses present within the heart when there is no external traction (pressure) applied.

sarcomere the subcellular contractile unit of the myocyte.

sarcomere length length of the sarcomere (μm).

sarcoplasmic reticulum an intracellular store of calcium ions.

stroke volume the volume of blood ejected during systole (μL).

systole the phase of the cardiac cycle when the left ventricle contracts.

tension development the process by which myocytes contract and develop tension.

transmural through the heart wall.

transversely isotropic where the material behaviour in a certain preferred direction is different from the material behaviour orthogonal to this direction.

ventricle a large cavity of the heart pumping blood to the lungs (right) or rest of the body (left).

Wigger's plot the transient of pressure and volume during the cardiac cycle.

Chapter 1

Introduction

1.1 Introduction

Myocardial infarction refers to tissue death usually caused by the restriction or blockage of blood flow from the coronary arteries to a part of the heart tissue (see Fig. 1.1). This can be due to a build up of plaque in the coronary arteries or a blood clot restricting blood flow to the heart tissue. The part of the heart tissue serviced by the blocked coronary artery dthe body.ies or becomes damaged due to the lack of blood. Although a myocardial infarction is not always fatal, the presence of infarcted tissue causes a reduction in cardiac function and may cause further heart pathologies [2, 3]. Myocardial infarctions affect a large and increasing segment of the population making it of critical importance to develop a better understanding of the effects of myocardial infarction so that effective treatments can be devised [21].

Computational models of the heart can be used to simulate the function and dysfunction of the heart. In order to accurately model the heart it is necessary to take into account a number of subsystems of the heart: the electrophysiology describing the electrochemical dynamics; the active mechanics describing the contraction the body.of myocardium; and the passive mechanics describing the mechanical response of the myocardium to external forces such as blood filling pressure. Computational models bypass ethics procedures needed for human and animal experimental studies and parameters can more easily be changed to represent different physiological conditions. Comprehensive experimental results required to calibrate and validate the mathematical models involved can however

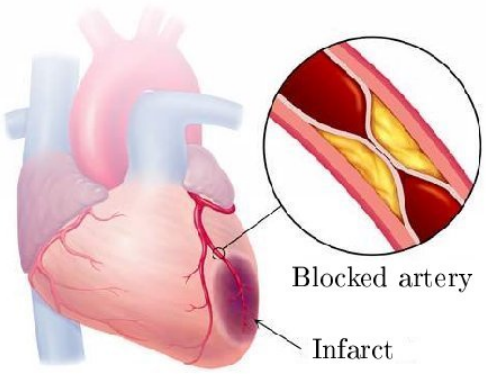

Figure 1.1: Schematic of a myocardial infarction. Adapted from [22].

be difficult to obtain due to the complexity of the models [23]. Once validated with experimental data, computational models can offer unique insight into function and dysfunction, and have the power to test treatments and have been used in clinical settings to optimise treatment [24–29].

Over the past fifty years the field of computational cardiology has developed, together with improved physiological knowledge, through revolutionary experimental techniques such as the voltage clamp and patch clamp techniques [30]. Initial modern work, such as that of Noble [31], described the electrochemical dynamics of a single cell whereas nowadays full electromechanical models of the whole heart based on accurate Magnetic Resonance Imaging (MRI) images can be simulated. With the increase in computing power through parallel computing clusters, computational modelling of the heart has the potential to become highly relevant clinically [32].

Complications resulting from myocardial infarction can be either mechanical (from thinning of the heart wall and reduced pump function to catastrophic rupture of the heart wall) or electrophysiological (such as irregular heart beats). A number of therapies have been designed to treat myocardial infarction that aim to improve the mechanical function of the heart and prevent further loss in cardiac function. These therapies have shown promising results experimentally and computational models of the infarcted heart represent an opportunity to test and optimise treatment [25].

1.2 Cardiac Modelling

1.2.1 The Heart

The heart is located in the thorax between the left and right lungs (see the for the human heart in Fig. 1.2). The function of the heart is to pump oxygen rich blood to the rest of the body supplying it with critical oxygen and nutrients and to pump de-oxygenated blood to the lungs to be oxygenated. The heart is divided into four cavities through which blood passes, the largest being the left ventricle tasked with pumping blood to all parts of the body.

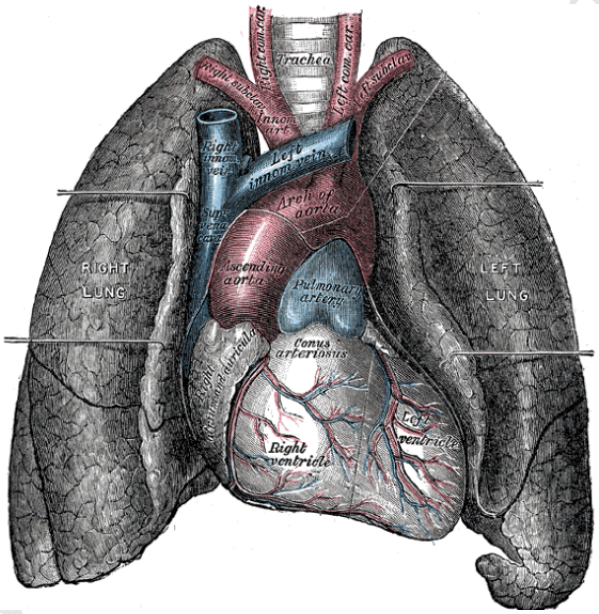

Figure 1.2: Diagram showing the location of the heart between the left and right lungs. Adapted from Sachse [33].

Heart tissue, myocardium, is primarily made up of cardiomyocytes, specialised muscle cells that are found in the heart. Cardiomyocytes contract when an electrical impulse is propagated through the heart and their contraction causes the contraction of the heart and the ejection of blood from the heart into the arteries that lead to the rest of the body. Cardiomyocytes are cylindrical in shape and their ordered arrangement within the myocardium leads to anisotropic macroscopic electrophysiological and mechanical behaviour. This means that material properties of the myocardium are different in different directions depending on

its structure. Since only myocytes in the heart are considered, cardiomyocytes are referred to as myocytes in the remainder of this thesis.

1.2.2 Electrophysiology

The heart contracts due to an electrical impulse that propagates through the heart. This electrical activity is caused by electro-chemical dynamics of ions within each myocyte and changes in ion concentration cause the myocyte to contract. The description of these electro-chemical dynamics constitutes the electrophysiology of the heart. Electrophysiology occurs both at the microscale where ion currents through the cell membrane of each myocyte cause a potential difference across the cell membrane, the action potential, and at the macroscale where the electrical signal propagates throughout the heart.

Myocardial infarction can cause a number of electrophysiological pathologies such as arrhythmias, or irregular heart beats, and branch bundle blocks, where asynchronous contraction of the heart occurs due to abnormal propagation of the electrical impulse [34].

1.2.2.1 Cellular Models

The modern study of cellular electrophysiology has its roots in neuroscience and the mathematical description of the electrophysiology of the squid axon (a nerve cell) developed by Hodgkin and Huxley [35]. Using the revolutionary voltage clamp technique they measured and modelled the role of voltage controlled ion channels in the cell membrane and Hodgkin-Huxley model successfully reproduced the shape and size of the action potential. Noble developed a model of a specialised myocyte, called a Purkinje cell, by adapting the Hodgkin-Huxley model to describe the ion channels of such a cell [31].

The Beeler-Reuter model was developed to describe a mammalian ventricular myocyte [36]. This model extended the ideas of Noble by introducing a variable intracellular calcium concentration, a key player in the contraction of the myocyte. Subsequently, the Luo-Rudy phase-I and the Luo-Rudy phase-II models were developed from the Beeler-Reuter model [37–39]. These models incorporated the effects of abnormal extracellular potassium concentration simulating a number of experimental observations on the periodicity of the action potential and detailed

modelling of the calcium concentration dynamics within the myocyte [40–42]. They have since been used, adapted and reparameterised to recent experimental data by numerous authors [43, 44]. Cellular electrophysiology models have been developed for myocytes from different animals such as mice, rats and dogs [45–47].

1.2.2.2 Propagation Models

The action potential is propagated through the heart from myocyte to myocyte. Ions pass between adjacent myocytes, initiating their action potential. Since the action potential passes from myocyte to myocyte its propagation is highly dependent on the structure of the myocardium. There are a number of ways this propagation has been modelled mathematically. The simplest method being that of cellular automata where the domain is discretised into discrete blocks that stimulate their adjacent blocks [33, 48, 49].

Reaction-diffusion equations such as the bidomain and monodomain equations apply a continuum approach to the propagation of the electrical signal [50, 51]. The bidomain equations incorporate the different anisotropy ratios found in the extracellular and intracellular fluid, whereas the monodomain equation assumes the same anisotropy ratio. Reduced variable reaction-diffusion equations like the Fitzhugh-Nagumo equations can accurately and efficiently describe the propagation of the action potential, but not the shape of the action potential [52].

The eikonal diffusion equation represents a simplification of reaction-diffusion equations [4]. As with the Fitzhugh-Nagumo equations the eikonal diffusion equation accurately and efficiently describes the propagation of the action potential, but not the action potential. The eikonal diffusion equation has been shown to be very accurate in calculating the propagation of the action potential predicted by the more complex reaction-diffusion equations [53].

1.2.3 Mechanics

In addition to myocytes, the myocardium is composed a stiff extracellular matrix mostly containing collagen and the remaining space is filled with extracellular fluid. The constituents of the myocardium are so small (myocytes are of the order $100\mu m$ in length and collagen is a protein on the nanoscale) that it is appropriate to approximate the myocardium as a three dimensional continuum.

Continuum mechanics has been used to model the mechanical deformation of the heart under forces such as blood filling pressure and active contractile forces in the myocardium [54].

1.2.3.1 Passive Mechanics

The passive mechanics of the myocardium constitutes the material behaviour when the heart is not contracting and there are no active forces. Early models of Demiry *et al.* [55] and Janz *et al.* [56] described the mechanics of the myocardium by taking into account the fact that biological tissues deform in a different way from conventional materials such as rubber. Biological soft tissues typically display a non-linear exponential stress-strain relationship first described by Fung [57].

Guccione *et al.* [58] developed a transversely isotropic exponential constitutive law by adapting the strain energy function to take into account the anisotropic nature of the myocardium. A number of authors have adapted this type of constitutive law. Notable examples are the models of Bovendeerd *et al.* [59], Okamoto [60], Kerckhoffs *et al.* [61] and Usyk *et al.* [5].

1.2.3.2 Active Mechanics

Contraction of the heart occurs because individual myocytes contract or shorten. Physiologically, myocytes contract when the intracellular calcium concentration is high enough and there is sufficient energy in the form of the molecule adenosine triphosphate (ATP). This occurs in a different manner to the contraction of skeletal myocytes (e.g. in biceps or triceps).

Mathematical models of this tension development process can describe these cellular processes in detail, taking into account ATP dynamics as well as local intracellular calcium dynamics [62–67]. These models typically involve dozens of equations, whilst being coupled to a cellular electrophysiology model, and are relatively computationally intensive to incorporate into a whole heart model.

Simplified models, such as the models of Guccione *et al.* [6] and Kerckhoffs *et al.* [61], provide models that can be efficiently implemented computationally. These models describe the important qualitative and quantitative features associated with tension development such as length dependence and duration of tension development [68].

There are two approaches to incorporating this into a continuum mechanical model: via the active stress model or the active strain model [69]. The active stress approach, where an additional active stress is added to the existing passive stress, has been used widely together with tension development models to predict mechanics of the contracting heart. Conversely, in the active strain approach, the deformation gradient tensor is multiplicatively split into a prescribed active deformation and an elastic deformation that is to be calculated [70].

1.2.4 Whole Heart Models

Simulations using a wide variety of models and combinations of models have been used to study the heart. The geometry of the heart has been described using idealised geometries such as an ellipsoid to approximate the shape of the left ventricle or more detailed geometries derived from magnetic resonance imaging (MRI) or histological sections of the heart [59, 71, 72].

The eikonal diffusion equation has been coupled to simple active stress models to provide a full electromechanical model of the heart and has been validated in a number of mechanics studies [27, 73, 74]. A number of electromechanical models have been developed to simulate cardiac arrhythmias that can occur after myocardial infarction [75–77]. Walker *et al.* implemented a mechanical model to investigate stress and strain in the infarcted heart [78]. Chabiniok *et al.* validated a biomechanical heart model using animal data with acute myocardial infarction [79].

Cardiac models have also been used to test therapies for myocardial infarction. Wall *et al.* [24] developed a model to describe an injection therapy for myocardial infarction where a gel is injected into and around the infarcted myocardium [80]. Wenk *et al.* [25] extended this by designing a model to optimise the positioning of the injections. Usyk *et al.* [81] used an electromechanical model to show the efficacy of a treatment for myocardial infarction where the ventricles are implanted with pacemakers that control the excitation of the infarcted heart.

1.3 The Cardiac Model

These computational models provide a good basis for the development of an efficient computational model to study myocardial infarction. Key factors that have been incorporated in this model are:

- the fibrous structure of the heart contributing to anisotropy in electrophysiology and mechanics,
- electrophysiological propagation in the heart,
- the characteristic anisotropy in the passive myocardium and,
- a description of the time and length dependency of tension development to analyse temporal changes in mechanics.

The full cardiac model that has been developed can accurately simulate electrophysiological and mechanical function and dysfunction of the rat left ventricle. The rat left ventricle was modelled because therapies are generally tested on animal models first and so this will provide a direct comparison with current experimental research. It was also the animal model used in experiments into injection therapy within the author's research group. The model could be used in future to test treatments for myocardial infarction such as injection therapy.

1.4 Organisation of Thesis

In Chapter 2 the fundamentals of continuum mechanics needed to describe cardiac mechanics are reviewed. The formulation is introduced by describing the kinematic measures used to describe the deformation of the heart and the stress measures needed to relate forces within the heart to deformation are introduced. Finally, the constitutive law for a hyperelastic material is introduced and extended to describe materials with transverse isotropy and orthotropy.

In Chapter 3 the mathematical model of electrophysiology is described. The underlying physiological basis of electrophysiology and the electro-chemical processes involved are introduced first. A description of the fibre directions needed to simulate the anisotropic nature of propagation within the heart is provided. The eikonal diffusion equation to model the propagation of the electric signal in the

heart is introduced. This model is analysed and a number of different numerical solution techniques are discussed.

In Chapter 4 the mechanical model used to describe the deformation of the heart is introduced. The structure and microstructure of the heart and how this affects the mechanics is described. The Usyk model used to model passive mechanical behaviour of the heart is described and residual stresses in the heart discussed. The active stress model of Guccione used to model the active contraction of the heart is introduced and the stretch dependent behaviour of this model is analysed. The boundary conditions controlling the cardiac cycle are then formulated.

In Chapter 5 the complete mathematical formulation and numerical method used to solve the governing equations is developed. The element-free Galerkin method and moving least squares (MLS) shape functions used to interpolate functions over the domain is described. Both the eikonal diffusion equation and mechanics equations were solved using the Newton's method, which requires the tangent stiffness matrix be calculated from the equation's weak form. Computational implementation of the models within SESKA is discussed.

In Chapter 6 the results are presented and discussed. Convergence of the numerical method is confirmed. Next, the electrophysiology model is solved and validated with experimental data and literature. The mechanical model is used to simulate passive mechanical behaviour and validated with pressure volume relationships of experimental results. The full mechanical model is used to simulate the full cardiac cycle of a healthy heart. The results of the healthy model are compared with experimental data. The cardiac cycle is then simulated for an infarcted left ventricle and results compared with experimental data.

In Chapter 7 the key results are summarised and their significance discussed. Recommendations for further development of this cardiac model are discussed.

Chapter 2

Continuum Mechanics

In order to fully describe cardiac mechanics it is necessary to use continuum mechanics. Continuum mechanics is a mathematical formulation used to study the mechanics of deformable materials.

2.1 Kinematics

First the mathematical description of the geometry and its deformation, the kinematics, is described. Let $\mathcal{B} \subset \mathbb{E}(3)$ where $\mathcal{B}$ is a three dimensional manifold defining the material body. Without loss of generality identify the body, $\mathcal{B}$, as the undeformed reference configuration at a fixed time $t = 0$. The undeformed reference configuration corresponds to the configuration of the body under no external forces.

The motion of the body, $\mathcal{B}$, over time, $t \in \mathbb{R}$, is represented by the nonlinear deformation mapping $\boldsymbol{\varphi}_t : \mathcal{B} \to \mathcal{B}_t$ where $\mathcal{B}_t$ is the configuration of the body at time t, the current configuration. It follows that each material coordinate $\mathbf{X} \in \mathcal{B}$ in the reference configuration can be related to its spatial coordinate $\mathbf{x} \in \mathcal{B}_t$ in the current configuration by

$$\mathbf{x} = \boldsymbol{\varphi}_t(\mathbf{X}, t) \tag{2.1}$$

The deformation mapping, $\boldsymbol{\varphi}_t$, has a linear tangent map, which is denoted as the deformation gradient

$$\mathbf{F} := \frac{\partial \boldsymbol{\varphi}_t}{\partial \mathbf{X}} = \frac{\partial \mathbf{x}}{\partial \mathbf{X}} \tag{2.2}$$

or $F_{ij} = {}^{\partial x_i}/_{\partial X_j}$ in index notation, where $i, j = 1, 2, 3$. The Jacobian is defined

Lagrangian Description	Eulerian Description
$\nabla\psi = \frac{\partial\psi}{\partial X_A}\mathbf{e}_A$	$\nabla_t\psi = \frac{\partial\psi}{\partial x_i}\mathbf{e}_i$
$\nabla\mathbf{u} = \frac{\partial u_i}{\partial X_A}\mathbf{e}_i \otimes \mathbf{e}_A$	$\nabla_t\mathbf{v} = \frac{\partial v_i}{\partial x_j}\mathbf{e}_i \otimes \mathbf{e}_j$
$\nabla \cdot \mathbf{u} = \frac{\partial u_i}{\partial X_A}$	$\nabla_t \cdot \mathbf{v} = \frac{\partial v_i}{\partial x_i}$
$\nabla \cdot \mathbf{S} = \frac{\partial S_{AB}}{\partial X_B}\mathbf{e}_A$	$\nabla_t \cdot \boldsymbol{\sigma} = \frac{\partial \sigma_{ij}}{\partial x_j}\mathbf{e}_i$

Table 2.1: Derivative operators in the Lagrangian and Eulerian descriptions. Summation over repeated indices implied.

as $J = \det \mathbf{F}$ and $J > 0$ for an admissible deformation. The displacement as a function of the material coordinates, $\mathbf{u}(\mathbf{X}, t)$, is then defined as $\mathbf{u} = \mathbf{x}(\mathbf{X}, t) - \mathbf{X}$. Basis vectors of the current configuration are denoted by $\mathbf{e}_i$ where $i = 1, 2, 3$ while basis vectors in the reference configuration are denoted by $\mathbf{e}_A$ where $A = 1, 2, 3$.

In the Lagrangian description physical quantities are functions of the material coordinates whereas in the Eulerian description physical quantities are functions of the spatial coordinates. One can distinguish between spatial derivatives with respect to the reference coordinates and derivatives with respect to the current coordinates. The divergence and gradient with respect to the reference coordinates are denoted by an uppercase letter as $\nabla \cdot (\bullet)$ and $\nabla (\bullet)$ respectively. The divergence and gradient with respect to the current coordinates are denoted by using the nabla operator with a t subscript indicating the current configuration as $\nabla_t (\bullet)$ and $\nabla_t (\bullet)$ respectively. A summary of these derivative operators is given in Table 2.1.

An infinitesimal volume element in the current configuration, dv, can be related to the same infinitesimal volume element in the reference configuration, dV, via the expression

$$dv = \det(\mathbf{F})\, dV = J dV. \tag{2.3}$$

Similarly an infinitesimal surface element with normal $\boldsymbol{n}$ in the current configuration, $\boldsymbol{n}da$, can be related to it's infinitesimal surface element with normal $\mathbf{N}$ in the reference configuration, $\mathbf{N}dA$, by Nanson's formula

$$\boldsymbol{n}da = \det(\mathbf{F})\, \mathbf{F}^{-T}\mathbf{N}dA. \tag{2.4}$$

The time derivative of the Jacobian is given by

$$\dot{J} = J\nabla_t \cdot \dot{\mathbf{x}}. \tag{2.5}$$

A number of strain measures can be derived from the deformation gradient tensor. The right Cauchy-Green deformation tensor *or* Cauchy-Green tensor is defined as

$$\mathbf{C} = \mathbf{F}^T\mathbf{F} \tag{2.6}$$

and is $\mathbf{I}$ (the identity tensor) if there is no deformation. The Green-Lagrangian strain tensor *or* Green strain tensor is defined as

$$\mathbf{E} = \frac{1}{2}(\mathbf{C} - \mathbf{I}) \tag{2.7}$$

and is $\mathbf{0}$ (the zero tensor) if there is no deformation.

The stretch is a measure of the strain on a line element in a particular direction. In terms of the Green strain tensor the stretch in the direction $\mathbf{V}$ can be defined as

$$\alpha = \sqrt{\mathbf{C} : (\mathbf{V} \otimes \mathbf{V})} = \sqrt{2\mathbf{E} : (\mathbf{V} \otimes \mathbf{V}) + 1}. \tag{2.8}$$

The material derivative of a quantity is the time rate of change of that quantity as measured by an observer moving with the body. In the Lagrangian description this amounts to the partial derivative with respect to time. For example, in the Lagrangian description, the material derivative of a quantity $P(\mathbf{X}, t)$ is

$$\frac{d}{dt}(P(\mathbf{X}, t)) = \frac{\partial}{\partial t}(P(\mathbf{X}, t)) \tag{2.9}$$

In the Eulerian description the material derivative can be found by applying the chain rule. For example, in the Eulerian description, the material derivative of a quantity $p(\mathbf{x}, t)$ is given by

$$\begin{aligned} \frac{d}{dt}(p(\mathbf{x}, t)) &= \frac{\partial}{\partial t}(p(\mathbf{x}, t)) + \frac{\partial}{\partial \mathbf{x}}(p(\mathbf{x}, t)) \cdot \frac{\partial \mathbf{x}}{\partial t} \\ &= \frac{\partial}{\partial t}(p(\mathbf{x}, t)) + \nabla_t(p(\mathbf{x}, t)) \cdot \mathbf{v} \end{aligned} \tag{2.10}$$

using the chain rule since $\mathbf{x}$ is a function of time. Note the velocity is defined as

$$\mathbf{v} = \frac{\partial \mathbf{x}}{\partial t}. \tag{2.11}$$

2.2 Stress Measures

In continuum mechanics forces within the body are related to deformation via stress measures. Stress is the force per unit area within the body and represents the response of the material to the applied forces. These forces can be body forces, $\mathbf{b}$, which act on the entire body, such as gravity, and traction forces, $\mathbf{t}$, which are forces acting on surfaces on or in a body in a particular direction.

The Cauchy stress tensor $\boldsymbol{\sigma}$ can be defined by applying the Cauchy stress principle. Define a cutting plane through the current configuration of the body. The traction $\mathbf{t}^{(\mathbf{n})}$ on the surface exposed with normal $\mathbf{n}$ is then defined by taking the limit of the force $\Delta\mathbf{f}$ on the surface per area Δa of the surface so that

$$\lim_{\Delta a \to 0} \frac{\Delta \mathbf{f}}{\Delta a} = \frac{d\mathbf{f}}{da} = \mathbf{t}^{(\mathbf{n})}. \tag{2.12}$$

The Cauchy stress tensor at each spatial coordinate can then be defined through

$$\mathbf{t}^{(\mathbf{n})}(\mathbf{x}, t) = \boldsymbol{\sigma}^T(\mathbf{x}, t)\,\mathbf{n}(\mathbf{x}, t) \tag{2.13}$$

where the Cauchy stress tensor is a function of the spatial coordinates and time.

It is useful to define stress measures in the Lagrangian description. In an analogous way to the Cauchy stress tensor, the first Piola-Kirchhoff stress tensor $\mathbf{P}$ is defined through

$$\mathbf{T}^{(\mathbf{N})}(\mathbf{X}, t) = \mathbf{P}(\mathbf{X}, t)\,\mathbf{N}(\mathbf{X}, t) \tag{2.14}$$

where $\mathbf{T}^{(\mathbf{N})}$ is the traction on a cutting plane with normal $\mathbf{N}$ in the reference configuration.

Another stress measure, the second Piola-Kirchhoff stress tensor $\mathbf{S}$, which will be used extensively, is defined as

$$\mathbf{S} = \mathbf{F}^{-1}\mathbf{P} \tag{2.15}$$

Because the differential force $d\mathbf{f}$ on the cutting planes with area da and dA is equal irrespective of the configuration of the body, these stress measures can be related in the following way. The differential force in the Eulerian description can manipulated as

$$d\mathbf{f} = \boldsymbol{\sigma}^T \mathbf{n} da = \boldsymbol{\sigma}^T \det(\mathbf{F}) \mathbf{F}^{-T} \mathbf{N} dA \tag{2.16}$$

where $\mathbf{n}da$ has been expressed in terms of quantities in the reference configuration. In the Lagrangian description

$$d\mathbf{f} = \mathbf{P}\mathbf{N}dA. \tag{2.17}$$

Combining the two equations

$$\boldsymbol{\sigma}^T J \mathbf{F}^{-T} \mathbf{N} dA = \mathbf{P}\mathbf{N}dA \tag{2.18}$$

and noting that $\mathbf{N} \neq \mathbf{0}$ and $dA \neq 0$ leads to an equation relating the Cauchy stress tensor with the first Piola-Kirchhoff stress tensor

$$\mathbf{P} = J\boldsymbol{\sigma}^T \mathbf{F}^{-T} \tag{2.19}$$

and using eq. (2.15) lead to the second Piola-Kirchhoff stress tensor in terms of the Cauchy stress tensor

$$\mathbf{S} = J\mathbf{F}^{-1}\boldsymbol{\sigma}^T \mathbf{F}^{-T}. \tag{2.20}$$

The Cauchy stress tensor and second Piola-Kirchhoff stress tensor are symmetric due to the conservation of angular momentum [82]. This is stated as

$$\boldsymbol{\sigma}^T = \boldsymbol{\sigma} \quad \text{and} \tag{2.21}$$

$$\mathbf{S}^T = \mathbf{S}. \tag{2.22}$$

2.3 Variational Formulation

The variational formulation of continuum mechanics states that the total external work $\mathcal{W}_{ext}$ is equal to the total internal work $\mathcal{W}_{int}$ [82]. The external work corresponds to work done by the external forces such as body forces $\mathbf{b}$ acting over

the volume of the body and traction forces $\mathbf{t}^{(\mathbf{n})}$ acting on the surface of the body.

The internal work is

$$\mathcal{W}_{int} = \int_{\mathcal{B}} \mathbf{S} : \delta\mathbf{E} dV \tag{2.23}$$

where $\delta\mathbf{E}$ is the variation of the Green strain tensor and $\mathbf{S}$ is the second Piola-Kirchhoff stress tensor.

The external work is

$$\mathcal{W}_{ext} = \int_{\mathcal{B}} \rho_0 \mathbf{b} \cdot \delta\mathbf{u} dV + \int_{\partial\mathcal{B}_N} \mathbf{T}^{(\mathbf{N})} \cdot \delta\mathbf{u} dA \tag{2.24}$$

where ρ_0 is the density in the Lagrangian description, $\mathbf{b}$ is the body force, $\mathbf{T}^{(\mathbf{N})}$ is the traction in the Lagrangian description acting on a surface with normal $\mathbf{N}$ and $\delta\mathbf{u}$ is the variation of displacement.

Balancing internal work and external work, the variational statement of strain energy is then

$$\begin{aligned} \delta\Psi &= \mathcal{W}_{int} - \mathcal{W}_{ext} = 0 \\ &= \int_{\mathcal{B}} \mathbf{S} : \delta\mathbf{E} dV - \int_{\mathcal{B}} \rho_0 \mathbf{b} \cdot \delta\mathbf{u} dV - \int_{\partial\mathcal{B}_N} \mathbf{T}^{(\mathbf{N})} \cdot \delta\mathbf{u} dA = 0. \end{aligned} \tag{2.25}$$

It can be shown that the variational formulation of continuum mechanics is equivalent to the equilibrium equation and associated boundary conditions. The equilibrium equation is a statement of Newton's second law in the case of negligible acceleration and is stated as

$$\nabla \cdot (\mathbf{FS}) + \mathbf{b}(\mathbf{X}, t) = \mathbf{0} \quad \text{in } \mathcal{B} \tag{2.26}$$

$$(\mathbf{FS})\,\mathbf{N} = \mathbf{T}^{(\mathbf{N})} \quad \text{on } \partial\mathcal{B}_N \tag{2.27}$$

$$\mathbf{u} = \bar{\mathbf{u}} \quad \text{on } \partial\mathcal{B}_D \tag{2.28}$$

where the first equation is the equilibrium equation, the second expresses the traction force acting on the Neumann boundary and the last equation states the displacement boundary condition on the Dirichlet boundary.

2.4 Constitutive Laws

The stress in the body $\mathcal{B}$ depends on its material properties and the deformation. In most materials when the deformation is small the stress is a linear function of the strain. When the deformation is large however the relation between stress and strain becomes nonlinear. The relationship between stress and strain is called the constitutive law. To describe the deformation of a material the stress is expressed as a function of strain, $\mathbf{S}(\mathbf{E})$. For example, for the Saint Venant-Kirchhoff model is described by the following constitutive law relating stress with strain:

$$\mathbf{S}(\mathbf{E}) = \lambda \mathrm{tr}(\mathbf{E})\mathbf{I} + 2\mu\mathbf{E}, \tag{2.29}$$

where λ and μ are material constants called the Lamé constants [83]. These material constants can be chosen to model a range of materials.

2.4.1 Hyperelastic Materials

If the material body under consideration $\mathcal{B}$ is assumed hyperelastic and homogeneous and possesses an elastic potential Ψ represented by the stored strain energy per unit mass $\psi(\mathbf{E})$ or strain energy function then the second Piola-Kirchhoff stress tensor is given by

$$\mathbf{S} = \frac{\partial \psi}{\partial \mathbf{E}}. \tag{2.30}$$

Many materials from rubber to soft biological tissues can be described by as hyperelastic materials.

2.4.2 Isotropy

It is convenient to define the strain energy function in terms of the principal invariants of $\mathbf{E}$. The principal invariants of a tensor are scalars quantities that remain constant for any coordinate transformation. The second order tensor $\mathbf{E}$ contains three independent invariants

$$I_1 := \mathrm{tr}\mathbf{E} \tag{2.31}$$

$$I_2 := \frac{1}{2}\left[(\mathrm{tr}\mathbf{E})^2 - \mathrm{tr}\left(\mathbf{E}^2\right)\right] \tag{2.32}$$

$$I_3 := \det\mathbf{E} \tag{2.33}$$

All invariants in this thesis are invariants of $\mathbf{E}$.

An isotropic material is a material where the material properties are independent of the direction in which they are measured. Generally, a strain energy function needs to be objective, i.e. invariant under any coordinate transformation. An objective scalar valued tensor function is mostly suitably expressed by the invariants of its tensorial arguments. Specifically, an isotropic strain energy function is described by the three strain invariants. The second Piola-Kirchhoff stress tensor can then be written in the more convenient form

$$\mathbf{S} = \frac{\partial \psi \left(I_1, I_2, I_3\right)}{\partial \mathbf{E}} = \sum_{\alpha=1}^{3} \frac{\partial \psi}{\partial I_\alpha} \frac{\partial I_\alpha}{\partial \mathbf{E}}. \tag{2.34}$$

2.4.3 Transverse Isotropy

Materials that exhibit different material properties depending on the direction in which they are measured are called anisotropic. A special case is transverse isotropy where the material behaviour in a certain preferred direction is different from the material behaviour orthogonal to this direction. Transverse isotropy in material usually occurs due to the microscopic nature of the material.

To mathematically describe transverse isotropy the material direction in the Lagrangian description is introduced and denoted as unit vector $\mathbf{V}_1$. The material tensor of a transversely isotropic material in the Lagrangian description is given by

$$\mathbf{M}_1 = \mathbf{V}_1 \otimes \mathbf{V}_1. \tag{2.35}$$

Consequently, a transversely isotropic strain energy function has as arguments the strain tensor and the material tensor $\mathbf{M}_1$. This requires to include two additional independent invariants two describe transversely isotropic material behaviour. These are

$$I_4 = \mathrm{tr}\left(\mathbf{M}_1 \mathbf{E}\right) \tag{2.36}$$

$$I_5 = \mathrm{tr}\left(\mathbf{M}_1 \mathbf{E}^2\right) \tag{2.37}$$

where the square of a tensor is defined as $\mathbf{E}^2 = \mathbf{E}\mathbf{E}$.

The second Piola Kirchhoff tensor may be expressed as

$$\mathbf{S} = \frac{\partial \psi \left(I_1, I_2, I_3, I_4, I_5 \right)}{\partial \mathbf{E}} = \sum_{\alpha=1}^{5} \frac{\partial \psi}{\partial I_\alpha} \frac{\partial I_\alpha}{\partial \mathbf{E}}. \tag{2.38}$$

2.4.4 Orthotropy

Orthotropy is a generalisation of transverse isotropy. An orthotropic material has differing material properties in two or three orthogonal directions. As in the case for a transversely isotropic material there are three mutually orthogonal material directions $\mathbf{V}_1$, $\mathbf{V}_2$ and $\mathbf{V}_3$ with which we define two additional material tensors. These are

$$\mathbf{M}_2 = \mathbf{V}_2 \otimes \mathbf{V}_2 \tag{2.39}$$

$$\mathbf{M}_3 = \mathbf{V}_3 \otimes \mathbf{V}_3 \tag{2.40}$$

Additionally the following are invariants for an orthotropic material

$$I_6 = \mathrm{tr} \left(\mathbf{M}_2 \mathbf{E} \right) \tag{2.41}$$

$$I_7 = \mathrm{tr} \left(\mathbf{M}_2 \mathbf{E}^2 \right) \tag{2.42}$$

$$I_8 = \mathrm{tr} \left(\mathbf{M_3} \mathbf{E} \right) \tag{2.43}$$

$$I_9 = \mathrm{tr} \left(\mathbf{M}_3 \mathbf{E}^2 \right) \tag{2.44}$$

The Green strain tensor may be expressed in a local coordinate system with basis vectors the material directions

$$\begin{aligned} \mathbf{E} = {} & E_{11} \mathbf{V}_1 \otimes \mathbf{V}_1 + E_{22} \mathbf{V}_2 \otimes \mathbf{V}_2 + E_{33} \mathbf{V}_3 \otimes \mathbf{V}_3 \\ & + E_{12} \left(\mathbf{V}_1 \otimes \mathbf{V}_2 + \mathbf{V}_2 \otimes \mathbf{V}_1 \right) + E_{13} \left(\mathbf{V}_1 \otimes \mathbf{V}_3 + \mathbf{V}_3 \otimes \mathbf{V}_1 \right) \\ & + E_{23} \left(\mathbf{V}_2 \otimes \mathbf{V}_3 + \mathbf{V}_3 \otimes \mathbf{V}_2 \right). \end{aligned} \tag{2.45}$$

where E_{ij} are the components of the local Green strain tensor. The invariants can also be expressed in terms of the coefficients of the local Green strain tensor E_{ij}.

Derivatives of the invariants can be computed as

$$\frac{\partial I_4}{\partial \mathbf{E}} = \mathbf{M}_1, \tag{2.46}$$
$$\frac{\partial I_5}{\partial \mathbf{E}} = \mathbf{M}_1\mathbf{E} + \mathbf{E}\mathbf{M}_1, \tag{2.47}$$
$$\frac{\partial I_6}{\partial \mathbf{E}} = \mathbf{M}_2, \tag{2.48}$$
$$\frac{\partial I_7}{\partial \mathbf{E}} = \mathbf{M}_{icMaterials2}\mathbf{E} + \mathbf{E}\mathbf{M}_2, \tag{2.49}$$
$$\frac{\partial I_8}{\partial \mathbf{E}} = \mathbf{M}_3, \tag{2.50}$$
$$\frac{\partial I_9}{\partial \mathbf{E}} = \mathbf{M}_3\mathbf{E} + \mathbf{E}\mathbf{M}_3. \tag{2.51}$$

Strain energy functions of orthotropic materials are functions of these nine invariants and the second Piola Kirchhoff tensor may be expressed as

$$\mathbf{S} = \frac{\partial \psi \left(I_1, I_2, I_3, I_4, I_5, I_6, I_7, I_8, I_9\right)}{\partial \mathbf{E}} = \sum_{\alpha=1}^{9} \frac{\partial \psi}{\partial I_\alpha} \frac{\partial I_\alpha}{\partial \mathbf{E}}. \tag{2.52}$$

Chapter 3

Electrophysiology

Electrophysiology is the study of the electro-chemical dynamics taking place in the body. This can be signalling between neurons in the brain or our present example of the propagation of an electrical signal between myocytes in the heart. Electrophysiology in the heart occurs both at the cell level where electrically charged ion concentrations fluctuate and at the tissue level where the electrical signal propagates cell-to-cell throughout the myocardium. This classic example of a multiscale problem can be handled by dividing the problem into the microscale problem describing the ion dynamics of a single cell and the macroscale problem describing the propagation of the electrical signal.

It is important to model the electrophysiology of the heart, because it is the chemical dynamics within each myocyte that initiate and modulate the contraction of the myocyte (see Section 4.4.1). The contraction of myocytes causes the heart to contract and eject blood from the heart maintaining the flow of blood throughout the body.

3.1 Cellular Electrophysiology

Each myocyte is enclosed in a semi-permeable cell membrane. The cell membrane separates electrically charged ions such as sodium, calcium, and potassium (Na^+, Ca^{2+} and K^+) found in different concentrations in intracellular fluid, the fluid inside the myocyte, and extracellular fluid that surrounds myocytes [84]. Different ions can pass through their own specific voltage-gated ion channels that are distributed over the cell membrane. Cellular electrophysiology describes the

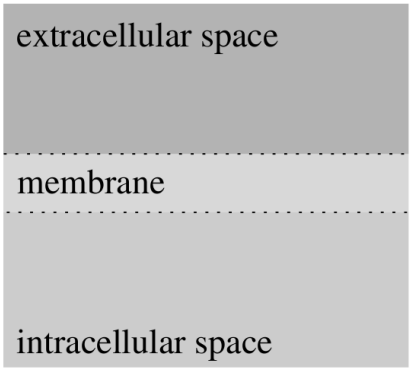

Figure 3.1: Schematic of the extracellular fluid, cell membrane and intracellular fluid [33].

movement of these ions across the cell membrane. The movement of ions across the cell membrane is caused by the potential difference over the cell membrane between the extracellular potential and the intracellular potential [35]. This potential difference is often termed the action potential *or* transmembrane potential.

The potential difference across a cell membrane can be more easily understood by considering the cell membrane as a capacitor-resistor circuit where ions crossing the cell membrane represent a current through the cell membrane since they are moving charges [33]. The relevant biological components in this circuit are the extracellular fluid, the cell membrane and intracellular fluid (see Fig. 3.1).

The intracellular potential is connected to a resistor and a capacitor in parallel representing the ion channels and the impermeability of the rest of the cell membrane and is connected to the extracellular potential (see Fig. 3.2). There is a potential difference driving a current across the resistor and capacitor (i.e. the cell membrane) due to the difference between the electric potentials of the intracellular fluid and the extracellular fluid.

Assuming constant capacitance across the cell membrane the action potential as a function of the current is

$$\frac{dV_m}{dt} = \frac{I_{ion}}{C_m} \tag{3.1}$$

where V_m is the transmembrane potential, C_m is the capacitance and I_{ion} is the current through the cell membrane. Biological membranes have a capacitance of approximately $1\mu F/cm^2$ [85]. The current across the cell membrane, I_{ion}, can be

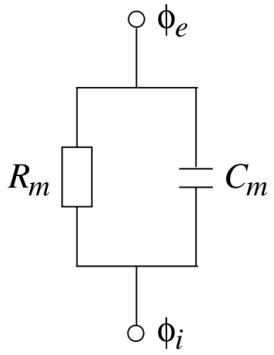

Figure 3.2: Resistor-capacitor cell membrane circuit diagram [33].

represented by adding the contribution of current from each type of ion channel

$$I_{ion} = I_{Na} + I_K + I_L \tag{3.2}$$

where I_{Na} and I_K are sodium and potassium currents and I_L is a summary current combining the contribution from other ionic currents [35]. Each current can in turn be described by an equation that relates the current to the action potential and conductivity of the ion channel. The conductivity itself depends on a number of variables such as the action potential V_m, the density of ion channels and a number of state variables describing the opening and closing of the ion channel.

3.2 The Action Potential

The action potential is an important determinant of electrophysiological and mechanical function. This is because the action potential controls the opening and closing of ion channels, allowing calcium ions to flow into the myocyte, which in turn causes its contraction. The shape of the action potential of a cardiac myocyte varies between different species and different pathologies, however, there are a number of common features present.

Fig. 3.3 shows the action potential of a ventricular myocyte and is representative of most cardiac myocytes. During phase 0 the action potential is at its negative resting potential. During phase 1, the depolarisation phase, there is a sharp upstroke where the action potential rapidly increases due to an influx of Na^+ ions entering the cell. A small stimulus from neighbouring myocytes is

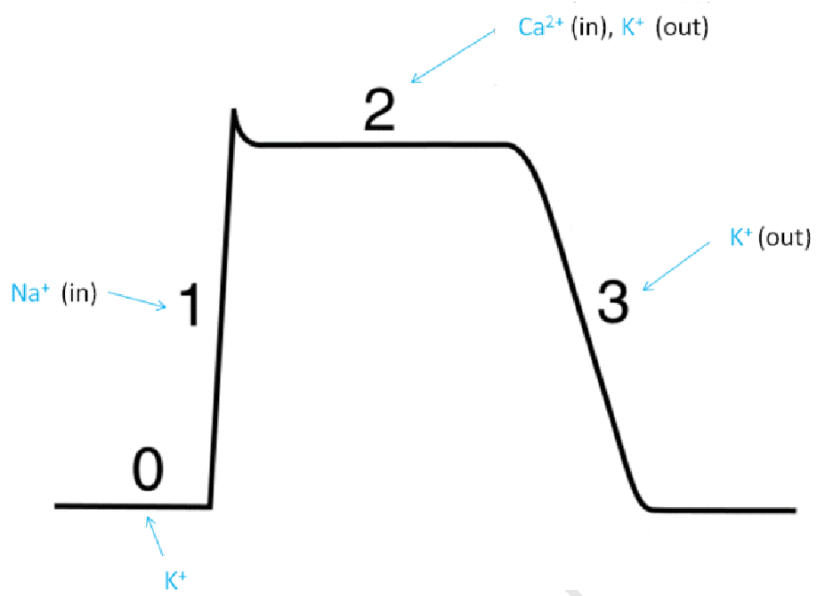

Figure 3.3: Generic shape of myocyte action potential showing major ion species inflow and outflow.

required to activate the first phase of the action potential. During phase 2, the plateau phase, Ca^{2+} ions enter the cell while K^+ ions leave the cell balancing each other out. The increase in intracellular Ca^{2+} causes additional Ca^{2+} ions to be from an intracellular compartment called the sarcomplasmic reticulum. This increase in Ca^{2+} causes the gradual development of tension in the myocyte (contraction). Following the plateau phase is the repolarisation phase, phase 3, where the intracellular K^+ continue to leave the cell and Ca^{2+} returns to the sarcoplasmic reticulum and decreases, causing the tension developed to decrease and the myocyte to relax. Complex cellular electrophysiology models are capable of accurately modelling the action potential shape.

3.3 Propagation in the Heart

The electrical signal is propagated through the heart from cell to cell via inter-cellular gap junctions. If a myocyte is excited (i.e. not at resting potential) then ions will flow into adjacent cells through these gap junctions causing the initiation of the depolarisation phase and of the full action potential. In this way the action potential is propagated throughout the heart and the heart contracts due to the

increase in intracellular calcium ion concentration (see Section 4.4).

3.3.1 Fibre Structure

The structure in which myocytes are arranged in the myocardium has a large effect on the propagation of the action potential. Myocytes, idealistically, are cylindrical in shape with an axis of symmetry corresponding to the direction in which the myocyte contracts. Myocytes are arranged in a tile-like fashion to create sheets two to three myocytes thick. These sheets, or laminae, have a preferred fibre direction in which myocytes are oriented. These sheets constitute the myocardium.

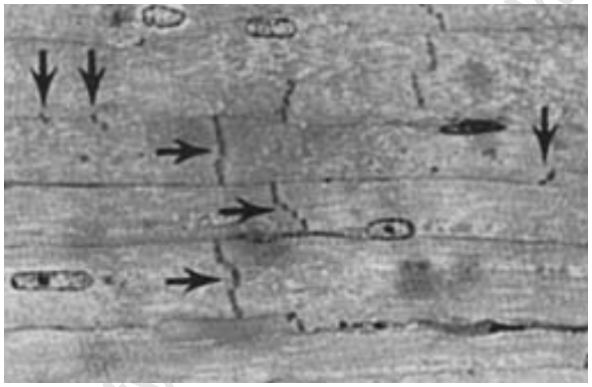

Figure 3.4: Myocytes with labelled gap junctions. Vertical arrows indicate transverse gap junctions and horizontal arrows represent longitudinal gap junctions. Adapted from [86].

Myocytes are electrically connected via gap junctions. Gap junctions can either be oriented longitudinally along the myocyte axis, connecting myocytes end-to-end, or transverse to the myocyte axis, connecting myocytes side-by-side (see Fig. 3.4). There is a higher density of longitudinal gap junctions than transverse gap junctions. This causes the electrical signal to propagate faster in the longitudinal direction (or fibre direction) than the transverse directions [87].

To describe this structure mathematically the fibre direction, sheet tangent direction and sheet normal direction at each point are defined. The fibre direction is a vector, $\mathbf{V}_1$, that points in the direction of the axis of the myocyte. The sheet tangent direction is a vector, $\mathbf{V}_2$, that is tangent to the sheet, but orthogonal to $\mathbf{V}_1$. The sheet normal direction is a vector, $\mathbf{V}_3$, that is normal to the sheet.

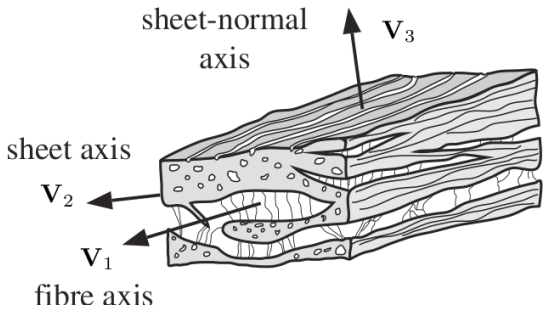

Figure 3.5: Sheet and fibre structure of the myocardium [88].

3.3.2 Conduction System

The conduction of the action potential through the myocardium is aided by specialised myocytes. These specialised myocytes form a conduction system throughout the heart (see Fig. 3.6) [33].

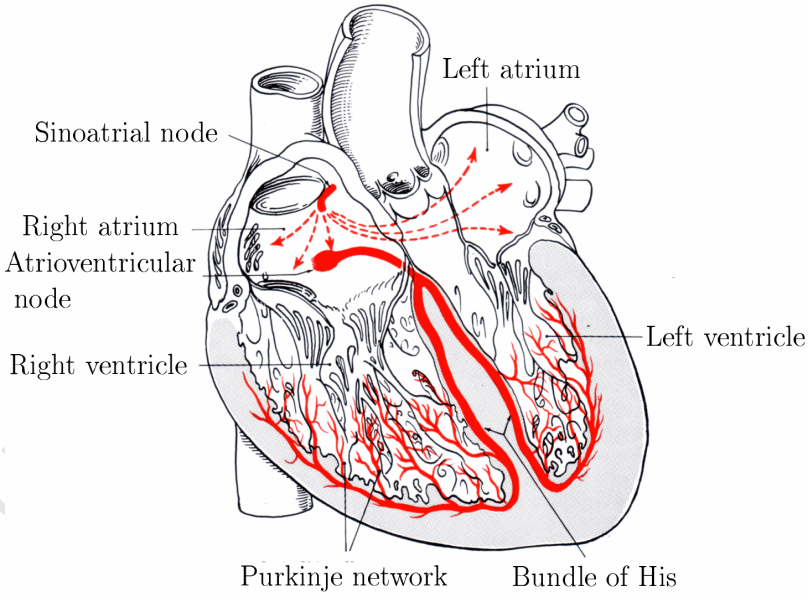

Figure 3.6: Schematic of the conduction system of the heart. Adapted from [89]
.

The sinoatrial node, located at the top of the right atrium initiates the electrical impulse and sends an electrical impulse both throughout the atria and to the atrioventricular node (AV node). There is a delay in propagation at the AV node, allowing the electrical impulse to propagate over the atria and contract before the action potential reaches the ventricles via the Bundle of His.

From the Bundle of His the electrical impulse reaches a fork and separates into the left and right bundle branches of the Purkinje network. The Purkinje network, electrically insulated from the rest of the myocardium, spreads out over the inner wall of the ventricle and penetrates into the myocardium whereupon the electrical impulse is passed to the myocardium via hundreds of Purkinje muscle junctions (PMJs). From the PMJs the electrical signal propagates throughout the ventricular myocardium.

The structure of the conduction system ensures that the electrical signal is propagated fast and reaches different parts of the heart at different times so that the heart contracts in a coordinated fashion. The conduction system also initiates the electrical signal via the pace-making sinoatrial node. The Purkinje network conducts the electrical signal faster than ventricular or atrial myocytes.

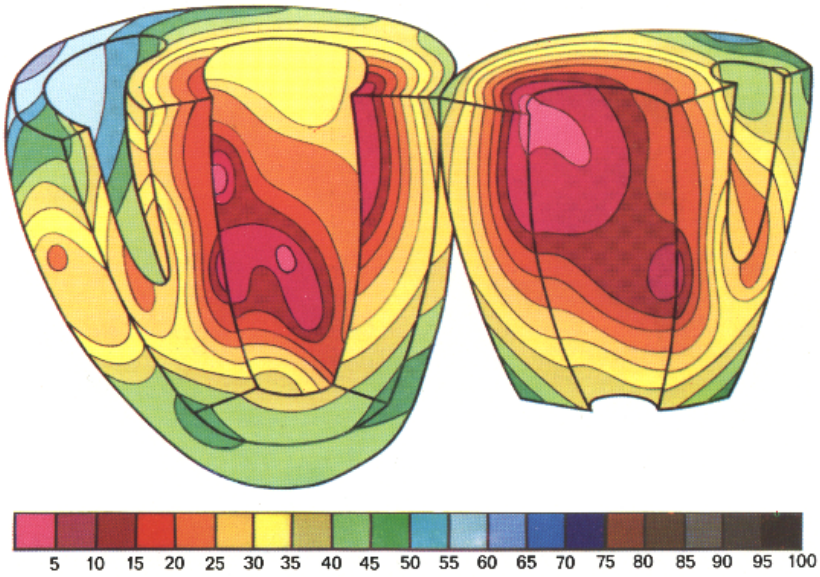

Figure 3.7: Depolarisation times in a human heart. Units are *ms*. Adapted from Durrer *et al.* [9].

The time at which the depolarisation phase occurs at each point in the myocardium is called the depolarisation time. This is important mechanically, because shortly after the depolarisation phase contraction of the myocyte begins. Depolarisation times in the heart have been found experimentally by a number of authors [9,90–92]. Fig. 3.7 shows the depolarisation times for a human heart [9]. Notice how the electrical signal propagates rapidly over the endocardium due to

the fast conducting Purkinje network.

3.3.3 Myocardial Infarction

Following a myocardial infarction the infarcted myocardium shows a gradual decrease in electrophysiological function due to cell death and once dead myocytes are replaced with collagen and a scar forms there is no conduction within the infarcted area. In the initial phase electrophysiological changes are characterised by slower conduction due to decoupling between adjacent myocytes [93]. Once scarring occurs in the infarcted region conduction is very slow, however surviving networks of myocytes may still propagate the action potential [94].

3.4 The Eikonal Diffusion Equation

Partial differential equations can be used to model the propagation and spatial variation of the action potential in the heart. These equations are the monodomain equations (or bidomain equations) and constitute a partial differential equation coupled to a system of ordinary differential equations [95]. These equations however can be computationally expensive to solve. An efficient mathematical model that describes the depolarisation times in the heart is the eikonal diffusion equation. The eikonal diffusion equation is a simplification of the biophysically based monodomain equations. The eikonal diffusion equation can accurately calculate the depolarisation times in the heart, however does not capture the transient nature of the action potential.

The eikonal diffusion equation is given by

$$c_0\sqrt{\nabla u \cdot \mathbf{M}\,\nabla u} - \nabla \cdot (\mathbf{M}\,\nabla u) = \tau_m \,\text{on}\,\Omega \tag{3.3}$$

where u is the depolarisation time, c_0 is the propagation speed of a plane wave, τ_m is a time constant, $\Omega \in \mathbb{R}^3$ is the physical domain over which the equation is solved and $\mathbf{M}$ is the effective coupling tensor

$$\mathbf{M} = \lambda_1 \mathbf{V}_1 \otimes \mathbf{V}_1 + \lambda_2^2 \mathbf{V}_2 \otimes \mathbf{V}_2 + \lambda_3^2 \mathbf{V}_3 \otimes \mathbf{V}_3 \tag{3.4}$$

where $\mathbf{V}_1$, $\mathbf{V}_2$ and $\mathbf{V}_3$ are unit vectors in the directions of the fibre tangent, sheet

tangent and sheet normal respectively and λ_1, λ_2 and λ_3 are the diffusivity in the fibre sheet and normal directions respectively. Note that the effective coupling matrix, $\mathbf{M}$, is symmetric.

The eikonal equation is supplemented with a depolarisation time Dirichlet boundary condition and a no-flux Neumann boundary condition

$$u = 0 \qquad \text{on } \Gamma_D \tag{3.5}$$

$$\mathbf{M}\nabla u = 0 \qquad \text{on } \Gamma_N = \Gamma \setminus \Gamma_D \tag{3.6}$$

where Γ is the boundary of Ω, Γ_D is the Dirichlet boundary corresponding to the initial depolarisation point/s and Γ_N is the Neumann boundary corresponding to a surrounding medium. In the heart the surrounding medium is a conductor, however, it has been shown that this does not affect the depolarisation times [96].

A disadvantage of the eikonal equation is that the solution for the depolarisation times is not deformation dependent. This is because the eikonal equation is solved once on a static domain and is not time dependent like the bidomain equation. This means that mechanoelectric feedback cannot be taken into account. This is of importance when stretch-dependent ion channels play a large role (e.g. in arrhythmias), but otherwise does not play a role in other dysfunctions of the heart (e.g. rupture and remodelling) [97].

The eikonal diffusion equation can be derived from the monodomain equations. The monodomain equations are originally derived by assuming that at each point in the heart there is a current source due to ions passing across the cell membrane. The monodomain equation is given by

$$\frac{\partial V_m}{\partial t} = \frac{1}{C_m \beta}\left[\nabla \cdot \left(\mathbf{D}_m \nabla \left(V_m\right)\right) - \beta\left(I_{ion}\left(V_m, \mathbf{w}\right) + I_s\right)\right] \qquad \text{on } \Omega \tag{3.7}$$

where $V_m\left(\mathbf{x}, t\right)$ is the action potential, $\mathbf{D}_m$ is the mean conductivity tensor describing the anisotropic nature of the tissue, C_m is the capacitance of the cell membrane, β is the membrane surface area per unit volume, I_{ion} is the total current through the cell membrane as calculated by an appropriate cellular model, $\mathbf{w}\left(\mathbf{x}, t\right)$ is a vector of state variables from the cellular model and I_s is an applied stimulus current. The monodomain equation is supplemented with a system of

ODEs for the ionic state variables and with the boundary condition

$$\mathbf{D}_m \nabla (V_m) \cdot \mathbf{n} = 0 \qquad \text{on } \Gamma_N. \tag{3.8}$$

The derivation of the eikonal diffusion equation is achieved by noting that the depolarisation upstroke is similar throughout the heart. This motivates a change of variables so that during the depolarisation phase the action potential is only a function of some new single time variable τ instead of depending on space, $\mathbf{x}$, and time, t. Further define the depolarisation time $u(\mathbf{x})$ to be the time at which the action potential is halfway between its resting value and plateau value. A first order approximation of this equation is then found using a weighted integral method. Implementing this change of variables leads to the eikonal diffusion equation [98].

The corresponding boundary conditions needed to solve the eikonal equation can be found by applying the same change of variables to the monodomain no flux boundary condition.

3.4.1 Analytical Solution to Eikonal Equation

The eikonal equation is a nonlinear steady state scalar PDE over space, the nonlinearity being present in the first term of the equation. Because it is nonlinear, we cannot apply uniqueness and existence theorems that apply to linear equations.

It is not possible to obtain an analytical solution for the general eikonal equation, however for the simple case of an infinite homogeneous domain with a single excitation point at the origin (without loss of generality this can be at any point in the infinite domain) it is possible to find an analytical solution [98]. This solution can be written in terms of the dimensionless distance from the origin, R, which is given by

$$R \equiv \sqrt{\mathbf{X} \cdot \mathbf{M}^{-1} \mathbf{X}}. \tag{3.9}$$

This quantity is dimensionless since $\mathbf{M}^{-1}$ has dimensions L^{-2} (where L is the length dimension) and $\mathbf{X}$ has dimensions L. The solution is given as

$$\frac{u}{\tau_m} = \frac{R}{c_0} + \frac{2}{c_0^2} \ln (c_0 R) - \frac{2}{c_0^3 R}. \tag{3.10}$$

This solution represents ellipsoidal wavefronts propagating from the origin.

This can be seen by noting that each value of R corresponds to an ellipsoid and for each value of R there is a unique u value. The dimensionless speed, $\left(\frac{1}{\tau_m}\frac{\partial u}{\partial R}\right)^{-1}$, can be found to be

$$\left(\frac{1}{\tau_m}\frac{\partial u}{\partial R}\right)^{-1} = c_0 \frac{R^2}{R^2 + \frac{2}{c_0}R + \frac{2}{c_0^2}} \tag{3.11}$$

which indicates that for large values of R (i.e. far away from the excitation point) the wavefront moves at a velocity c_0. This is as expected since c_0 has the interpretation as the dimensionless propagation speed of a plane wave without curvature effects.

For an isotropic plane wave, i.e. when curvature effects are neglected, the propagation speed is $c = {}^{c_0}/_{\tau_m}$. When there is anisotropy the plane wave propagates at different speeds in different directions. The propagation speed in the fibre direction is

$$c_f = \frac{c_0 \lambda_1}{\tau_m} \tag{3.12}$$

and similarly the propagation speeds in the sheet tangent and sheet normal directions are $c_s = {}^{c_0\lambda_2}/_{\tau_m}$ and $c_n = {}^{c_0\lambda_3}/_{\tau_m}$ respectively.

3.4.2 Numerical Solution

Unfortunately, an infinite homogeneous domain does not provide a good approximation to the heart, so numerical methods will be used to solve the eikonal diffusion equation. Being a nonlinear equation it is appropriate to use the Newton Raphson method to solve the eikonal diffusion equation (described in Section 5.1.5).

3.4.2.1 Numerical Continuation

The Newton Raphson method requires as an initial guess a solution that is close to the actual solution. Considering the eikonal equation, it is not known what the solution looks like for a given domain. What is known is the solution to the linear part of the eikonal equation, that is

$$\nabla \cdot (\mathbf{M} \nabla u) = 0 \tag{3.13}$$

which corresponds to the eikonal equation with c_0 and τ_m set to zero. This solution should be close to the solution of the eikonal equation with small c_0 and τ_m. A loading factor λ_n at calculation step n is introduced that multiplies the constants as $\lambda_n c_0$ and $\lambda_n \tau_m$. In this way the linear equation is first solved, then this solution together with Newton Raphson is used to find the solution of the eikonal equation for a small loading increment $\Delta\lambda_n$. This is repeated using the solution from the previous calculation step incrementally increasing λ_n with each step. This procedure is repeated until $\lambda_n = 1$ and c_0 and τ_m are at their desired values. This method is called numerical continuation [99].

3.4.2.2 Stability

Numerical instability can occur in numerical solution of the eikonal diffusion equation due to the nonlinear term. One way to prevent this instability is to approximate the solution with high accuracy near the boundary. This can be done by using a finer discretisation, using higher order elements or upwinding schemes [100]. This, however, uses more computational resources or would require fundamental changes in a numerical code. It was found in this study that for physiological parameters the nonlinear term was sufficiently small to simulate the eikonal diffusion equation efficiently without implementing these methods.

3.4.2.3 Conduction Network

The fast conducting Purkinje network that spreads over the endocardium and penetrates into the myocardium is simulated by increasing the propagation speed in a thin region near the endocardium [61, 101]. The conduction speed increase was calibrated so that the simulated depolarisation time map qualitatively matched the spatial distribution in the experimental depolarisation time map of Durrer [9], while the propagation speed correspoded well to experimental results of propagation speed in rats [102]. This was required as, to the author's knowledge, no experimental spatial depolarisation time data is available for rats.

Chapter 4

Cardiac Mechanics

Cardiac mechanics describes the deformation and forces within the heart. Throughout the cardiac cycle the heart undergoes large deformation due to a number of different forces including a pressure from the blood acting on the inside of the cavity and active forces due to the contraction of myocytes. The suitable mathematical formulation of continuum mechanics has been presented in the preceding chapter and will be used throughout this description of cardiac mechanics.

Once the constitutive laws describing the mechanics have been described, the geometry within which they act is defined. The rat left ventricle has been chosen to be modelled and a truncated ellipsoid approximates its shape well. The mapping of fibre directions describing the anisotropy of the myocardium is then described.

However, before seeking to model the mechanics of the heart it is important to understand the structure of the heart. The gross morphology of the heart is first described as well as details of the microscopic structure of myocardium and its constituents. For further details the reader is referred to Sachse [33].

4.1 Heart Structure

Within the heart there are four main cavities through which blood passes. These are the left and right atria and the left and right ventricles (see Fig. 4.1). The ventricles are larger than the atria as they pump blood out of the heart to the body and lungs whereas the atria pump blood into the ventricles via valves. The left ventricle is the largest cavity and the focus of this study. The walls of the

left ventricle are formed from muscular myocardium with the outer layer termed the epicardium and the inner layer the endocardium. The muscle tissue between the epicardium and endocardium is called the midwall. The bottom tip of the left ventricle is called the apex, while top of the left ventricle is near the base of the heart, not to be confused with the bottom.

Controlling blood passed from the left atrium to the left ventricle is the mitral valve. A large artery, the aorta, leaves the left ventricle and sends blood to the rest of the body. Separating the left ventricle and the aorta is the aortic valve, which opens once the blood pressure in the ventricle rises above the blood pressure in the aorta.

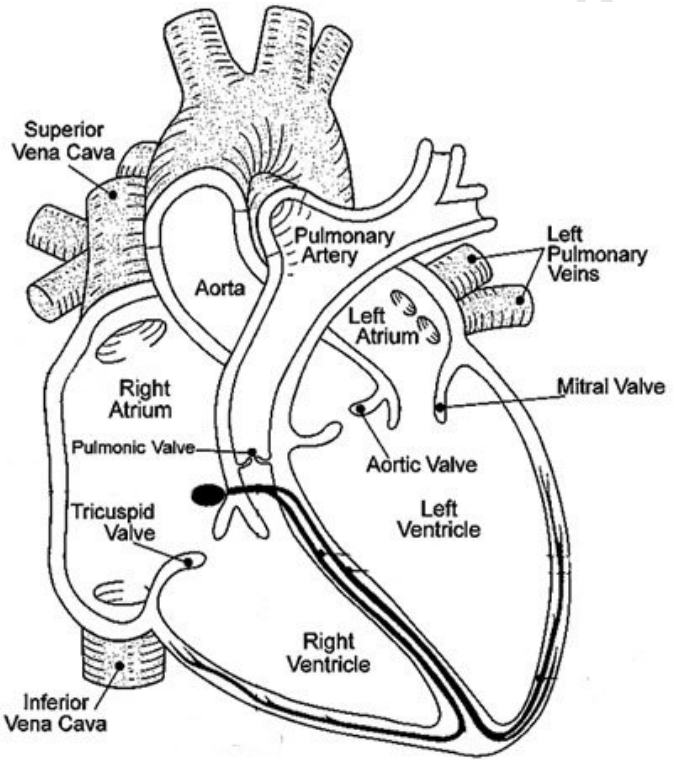

Figure 4.1: Schematic of the macrostructure of the heart. Adapted from [103].

4.1.1 Myocytes

Myocytes are irregular cylindrical cells with a length of between $50 - 120\mu m$ and a diameter of $5 - 25\mu m$. Myocytes are enclosed by a cell membrane, or sarcolemma, $3 - 5nm$ thick, which separates the extracellular and intracellular

spaces (see Fig. 4.2). Intracellular space contains the nucleus, sarcoplasmic reticulum, mitochondria, myofibrils, the cytoskeleton and is filled with aqueous cytoplasm.

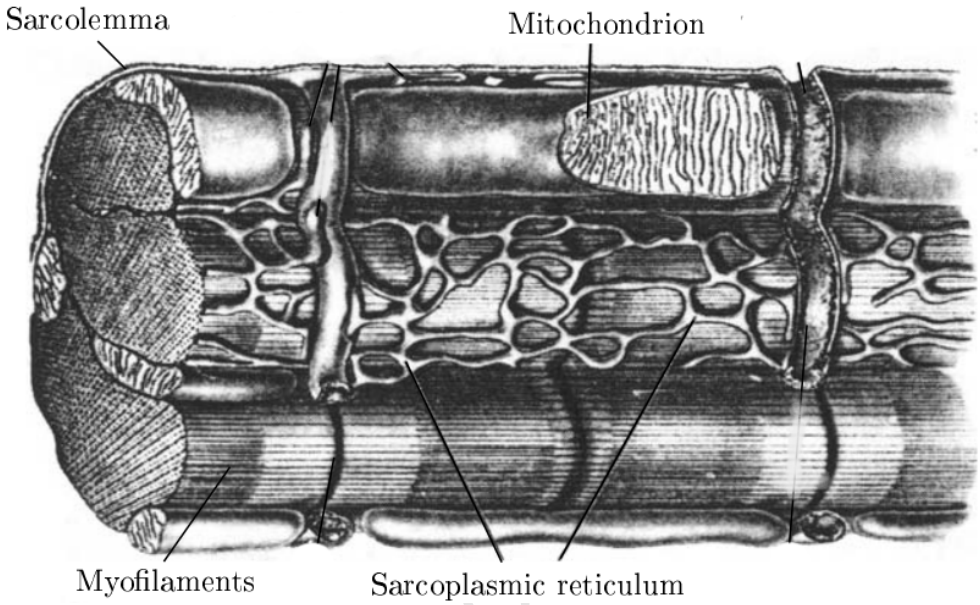

Figure 4.2: Schematic of a myocyte [104].

Cytoplasm is the fluid that fills the spaces within the cell. It is made up of water, electrolytes (ion solutions), lipids, salts, and proteins. Cytoplasm contributes a relatively small proportion of the volume of the myocyte with much of the volume of the myocyte being taken by the myofibrils. Mitochondria, the energy producers of cells, are present in myocytes and occupy $14 - 36\%$ of the volume of the myocyte.

Myofibrils are the tube shaped contractile elements of the cell. Approximately half of the volume of myocytes is taken up by myofibrils. They are approximately $1\mu m$ thick and are divided every $2.5\mu m$ into the sarcomeres. Each sarcomere contains myofilaments which cause the mechanical contraction of the cell. There are two types of myofilament, actin (thin) and myosin (thick) filaments (see Fig. 4.3). The sarcomeres are enclosed by the sarcoplasmic reticulum which is further enclosed by a membrane containing various ion channels. The sarcoplasmic reticulum stores reserves of calcium ions and plays an important role in regulating the intracellular calcium concentration during contraction.

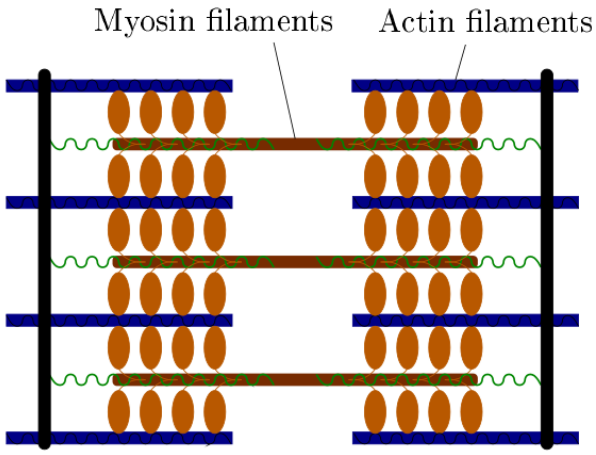

Figure 4.3: Schematic of myofilament microstructure. Adapted from [104].

4.1.2 Extracellular Matrix

The myocardium is supported by a mesh of connective tissue called the extracellular matrix (ECM). The main constituent of the ECM is collagen, a protein. Collagen fibrils take up 2-5% of the heart volume and contribute to the mechanical stiffness of the myocardium. Extracellular fluid fills the spaces between myocytes and contains water, ions and other substances. Collagen fibres are generally not oriented in any preferred direction.

4.1.3 Myocardial Infarction

Myocardial infarction occurs when blood flow to part of the myocardium is obstructed or restricted. This lack of blood supply causes a gradual decline in mechanical function of the associated myocardium. The time course of structural changes that occur can be divided into four phases: acute ischaemia, necrotic phase, fibrotic phase and remodelling phase [105, 106].

The first phase, acute ischaemia, occurs in the first few hours after myocardial infarction before the infarct begins to stiffen. The myocardium becomes more compliant due to degradation of the ECM [107]. During this phase the myocardium has lost its blood supply and after a few minutes contractile function ceases and the myocardium acts passively. Adjacent myocardium, called the border zone, is impaired by the non-contractile ischaemic myocardium.

During the second phase, the necrotic phase, the infarcted myocardium un-

dergoes necrosis (cell death). As well as myocytes dying it has been observed that the ECM decays and is replaced by a new matrix in the subsequent fibrotic phase. It is at this stage that the infarct is most likely to rupture if stresses become too high.

During the third phase, the fibrotic phase, collagen accumulates in the infarcted region and a scar forms [106]. The scar is stiffer than the healthy myocardium. The scar tissue is isotropic, i.e. it does not have a preferred direction [106].

During the last phase, the remodelling phase, the scar thins to take up a smaller percentage of the wall volume. Elevated wall stresses are an important factor in the remodelling process [108, 109].

4.2 Cardiac Function

During the cardiac cycle the volume of blood within each cavity and the pressure on the cavity walls varies with the opening and closing of valves and the contraction of the heart. The cardiac cycle is divided into systole when the left ventricle contracts and diastole when the left ventricle does not contract. The cardiac cycle is periodic so that blood can be continually pumped throughout the body.

Diastole and systole can be further divided into two phases. The four main phases for the left ventricle can be identified as follows:

- Diastole: Diastolic filling: The mitral valve opens allowing blood from the left atrium to fill the ventricle. The influx of blood causes the cavity volume and pressure to increase. The cavity inflates as there is no contractile force to oppose the force of the blood being pumped in.

- Systole: Isovolumetric contraction: The ventricle contracts with the mitral valve and aortic valve closed. The cavity volume remains constant or nearly constant since all valves are closed and the pressure in the cavity increases due to the contraction of the ventricle.

- Systole: Ejection: Once the pressure within the cavity reaches the same pressure as in the aorta the aortic valve opens and blood is ejected from the ventricle. The cavity volume decreases as blood is expelled from the

contracting left ventricle. The pressure in the cavity first increases further due to the compliance of the aorta and then decreases as the rate of ejection decreases.

- Diastole: Isovolumetric relaxation: Once the cavity ceases to contract further the aortic valve closes and the ventricle relaxes. The cavity volume remains constant or nearly constant as all the valves are closed. The pressure decreases due to the relaxation of the ventricle.

The end-systolic volume is defined as the cavity volume at end-systole. The end-diastolic volume is defined as the cavity volume at end-diastole. The stroke volume is defined as the amount of blood expelled during systole (i.e. the difference between end-diastolic volume and end-systolic volume. The ejection fraction is defined as the stroke volume divided by the end-diastolic volume.

4.3 Passive Mechanics

The constituents of the myocardium are so small that it can be modelled as a three dimensional continuum. Modelling the myocardium as a continuum means the theory in continuum mechanics can be used to describe the mechanical deformation of the heart under forces such as blood filling pressure and active contractile forces in the myocardium. In this work the myocardium is described as an inhomogeneous, orthotropic, nearly incompressible viscoelastic material [88].

The myocardium is subjected to external loads (via the pressure from blood filling the ventricles). These loads can be described in the form of pressure boundary conditions applied to the endocardium of the heart. It is important that these changing boundary conditions are physiologically accurate so that simulations correspond well with experiment.

4.3.1 Residual Stresses

Residual stresses are stresses that remain in a body even when there are no external loads. Experimentally, compressive residual circumferential stresses have been found near the endocardium, while there tensile residual circumferential stresses were found near the epicardium [110]. It has been postulated that residual stresses develop during growth of the heart [111, 112].

Residual stresses can be elucidated and quantified by making a cut in the myocardium transverse to the fibres (as shown in [113]). Once this is done the myocardium will "open up" due to the residual stresses (see Fig. 4.4). This new configuration has lower residual stresses than the original configuration.

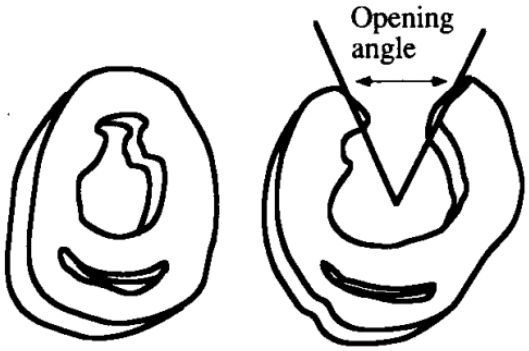

Figure 4.4: Diagram showing the effect of residual stresses in the heart ventricle [114].

An important effect that residual stresses have on the myocardium is that the sarcomere length in the unloaded configuration (with residual stresses) shows a transmural variation with smaller values at the endocardium and higher values at the epicardium [114]. In the stress-free state the sarcomere length does not vary transmurally. This is important for active contraction as the active force generated is highly dependent on the sarcomere length (see Section 4.4).

In this work the effect of residual stresses is incorporated in the active stress model. The sarcomere rest length is defined to vary linearly transmurally through the heart wall from $1.78\mu m$ at the endocardium to $1.91\mu m$ at the endocardium [114].

4.3.2 Constitutive Law

Whilst early models described the nonlinear nature of the myocardium as isotropic, a description taking into account the fibre structure of cardiac tissue is necessary. A number of mechanical effects are due to the fibre structure of myocytes in the myocardium. Torsion of the heart which aids in pumping the blood out of the heart is a result of the fibre structure.

In this work the passive mechanical model of Usyk *et al.* [5] is used. This

model describes the myocardium as orthotropic and nearly incompressibility. In the Usyk model the strain energy function is given by

$$\psi_P = \frac{A}{2}\left(e^Q - 1\right) + A_{comp}\left(J \ln J - J + 1\right) \tag{4.1}$$

where A is a stiffness factor A_{comp} is a constant controlling compressibility of the myocardium and

$$Q = b_{11}E_{11}^2 + b_{22}E_{22}^2 + b_{33}E_{33}^2 + b_{12}(E_{12}^2 + E_{21}^2) + b_{13}(E_{13}^2 + E_{31}^2) + b_{23}(E_{23}^2 + E_{32}^2) \tag{4.2}$$

where b_{ij}, $i, j = 1, 2, 3$ are material parameters and E_{ij} are the components of the Green strain tensor in the local coordinate system defined by the three material directions $\mathbf{V}_i$ is the i^{th} direction

$$E_{ij} = \mathrm{tr}\left(\mathbf{E}\left(\mathbf{V}_i \otimes \mathbf{V}_j\right)\right). \tag{4.3}$$

Since the constitutive law is orthotropic it can be expressed in terms of the nine invariants of $\mathbf{E}$. Note that the eq. 4.2 contains the squares of the components of the Green strain tensor in the local coordinate system. This is similar to the invariants as expressed in terms of the components of the Green strain tensor in the local coordinate system. This motivates introducing a form of Q based on these invariants, this is

$$Q = a_1 I_4^2 + a_2 I_6^2 + a_3 I_8^2 + a_4 I_5 + a_5 I_7 + a_6 I_9. \tag{4.4}$$

Eq. ((4.4)) can be expressed in terms of the components of $\mathbf{E}$ in the local coordinate system:

$$\begin{aligned} Q &= a_1 E_{11}^2 + a_2 E_{22}^2 + a_3 E_{33}^2 + a_4\left(E_{11}^2 + E_{12}^2 + E_{13}^2\right) \\ &\quad + a_5\left(E_{21}^2 + E_{22}^2 + E_{23}^2\right) + a_6\left(E_{31}^2 + E_{32}^2 + E_{33}^2\right) \\ &= \left(a_1 + a_4\right)E_{11}^2 + \left(a_2 + a_5\right)E_{22}^2 + \left(a_3 + a_6\right)E_{33}^2 \\ &\quad + \frac{1}{2}\left(a_4 + a_5\right)\left(E_{12}^2 + E_{21}^2\right) + \frac{1}{2}\left(a_4 + a_6\right)\left(E_{13}^2 + E_{31}^2\right) \\ &\quad + \frac{1}{2}\left(a_5 + a_6\right)\left(E_{23}^2 + E_{32}^2\right). \end{aligned} \tag{4.5}$$

Equating like terms of eq. (4.2) and (4.5), the newly defined parameters a_i in

terms of the parameters b_{ij} are:

$$a_1 = b_{11} - b_{12} - b_{13} + b_{23} \quad (4.6)$$
$$a_2 = b_{22} - b_{12} + b_{13} - b_{23} \quad (4.7)$$
$$a_3 = b_{33} + b_{12} - b_{13} - b_{23} \quad (4.8)$$
$$a_4 = b_{12} + b_{13} - b_{23} \quad (4.9)$$
$$a_5 = b_{12} - b_{13} + b_{23} \quad (4.10)$$
$$a_6 = -b_{12} + b_{13} + b_{23}.reticulum \quad (4.11)$$

Using eq. (2.52) the second Piola-Kirchhoff tensor of this strain energy function was found to be

$$\begin{aligned} \mathbf{S} &= \frac{1}{2}Ae^{Q}\frac{\partial Q}{\partial \mathbf{E}} + A_{comp}\left(\frac{\partial J}{\partial \mathbf{E}}\ln J + \frac{1}{J}\frac{\partial J}{\partial \mathbf{E}} - \frac{\partial J}{\partial \mathbf{E}}\right) \\ &= \frac{1}{2}Ae^{Q}\frac{\partial Q}{\partial \mathbf{E}} + A_{comp}\left(J\ln J - J + 1\right)(\mathbf{C})^{-1}, \end{aligned} \quad (4.12)$$

where

$$\begin{aligned} \frac{\partial Q}{\partial \mathbf{E}} &= 2a_1 I_4 \mathbf{M}_1 + 2a_2 I_6 \mathbf{M}_2 + 2a_3 I_8 \mathbf{M}_3 \\ &\quad + a_4\left(\mathbf{M}_1\mathbf{E} + \mathbf{E}\mathbf{M}_1\right) + a_5\left(\mathbf{M}_2\mathbf{E} + \mathbf{E}\mathbf{M}_2\right) + a_6\left(\mathbf{M}_3\mathbf{E} + \mathbf{E}\mathbf{M}_3\right) \end{aligned} \quad (4.13)$$

For a certain set of material parameters this orthotropic constitutive law reduces to a transversely isotropic constitutive law [5]. In this study material parameters describing transverse isotropy are used. These material parameters are shown in Table 4.1.

A	A_{comp}	a_1	a_2	a_3	a_4	a_5	a_6
$0.88kPa$	$3.0kPa$	0	-1	-1	6	6	6

Table 4.1: Parameter values for the Usyk constitutive law.

While the myocardium is incompressible, it has been found that applying near incompressibility results in more accurate numerical results [5, 115]. The last term in the Usyk constitutive law (eq. (4.1)) controls the compressibility of the myocardium.

The orthotropic model of Usyk is used as other members of the author's

research group are also studying rats so experimental data may become available in the future. This model has also been implemented in a number of simulation studies which makes validating the performance and implementation easier [116–118].

4.3.3 Infarct Mechanics

The structural changes that occur after a myocardial infarction has occurred have been discussed in Section 4.1.3. In this work the ischaemic phase of myocardial infarction has been modelled. During this phase the myocardium is generally described by the same constitutive law as the healthy myocardium except with a reduced overall stiffness (the stress tensor is multiplied by a reduction factor) [119]. This seeks to represent that the myocardium is still intact, but weaker due to the degrading of the ECM. During acute ischaemia there is no active stress in the infarcted region as the myocardium loses its ability to generate force within minutes.

4.4 Active Mechanics

A key aspect of modelling the mechanics of the heart is describing the active contraction of cardiac tissue. Contraction occurs on a cell level when the sarcomere, the contractile unit of the myocyte, develops tension and contracts due to changes in intracellular calcium concentration level. The contraction of each individual myocyte causes the overall contraction of the myocardium. To model this contraction the active stress model of Guccione *et al.* [68] where a tensile stress is added to the passive stress used.

The active stress model requires a constitutive law that describes the dynamics of tension development due to changes in the cell be they mechanical such as stretch or chemical such as intracellular calcium concentration. This constitutive law defines the active tension as a function of the stretch and time. The resulting active tension is transformed into an active stress acting in the fibre direction.

4.4.1 Tension Development

Tension development is initiated when an electrical impulse passes over the sarcomere causing calcium ion channels to open and increasing intracellular calcium concentration. The increase in intracellular calcium concentration causes a cyclical binding of myosin heads with actin and the subsequent sliding and overlapping of the myofilaments. The binding of myosin heads to the actin filament is said to create crossbridges between myosin and actin. Adenosine triphosphate supplies the energy for contraction of the myocyte. The overlapping of these myofilaments causes the contraction of the myocyte.

4.4.2 Active Stress

In the active stress formulation the total stress is defined as the sum of an active stress and a passive stress representing the passive mechanical response of tissue to loads (as described in Section 4.3). The active stress acts in the direction of the fibres. The total deformation is then found by solving the mechanics equations with this modified constitutive law.

In the active stress formulation the total stress is defined as the sum of a passive stress $\mathbf{S}_P$ and an active stress $\mathbf{S}_A$ so that

$$\mathbf{S} = \mathbf{S}_P + \mathbf{S}_A, \tag{4.14}$$

where $\mathbf{S}$ is the second Piola Kirchhoff tensor. The passive stress is taken from from the passive mechanical law so that when there is no active stress ($\mathbf{S}_A = 0$) the myocardium simply behaves passively. The active stress is assumed to act only in the fibre direction $\mathbf{V}_1$ so that

$$\mathbf{S}_A = T_A \mathbf{M}_1. \tag{4.15}$$

The variable T_A represents the active tension developed in the myocyte and is derived from a cellular model of tension development in myocytes as described in the subsequent section.

4.4.3 Tension Development Model

For the purposes of studying the tissue level mechanics of the heart it is appropriate to use a simple tension development model, here, the model of Guccione *et al.* [6]. This model was derived from biophysical considerations of calcium dynamics and crossbridge formation. The model was developed as an approximation to a more complex model based on experimental data.

The Guccione model predicts the tension developed as

$$T_A = T_{max} \frac{Ca_0^2}{Ca_0^2 + ECa_{50}^2(l)} C_t(l,t) \tag{4.16}$$

where C_t represents the time transient dependent on time and sarcomere length, ECa_{50}^2 represents the calcium concentration at which tension is 50%, Ca_0 is the peak intracellular calcium concentration, l is the sarcomere length and T_{max} is the maximum tension developed.

The functions C_t and ECa_{50} are given by

$$C_t = \frac{1}{2}(1 - \cos\omega(l,t)) \tag{4.17}$$

$$ECa_{50}(l) = \begin{cases} \frac{(Ca_0)_{max}}{\sqrt{\exp[B(l-l_0)]-1}} & \text{for } l > l_0 \\ 0 & \text{for } l \leq l_0 \end{cases} \tag{4.18}$$

where B is a constant and l_0 is the sarcomere length below which there is no active tension developed. The sarcomere length is a function of the stretch (see eq. 2.8) with respect to the reference configuration in the fibre direction $\alpha = \sqrt{2\text{tr}(\mathbf{M}_1\mathbf{E}) + 1} = \sqrt{2I_4 + 1}$ so that

$$l = l_R\sqrt{2I_4 + 1} \tag{4.19}$$

where l_R is the sarcomere rest length in the undeformed reference configuration. As mentioned in Section 4.3.1 the measured sarcomere rest length in the undeformed configuration is influenced by the residual stresses. The sarcomere rest length thus varies from $1.78\mu m$ at the endocardium to $1.91\mu m$ at the epicardium [114]. The time dependence of the active tension is described by the

function $\omega(t)$ which is given by

$$\omega(l,t) = \begin{cases} \pi \frac{t-u}{t_0} & \text{for } 0 \leq t < t_0 \\ \pi \left[\frac{t-u-t_0}{t_r(l)} + 1 \right] & \text{for } t_0 \leq t < t_0 + t_r \\ 0 & \text{for } t \geq t_0 + t_r \end{cases} \tag{4.20}$$

where t_0 is the time to peak tension, u is the depolarisation time (equivalently the starting time of contraction) and t_r is the duration of the relaxation period described as a function of the sarcomere length

$$t_r = ml + b \tag{4.21}$$

with constants m and b. The parameters used by Guccione *et al.* were calibrated for the canine heart. In order to describe the active tension development in the rat left ventricle the maximum active tension parameter has been scaled to rat tension development data [120]. The parameter T_{max} was reduced from $135.7kPa$ to $56.2kPa$. The full set of parameters used for the active tension model are given in Table 4.2.

T_{max} (kPa)	56.7
Ca_0 (μM)	4.35
$(Ca_0)_{max}$ (μM)	4.35
B (μm^{-1})	4.75
l_0 (μm)	1.58
t_0 (ms)	250
m $(s\mu m^{-1})$	1.0489
b (ms)	-1429

Table 4.2: Parameter values for the Guccione active stress model.

The maximum developed tension occurs when $t = t_0 + u$. At this point the tension is

$$T_A(t_0 + u) = T_{max} \frac{\mathrm{Ca}_0^2}{\mathrm{Ca}_0^2 + (Ca_0)_{max}^2 \, e^{-[B(l-l_0)-1]}}. \tag{4.22}$$

This length dependence of the maximum developed tension can be seen in Fig. 4.5. This models the known length dependence of the calcium sensitivity of proteins that cause tension development.

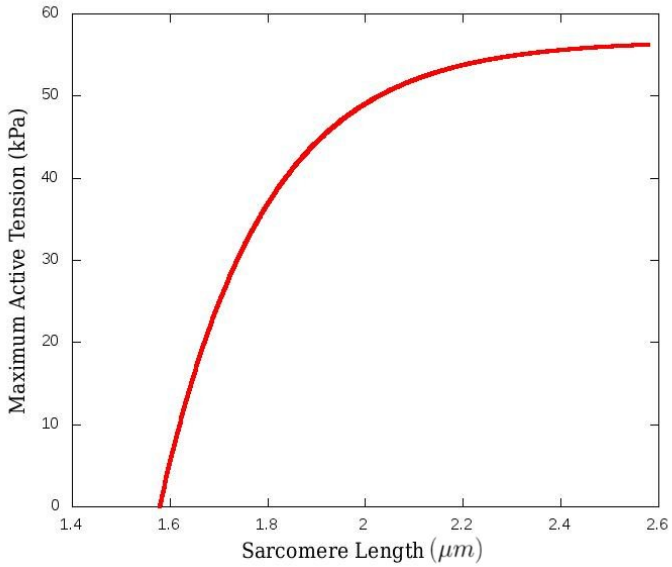

Figure 4.5: Maximum active tension as a function of sarcomere length.

While the exact underlying basis of the length dependence of the active tension is still unknown, its effects are well known in cardiology as the Frank-Starling law. The Frank-Starling law, first discovered in the early twentieth century, states that an increase in end-diastolic volume results in an increase in stroke volume [121]. This means that the more blood entering the ventricle during diastole, the more blood is ejected from the heart. This effect is particularly evident in athletes, who have been found to have an increased left ventricular compliance [122]. This increased compliance results in a larger end diastolic volume and larger sarcomere lengths due to the increased stretch. The larger sarcomere length produces a larger active tension and ultimately there is increased ejection of blood from the ventricle.

The time dependence of the active tension described by the function C_t scales the active tension by a sinusoidal curve rising from zero to one and then back down to one. The upstroke to a maximum has a period t_0 while the down-stroke back to zero has a period t_r for a total period of active tension of $T = t_0 + t_r$. This time dependence can be seen in the active tension graphs of Fig. 4.6. The period of active tension for the three constant sarcomere lengths $1.7\mu m$, $2.0\mu m$ and $2.3\mu m$ can be calculated as $604.1ms$, $918.8ms$ and $1233.3ms$ respectively.

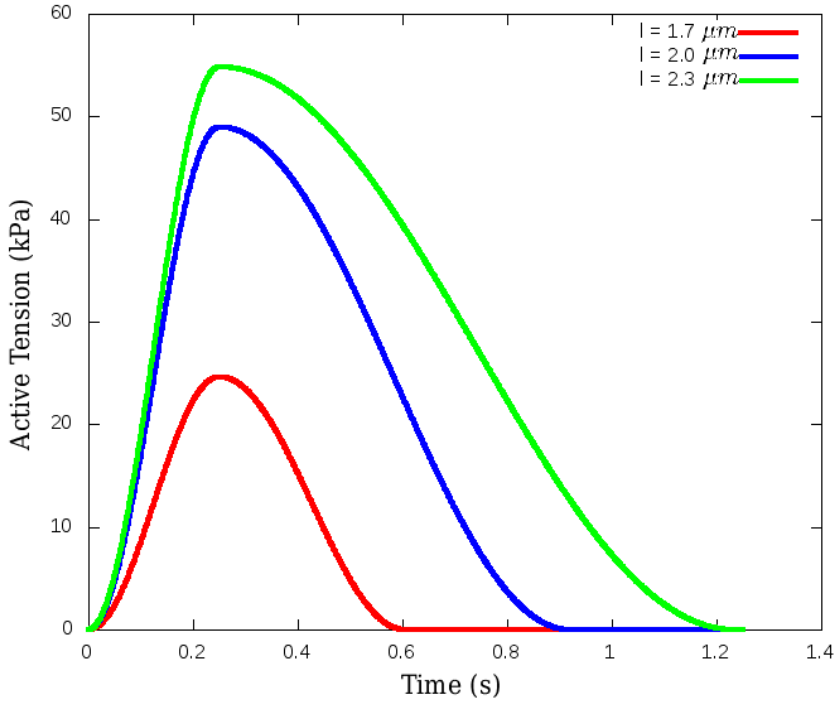

Figure 4.6: Active tension as a function of time for three representative sarcomere lengths $1.7\mu m$, $2.0\mu m$ and $2.3\mu m$. The depolarisation time is taken as $u = 0\,s$.

4.5 Geometry

Idealised geometries are particularly useful when it comes to developing models for cardiac function. A common idealised geometry of the left ventricle is that of a truncated ellipsoid [59, 61, 123, 124]. In this formulation the left ventricle is assumed to take the shape of an ellipsoid that has been cut off at the top (see Fig. 4.7).

It is convenient to use a prolate spheroidal coordinate system to describe the ellipsoidal geometry. The prolate spheroidal coordinate system is an orthogonal curvilinear coordinate system [125]. The relationship between Cartesian and prolate spheroidal coordinates is given by

$$x_1 = C \sinh\xi \sin\eta \cos\phi \tag{4.23}$$

$$x_2 = C \sinh\xi \sin\eta \sin\phi \tag{4.24}$$

$$x_3 = C \cosh\xi \cos\eta \tag{4.25}$$

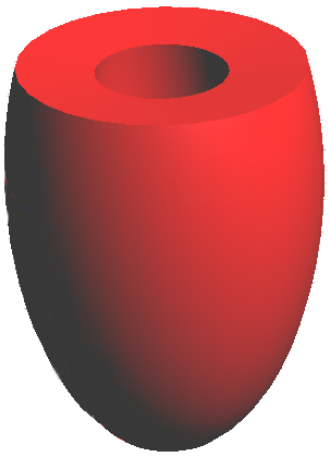

Figure 4.7: Truncated ellipsoid geometry.

where $\xi \in [0, \infty)$, $\eta \in [0, \pi]$ and $\phi \in [0, 2\pi)$ are the prolate spheroidal coordinates, C is the prolate constant, x_i are the usual Cartesian coordinates.

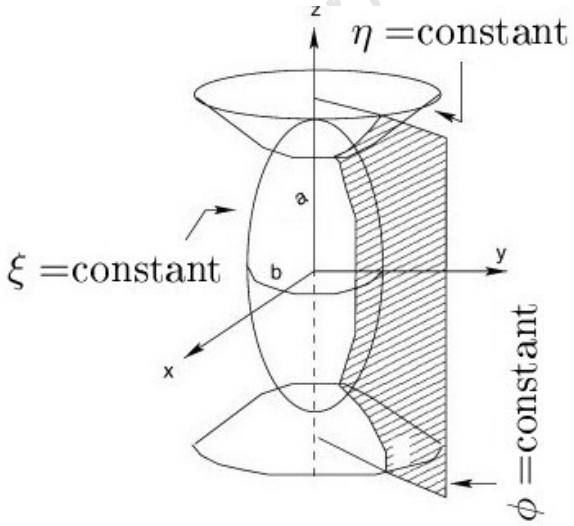

Figure 4.8: Three dimensional prolate spheroidal coordinates diagram.

It is useful to use prolate spheroidal coordinates, because surfaces of constant ξ represent axisymmetric ellipsoids with major axis length $a = C\cosh\xi$ and minor axis length $b = C\sinh\xi$. The truncated ellipsoid geometry can then be completely defined by defining a prolate constant C, the epicardial surface coordinate ξ_{epi}, the endocardial surface coordinate ξ_{endo} and a truncation height h from the equator.

To model a rat left ventricle experimental data of the dimensions of the unloaded rat heart have been used [13, 14]. The inner radius and outer radius are given as $2.4mm$ and $5.1mm$ respectively. The inner apex to base and outer apex to base measurements are given as $11.5mm$ and $13.2mm$. From this data the parameters $C = 7.18mm$, $\xi_{epi} = 0.66$, $\xi_{endo} = 0.32$ and $h = 4.39mm$ were calculated. The resulting geometry has a cavity volume of $156\mu L$.

4.5.1 Auxiliary Coordinate System

It is convenient to make use of the prolate spheroidal coordinate system to define an auxiliary coordinate system that describes the both the transmural and longitudinal position in the myocardium (see Fig. 4.9). This can be done to make the transmural coordinate $\bar{\xi}$ (or v) vary monotonically from $\bar{\xi}_{endo} = -1$ at the endocardium to $\bar{\xi}_{epi} = 1$ at the epicardium and the longitudinal coordinate $\bar{\eta}$ (or u) to vary monotonically from $\bar{\eta}_{apex} = -1$ at the apex to $\bar{\eta}_{mid} = 0$ at the equator.

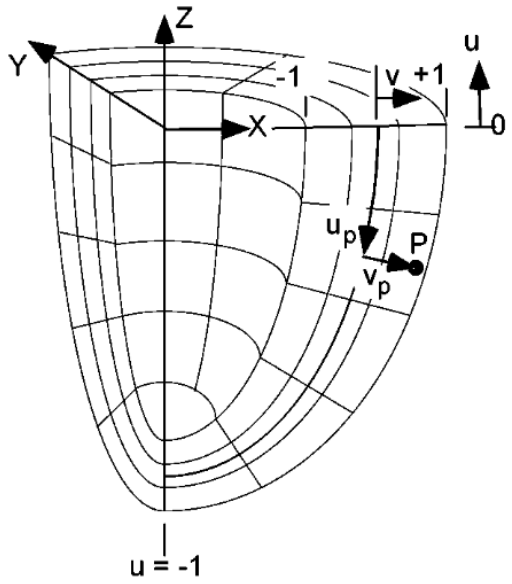

Figure 4.9: Transmural and longitudinal coordinate system [124].

Using the following relations the "transmural" prolate spheroidal coordinate ξ and "longitudinal" prolate spheroidal coordinate η are shifted so that they are centred on zero. Then the coordinates are scaled so that they vary from -1 to +1

in the correct direction

$$v = \bar{\xi} = (\xi - \xi_{mid}) \frac{\bar{\xi}_{diff}}{\xi_{diff}}, \tag{4.26}$$

where

$$\xi_{diff} = \xi_{epi} - \xi_{endo} \tag{4.27}$$
$$\bar{\xi}_{diff} = \bar{\xi}_{epi} - \bar{\xi}_{endo} = 2 \tag{4.28}$$
$$\xi_{mid} = \frac{\xi_{epi} + \xi_{endo}}{2}, \tag{4.29}$$

and

$$u = \bar{\eta} = (\eta - \eta_{mid}) \frac{\bar{\eta}_{diff}}{\eta_{diff}} = -(\eta - \pi/2)\, 2/\pi, \tag{4.30}$$

where

$$\eta_{diff} = \eta_{apex} - \eta_{base} = \pi \tag{4.31}$$
$$\bar{\eta}_{diff} = \bar{\eta}_{apex} - \bar{\eta}_{base} = -2 \tag{4.32}$$
$$\eta_{mid} = \pi/2, \tag{4.33}$$

which requires the input of ξ_{epi} and ξ_{endo} for the animal model being studied. Note that these new coordinates do not vary linearly with transmural and longitudinal distance, but do vary monotonically transmurally and longitudinally.

4.5.2 Fibre Directions

An analytical expression for the fibre directions found by Rijcken *et al.* in an optimisation study is used to describe the fibre structure of the heart [124]. The fibre directions found using this expression compared well with experimental data [126, 127].

The fibre direction is a function of the helical angle, α_h, and transverse angle, α_t, (see Fig. 4.10). The helical and transverse angles of the fibre direction vary based on the transmural and longitudinal position within the myocardium in the following way

$$\alpha_h(v) = p_1 + p_2 v, \tag{4.34}$$
$$\alpha_t(u, v) = p_3 u \left(1 - v^2\right) \tag{4.35}$$

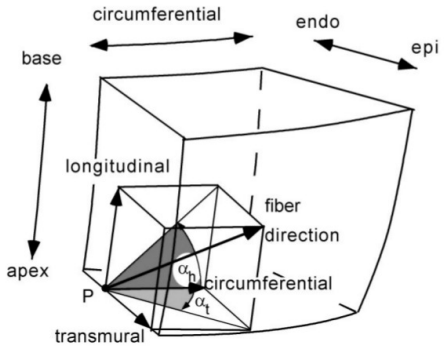

Figure 4.10: Diagram showing angles used to define fibre directions [124].

where p_1, p_2 and p_3 are constants, and u and v are the respective normalised longitudinal and transmural coordinates introduced in the previous Section. The values for the parameters p_1, p_2 and p_3 are given in Table 4.3.

p_1 (rad)	p_2 (rad)	p_3 (rad)
0.3533429174	-1.147553983	0.291993584

Table 4.3: Parameter values for the fibre direction model [124].

From these angles, together with the basis vectors of the prolate spheroidal coordinate system, the fibre direction can be constructed. The relevant basis vectors are the "circumferential" basis vector, $\boldsymbol{\phi}$,the "transmural" basis vector, $\boldsymbol{\xi}$, and the "longitudinal" basis vector, $\boldsymbol{\eta}$ which are given by

$$\begin{aligned}\boldsymbol{\xi} &= \frac{1}{\sqrt{\cosh^2\xi\sin^2\eta+\sinh^2\xi\cos^2\eta}} \\ &\quad\times(\cosh\xi\sin\eta\cos\phi\mathbf{e}_1+\cosh\xi\sin\eta\sin\phi\mathbf{e}_2+\sinh\xi\cos\nu\mathbf{e}_3) \quad (4.36)\\ \boldsymbol{\phi} &= \frac{1}{\sqrt{\sinh\xi\sin\eta}} \\ &\quad\times(-\sinh\xi\sin\eta\sin\phi\mathbf{e}_1+\sinh\xi\sin\eta\cos\phi\mathbf{e}_2+0\mathbf{e}_3) \quad (4.37)\\ \boldsymbol{\eta} &= -\frac{1}{\sqrt{\cosh^2\xi\sin^2\eta+\sinh^2\xi\cos^2\eta}} \\ &\quad\times(\sinh\xi\cos\eta\cos\phi\mathbf{e}_1+\sinh\xi\cos\eta\sin\phi\mathbf{e}_2+\cosh\xi\sin\nu\mathbf{e}_3) \quad (4.38)\end{aligned}$$

This fibre direction $\mathbf{V}_1$ can then be calculated as

$$\mathbf{V}_1 = \tan\alpha_t\,\boldsymbol{\xi}+\tan\alpha_h\,\boldsymbol{\phi}+\boldsymbol{\eta}. \quad (4.39)$$

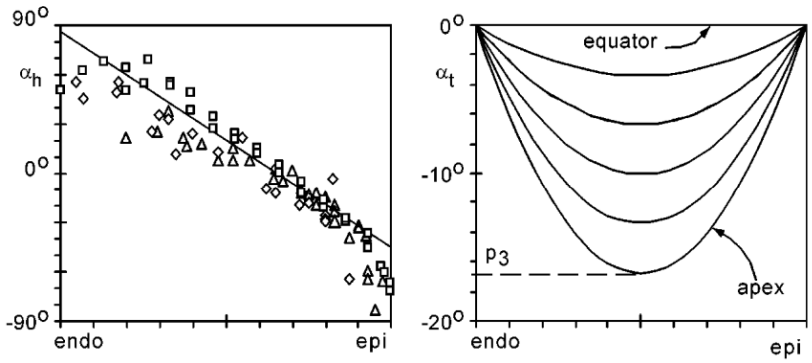

Figure 4.11: Fibre direction angles as a function of transmural position [124].

The helical fibre direction angles α_h is shown in Fig. 4.11. They correspond well with experimental fibre directions found in the literature [126, 127]. Notice the helical angle varying from almost 90° at the endocardium to −60° at the epicardium. On the endocardium and epicardium the fibre direction is tangent to the surface since the $(1 - v^2)$ factor of eq. (4.35) is zero when on the endocardium, $v = -1$, and the epicardium, $v = +1$.

4.6 Boundary Conditions

To simulate the mechanics of the cardiac cycle it is necessary to apply appropriate boundary conditions. Two types of boundary conditions need to be applied. Deformation boundary conditions are required to prevent rigid body motion and to constrain the base of the heart. Pressure boundary conditions are required to simulate the blood filling pressure acting on the endocardium of the left ventricle.

4.6.1 Deformation Boundary Conditions

At the base of the ellipsoid there is an opening which corresponds to the aortic valve through which blood leaves the heart. This valve is relatively stiff so a ring at the base of the ellipsoid has been constrained to undergo no displacement

$$\mathbf{u} = \mathbf{0} \qquad \text{on } \Gamma_D. \tag{4.40}$$

where Γ_D is the upper ring of the ellipsoid [128].

4.6.2 Pressure Boundary Conditions

The blood inside the heart exerts pressure on the endocardium of the left ventricle. This suggests that a pressure boundary condition is applied to the inner wall of the ellipsoid. During the heart cycle's four phases different pressure boundary conditions exist due to changes in blood flow in and out of the left ventricle.

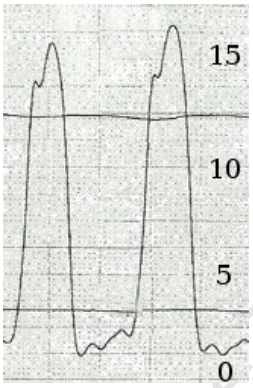

Figure 4.12: Wigger's plot showing the pressure transient of a human left ventricle during two cardiac cycles. x-axis is time, y-axis is pressure in $mmHg$. Adapted from Seiler *et al.* [129].

During diastole the mitral valve is open and blood flows into the left ventricle. The pressure exerted by the blood in the left ventricle increases over time. The transient of the pressure is evaluated by a Wigger's plot, which descibes the experimentally found pressure transient of the cardiac cycle. [130] (see Fig. 4.12). The pressure boundary condition is simply applied to the endocardium.

During isovolumetric contraction all valves are closed. This means that the volume of the cavity of the left ventricle should not change. While the heart contracts the blood exerts pressure on the heart wall to prevent volume change (since blood is mostly water, it is incompressible). This pressure needs to be calculated by an iterative procedure.

During ejection the aortic valve is open and blood flows out of the heart due to the contracting ventricle. The pressure that is now exerted by the blood on the heart wall varies in time depending on the resistance offered by the compliant aorta. An approximation is to assume the pressure reached at end-isovolumetric contraction. This is valid physiologically as for the rat left ventricle the pressure during this phase is approximately constant [18].

During isovolumetric relaxation the valves close once again and the contraction of the heart steadily reduces over time. This reduction leads to a reduced pressure exerted by the blood, which is again calculated iteratively since the effect of the active stress is not known *a priori*.

It is important to note that the pressure acts in the current configuration. The traction is thus

$$\mathbf{t}^{(\mathbf{n})} = p\mathbf{n} \qquad \text{on } \partial\mathcal{B}_{tN} \tag{4.41}$$

where the Neumann boundary in the current configuration is denoted as $\partial\mathcal{B}_{tN}$. The corresponding term in the variation formulation (eq. (2.25)) is the external work $\mathcal{W}_{ext}$ since the body force is negligible

$$\mathcal{W}_{ext} = \int_{\partial\mathcal{B}_{tN}} p\mathbf{n} \cdot \delta\mathbf{u} da \tag{4.42}$$

noting integration over the Neumann boundary in the current configuration. To convert this integral to an integral over the reference configuration Nanson's formula relating surface elements in the current and reference configuration (see eq. (2.4)). This results in

$$\mathcal{W}_{ext} = \int_{\partial\mathcal{B}_N} pJ\mathbf{F}^{-T}\mathbf{N} \cdot (\mathbf{V} \otimes \mathbf{V})\, \delta\mathbf{u} dA \tag{4.43}$$

noting integration of the Neumann boundary in the reference configuration.

Chapter 5

Numerical Formulation

5.1 Numerical Method

The element-free Galerkin method (EFGM) with moving least squares (MLS) shape functions was used to interpolate solutions over the domain. EFGM is a meshless method meaning that instead of using a mesh as in the finite element method (FEM) a particle distribution is used to calculate the shape functions.

5.1.1 Moving Least Squares Shape Functions

In the Moving Least Square Method (MLS) an approximation for a solution is constructed based on a given particle distribution. In the following the MLS method is briefly outlined [7, 131, 132]. Consider a scalar function $u(\mathbf{x})$ defined over the field Ω. An approximation for $u(\mathbf{x})$ is defined by a complete polynomial $\mathbf{P}(\mathbf{x})$ and its non-constant coefficients $\mathbf{a}(\mathbf{x})$:

$$u^h(\mathbf{x}) = \mathbf{P}(\mathbf{x}) \cdot \mathbf{a}(\mathbf{x}). \tag{5.1}$$

A *weight function* Φ with compact support is associated with each particle (see Figure 5.1). ϱ defines the so-called *influence radius* of Φ. The sum of all particles with coordinates $\mathbf{x}_I$, that fall within the support of the point $\mathbf{x}$, constitute the set Λ. Using this set a weighted least square fit close to a point $\mathbf{x}$ can be constructed

as

$$J\left(\mathbf{a}\left(\mathbf{x}\right)\right) \;:=\; \sum_{I\in\Lambda}\left[\mathbf{P}\left(\mathbf{x}_I\right)\cdot\mathbf{a}\left(\mathbf{x}\right)-u\left(\mathbf{x}_I\right)\right]^2\Phi\left(\frac{\mathbf{x}-\mathbf{x}_I}{\varrho}\right). \tag{5.2}$$

The least square fit is weighted by the function Φ which, in this case, is taken to be a C^3 quartic spline. Note that a function f is said to be of class C^k if the k^{th} derivative of f exists and is continuous.

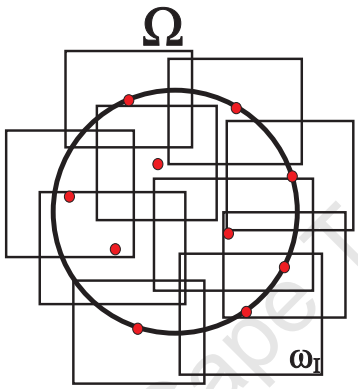

Figure 5.1: Domain in EFGM method showing particles (red) and their associated influence domains with weight functions ω_I covering the circular domain Ω.

The unknown coefficients $\mathbf{a}(\mathbf{x})$ can be determined by minimising the functional J (eq. (5.2)) with respect to $\mathbf{a}(\mathbf{x})$. Then the substitution of the coefficients $\mathbf{a}(\mathbf{x})$ in eq. (5.1) provides the approximation of $u(\mathbf{x})$ as follows

$$u^h\left(\mathbf{x}\right)=\mathbf{P}\left(\mathbf{x}\right)\cdot\mathbf{M}^{-1}\left(\mathbf{x}\right)\sum_{I\in\Lambda}\mathbf{P}\left(\mathbf{x}_I\right)\,\Phi\left(\frac{\mathbf{x}-\mathbf{x}_I}{\varrho}\right)\,u_I\,, \tag{5.3}$$

where $\mathbf{M}(\mathbf{x})$ is the *moment matrix* of the weight function Φ:

$$\mathbf{M}\left(\mathbf{x}\right) \;=\; \sum_{I\in\Lambda}\mathbf{P}\left(\mathbf{x}_I\right)\mathbf{P}\left(\mathbf{x}_I\right)\Phi\left(\frac{\mathbf{x}-\mathbf{x}_I}{\varrho}\right). \tag{5.4}$$

and u_I are the particle parameters.

Comparing this to FEM the particle parameters correspond to the nodal degrees of freedom of FEM. If the local approximation is defined as a sum over

particles with associated shape functions as

$$u^h(\mathbf{x}) = \sum_{I \in \Lambda} \phi_I(\mathbf{x})\, u_I \tag{5.5}$$

where the shape functions are given as

$$\phi_I(\mathbf{x}) = \mathbf{P}(\mathbf{x}) \cdot \mathbf{M}^{-1}(\mathbf{x}) \cdot \mathbf{P}(\mathbf{x}_I)\ \Phi\left(\frac{\mathbf{x} - \mathbf{x}_I}{\varrho}\right). \tag{5.6}$$

Since the least square fit (eq. (5.2)) is weighted by a function Φ which has compact support, the local character of the approximation $u^h(\mathbf{x})$ is ensured. With increasing particle density the weight function support can be chosen to be correspondingly smaller and the approximation $u^h(\mathbf{x})$ converges for $\varrho \to 0$ to the exact function $u(\mathbf{x})$.

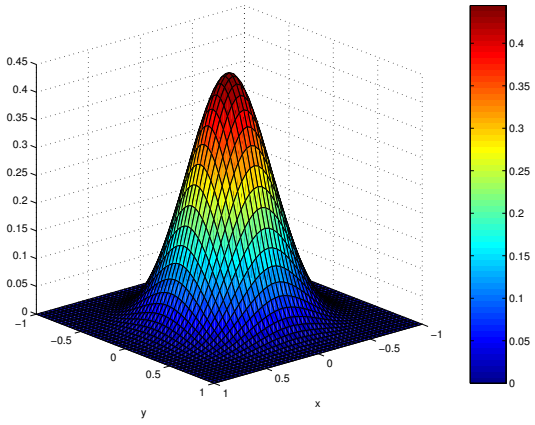

Figure 5.2: Two-dimensional weight function $\Phi = w\left(\frac{x}{\varrho}\right) w\left(\frac{y}{\varrho}\right)$ based on a cubic spline [133].

The smoothness of the MLS approximation is determined by the invertibility requirement of eq. (5.4) as well by eq. (5.3). This is as both expressions depend on the continuity of the basis polynomial $\mathbf{P} \in C^m(\Omega)$ as well as the weight function $\Phi \in C^l(\Omega)$ and it holds $u^h(\mathbf{x}) \in C^k$ with $k = \min(l, m)$ [131]. A complete linear basis polynomial

$$\mathbf{P}(\mathbf{x}) \;=\; [1,\, x,\, y,\, z]\,, \tag{5.7}$$

together with a weight function based on a cubic spline

$$w(r) = \begin{cases} \frac{2}{3} - 4r^2 + 4r^3 & \text{for } |r| \leq \frac{1}{2} \\ \frac{4}{3} - 4r + 4r^2 - \frac{4}{3}r^3 & \text{for } \frac{1}{2} < |r| < 1 \\ 0 & \text{for } |r| > 1 \end{cases} \tag{5.8}$$

is chosen. For the three-dimensional space the weight function can be constructed by the following expression

$$\Phi\left(\frac{\mathbf{x} - \mathbf{x}_I}{\varrho}\right) = w\left(\frac{x - x_I}{\varrho}\right) w\left(\frac{y - y_I}{\varrho}\right) w\left(\frac{z - z_I}{\varrho}\right). \tag{5.9}$$

The two-dimensional weight function is shown in Fig. 5.2. Note that the influence radius ϱ may be chosen independently and differently for each coordinate direction and particle. Therefore, the MLS approximation scheme can be adapted to any irregular particle distribution as well as to domain geometries which are much smaller in one or two coordinate directions. Considering that $\mathbf{P} \in C^1(\Omega)$ as well as $\Phi \in C^1(\Omega)$ it follows that the MLS approximation eq. (5.3) also provides $C^1(\Omega)$ smoothness.

5.1.2 Modified Boundary Collocation Method

It is important to note that, unlike FEM shape functions, the MLS shape functions do not satisfy the Kronecker delta property. This means that, at the particles, the particle parameters are not equal to the value of the approximated field at that point. Dirichlet boundary conditions cannot be directly enforced as easily as in FEM. The Dirichlet boundary conditions were enforced using the Modified Boundary Collocation Method [8]. This method enforces the Dirichlet condition exactly by modifying the linear system after it has been assembled.

5.1.3 Gaussian Integration

Numerical integration of integrals resulting from the formulation were performed using Gaussian integration over elements of the mesh that were used to discretise the domain. This introduces a certain mesh dependency and means that the full numerical method is not truly meshless, since the geometry is approximated by

FEM shape functions. Second order Gaussian quadrature was used.

5.1.4 Particle Distribution

The particle distribution used to represent the geometry was calculated by creating a hexahedral or tetrahedral mesh of the geometry in the software package Gid [134]. The nodal positions of the mesh elements were then taken to represent the particles used in the element-free Galerkin method and input into SESKA. The mesh was also used for Gaussian integration of integrals over the domain.

5.1.5 Newton's Method

To apply the element free Galerkin method the variational formulations of the eikonal diffusion equation and mechanics problem were found. This resulted in a scalar functional $W(u)$ in the case of the eikonal diffusion equation and $\delta\Psi(\mathbf{u})$ in the case of the mechanics problem. The solution procedure for the mechanics problem is outlined below. The eikonal diffusion equation was solved in the same way replacing the displacement vectors $\mathbf{u}$ with the scalar depolarisation time u . To solve these equations the system was linearised using a first order Taylor expansion about the point $\mathbf{u}_0$ to obtain

$$\begin{aligned} \delta\Psi(\mathbf{u}_0+\Delta\mathbf{u}) &\approx \delta\Psi(\mathbf{u}_0)+\Delta\delta\Psi(\mathbf{u}) \\ &\approx \delta\Psi(\mathbf{u}_0)+\left.\frac{\partial\delta\Psi(\mathbf{u})}{\partial\mathbf{u}}\right|_{\mathbf{u}_0}\cdot\Delta\mathbf{u} \end{aligned} \tag{5.10}$$

where $\Delta\mathbf{u}$ is the incremental displacement field such that $\mathbf{u}=\mathbf{u}_0+\Delta\mathbf{u}$ and $\Delta\delta\Psi(\mathbf{u}) = \left.\frac{\partial\delta\Psi(\mathbf{u})}{\partial\mathbf{u}}\right|_{\mathbf{u}_0}\cdot\Delta\mathbf{u}$ is the variation of $\delta\Psi(\mathbf{u})$ with respect to $\Delta\mathbf{u}$ (or equivalently the directional derivative in the direction of $\Delta\mathbf{u}$).

The functional $\delta\Psi(\mathbf{u})$ is equated to zero to to find the displacement $\mathbf{u}$ satisfying $\delta\Psi(\mathbf{u})=0$. The linearisation of $\delta\Psi(\mathbf{u})$ is then approximately zero

$$\delta\Psi(\mathbf{u}_0)+\left.\frac{\partial\delta\Psi(\mathbf{u})}{\partial\mathbf{u}}\right|_{\mathbf{u}_0}\cdot\Delta\mathbf{u}\approx 0 \tag{5.11}$$

Eq. (5.11) was discretised using EFGM through eq. (5.5) to obtain a linear system of the form

$$\mathbf{F}(\mathbf{u})+\mathbf{K}(\mathbf{u})\,\Delta\overline{\mathbf{u}}\approx 0 \tag{5.12}$$

where $\mathbf{F}$ is the discretisation of $G(\mathbf{u}_0)$, $\mathbf{K}$, the tangent matrix, is the discretisation of $\frac{\partial G(\mathbf{u})}{\partial \mathbf{u}}\Big|_{\mathbf{u}_0}$ and $\Delta\overline{\mathbf{u}}$ is the discretised displacement vector consisting of the particle parameters u_I (equivalent to degrees of freedom in FEM).

Unless the equations are linear there is no equality in eq. (5.12). The equations that were considered here were both nonlinear and an iterative procedure, Newton's method, was required to solve the system for $\Delta\overline{\mathbf{u}}$. In iteration 0 of Newton's method an initial guess $\mathbf{u}^0$ for the solution of eq. (5.12) is chosen. Using $\mathbf{u}_0$ to calculate $\mathbf{F}(\mathbf{u}^0)$ and $\mathbf{K}(\mathbf{u}^0)$ the system is solved to find the increment $\Delta\mathbf{u}^0$. The initial guess is then updated using the increment calculated as

$$\mathbf{u}^{i+1} = \mathbf{u}^i + \Delta\mathbf{u}^i \tag{5.13}$$

to find the displacement $\mathbf{u}^{i+1}$ that will be used as displacement to calculate $\mathbf{F}$ and $\mathbf{K}$ for the next Newton iteration. This procedure of solving the linear system for $\Delta\mathbf{u}^i$ then updating the displacement is repeated until $\mathbf{u}^{i+1}$ converges to the solution i.e. $\Delta\mathbf{u}^i$ is less than a desired tolerance. Quadratic convergence is ensured if the initial guess, $\mathbf{u}^0$, is close enough to the actual solution.

Note that the Newton's method was used at each time step to calculate the solution for the loading applied at that time step. The solution from the previous time step was used as an initial guess for the first Newton iteration. Before the simulation begins and there is no loading the zero vector is a solution and was thus used as the initial guess for the first time step. Because the initial guess should be close to the solution time steps should be small enough to ensure convergence of the method.

5.2 Eikonal Diffusion Equation

5.2.1 Weak Form

The strong form of the eikonal diffusion equation is

$$c_0\sqrt{\nabla u \cdot \mathbf{M}\nabla u} - \nabla\cdot(\mathbf{M}\nabla u) = \tau_m \quad \text{in } \mathcal{B} \tag{5.14}$$

$$\mathbf{n}\cdot\mathbf{M}\nabla u = 0 \quad \text{in } \partial\mathcal{B}_{\mathcal{N}} \tag{5.15}$$

$$u = \hat{u} \quad \text{in } \partial\mathcal{B}_D \tag{5.16}$$

In order to implement the standard Galerkin method, the weak form, or variational formulation, of the problem was calculated. Multiplying by a scalar test function δv that is assumed to be zero on the Dirichlet boundary and integrating over $\mathcal{B}$

$$W = \int_{\mathcal{B}} \left\{ c_0 \sqrt{\nabla u \cdot \mathbf{M} \nabla u} \delta v + \nabla \cdot (\mathbf{M} \nabla u) \, \delta v - \tau_m \delta v \right\} dV = 0 \tag{5.17}$$

and integrating the second term by parts

$$\begin{aligned} W &= \int_{\mathcal{B}} \left\{ c_0 \sqrt{\nabla u \cdot \mathbf{M} \nabla u} \delta v + (\mathbf{M} \nabla u) \cdot \nabla \delta v - \tau_m \delta v \right\} dV \\ &\quad - \int_{\partial \mathcal{B}_D} (\mathbf{M} \nabla u) \cdot \mathbf{n} \delta v dA = 0. \end{aligned} \tag{5.18}$$

Note that along the Neumann boundary $\partial \mathcal{B}_N$ the term under the integral is zero so the integral is only over the Dirichlet boundary. This enforces the Neumann boundary condition. The term involving the integral over the Dirichlet boundary is also zero since the test functions are zero on $\partial \mathcal{B}_D$ resulting in the following weak form

$$W(u) = \int_{\mathcal{B}} \left\{ c_0 \sqrt{\nabla u \cdot \mathbf{M} \nabla u} \delta v + (\mathbf{M} \nabla u) \cdot \nabla \delta v - \tau_m \delta v \right\} dV = 0 \tag{5.19}$$

5.2.2 Linearisation

To solve this nonlinear system of equations the Newton's method was used. This required the linearisation of the variational formulation introduced in eq. (5.19). To find the linearisation, the Taylor expansion of the functional $W(u)$ was computed (see eq. (5.10)):

$$W(u) \approx W(u_0) + \frac{\partial W}{\partial u} \Delta u = 0, \tag{5.20}$$

where the variation is given by

$$\frac{\partial W}{\partial u} \Delta u = \int_{\mathcal{B}} c_0 \frac{\nabla u \cdot \mathbf{M} \nabla (\Delta u)}{\sqrt{\nabla u \cdot \mathbf{M} \nabla u}} \delta v dV + \int_{\mathcal{B}} (\mathbf{M} \nabla (\Delta u)) \cdot \nabla \delta v dV$$

where Δu is an increment of the depolarisation time u. The fact that $\mathbf{M}$ is symmetric was used to simplify the expressions in eq. (5.20).

5.3 Mechanics Equation

5.3.1 Variational Formulation

The variational formulation of continuum mechanics (eq. (2.25)) is given as

$$\delta\Psi = \int_{\mathcal{B}} \mathbf{S} : \delta\mathbf{E} dV - \int_{\partial\mathcal{B}_N} pJ\mathbf{F}^{-T}\mathbf{N} \cdot \delta\mathbf{u} dA = 0, \tag{5.21}$$

where the body force term has been omitted as it is negligible in cardiac mechanics. The pressure term was expressed in the reference configuration using eq. (2.4) since the pressure was defined in the current configuration. The second Piola-Kirchhoff stress tensor $\mathbf{S}$ is defined as the sum via the passive stress $\mathbf{S}_P$ and the active stress $\mathbf{S}_A$ so that $\mathbf{S} = \mathbf{S}_P + \mathbf{S}_A$. The passive stress is given by eq. (4.12) while the active stress is given by eq. (4.15).

5.3.2 Linearisation

Eq. (5.21) is nonlinear so it was necessary to linearise the equation. This resulted in

$$\begin{aligned} \delta\Psi(\mathbf{u}) \approx\ & \delta\Psi(\mathbf{u}_0) + \int_{\mathcal{B}} \left[\Delta\mathbf{S} : \delta\mathbf{E} + \int_{\mathcal{B}} \mathbf{S} : \Delta\delta\mathbf{E} \right] dV \\ & -\Delta \left[\int_{\partial\mathcal{B}_N} pJ \left(\mathbf{F}^{-T}\mathbf{N} \right) \cdot \delta\mathbf{u} dA \right] = 0. \end{aligned} \tag{5.22}$$

Because the second Piola-Kirchhoff stress tensor is expressed in terms of the Green strain, it is convenient to express the variation of the stress tensor with respect to the Green strain so that

$$\Delta\mathbf{S} = \frac{\partial\mathbf{S}_P}{\partial\mathbf{E}} \cdot \Delta\mathbf{E} + \frac{\partial\mathbf{S}_A}{\partial\mathbf{E}} \cdot \Delta\mathbf{E}. \tag{5.23}$$

The tensor $\frac{\partial\mathbf{S}_P}{\partial\mathbf{E}} = {}^{\partial^2\psi_P}/_{\partial\mathbf{E}\partial\mathbf{E}}$ is often called the constitutive tensor (in this case

the passive constitutive tensor). It was calculated to be

$$\begin{aligned}\frac{\partial^2\psi_P}{\partial\mathbf{E}\partial\mathbf{E}} &= \left\{\frac{1}{2}Ae^Q\left[\frac{\partial Q}{\partial\mathbf{E}}\otimes\frac{\partial Q}{\partial\mathbf{E}}+\frac{\partial^2 Q}{\partial\mathbf{E}\partial\mathbf{E}}\right]\right.\\ &\left.+A_{comp}\left[\mathbf{C}^{-1}\otimes\mathbf{C}^{-1}J\ln J+\frac{\partial\mathbf{C}^{-1}}{\partial\mathbf{E}}\left(J\ln J-J+1\right)\right]\right\}, \quad (5.24)\end{aligned}$$

where $\frac{\partial Q}{\partial\mathbf{E}}$ has been derived in eq. (4.13), $\frac{\partial^2 Q}{\partial\mathbf{E}\partial\mathbf{E}}$ is given by

$$\begin{aligned}\frac{\partial^2 Q}{\partial\mathbf{E}\partial\mathbf{E}} &= 2a_1\mathbf{M}_1\otimes\mathbf{M}_1+2a_2\mathbf{M}_2\otimes\mathbf{M}_2+2a_3\mathbf{M}_3\otimes\mathbf{M}_3\\ &+\left\{a_4\left[\delta_{ik}\left(M_1\right)_{lj}+\left(M_1\right)_{ik}\delta_{lj}\right]+a_5\left[\delta_{ik}\left(M_2\right)_{lj}+\left(M_2\right)_{ik}\delta_{lj}\right]\right.\\ &\left.+a_6\left[\delta_{ik}\left(M_3\right)_{lj}+\left(M_3\right)_{ik}\delta_{lj}\right]\right\}\mathbf{e}_i\otimes\mathbf{e}_j\otimes\mathbf{e}_k\otimes\mathbf{e}_l, \quad (5.25)\end{aligned}$$

and $\frac{\partial\mathbf{C}^{-1}}{\partial\mathbf{E}}$ can be written as

$$\frac{\partial\mathbf{C}^{-1}}{\partial\mathbf{E}}=-\left(C^{-1}_{ik}C^{-1}_{jl}+C^{-1}_{jk}C^{-1}_{il}\right)\mathbf{e}_i\otimes\mathbf{e}_j\otimes\mathbf{e}_k\otimes\mathbf{e}_l. \quad (5.26)$$

It is important to note that the constitutive tensor, expressed here with indices exposed $\frac{\partial^2\psi_P}{\partial E_{ij}\partial E_{kl}}\mathbf{e}_i\otimes\mathbf{e}_j\otimes\mathbf{e}_k\otimes\mathbf{e}_l$, is symmetric in the ij indices and the kl indices. This is due to the symmetry of $\mathbf{E}$.

The active constitutive tensor $\frac{\partial\mathbf{S}_A}{\partial\mathbf{E}}$ is given by

$$\frac{\partial\mathbf{S}_A}{\partial\mathbf{E}}=\mathbf{M}_1\otimes\frac{\partial T_A}{\partial\mathbf{E}}, \quad (5.27)$$

where $\frac{\partial T_A}{\partial\mathbf{E}}$ is given by

$$\begin{aligned}\frac{\partial T_A}{\partial\mathbf{E}} &= \frac{\partial T_A}{\partial l}\frac{\partial l}{\partial\mathbf{E}}\\ &= T_{max}\left\{-\frac{1}{2}\frac{Ca_0^2}{Ca_0^2+ECa_{50}^2\left(l\right)}\sin\left(\omega\left(l,t\right)\right)\frac{\partial\omega}{\partial l}\right.\\ &\left.+\left[\frac{Ca_0\left(ECa_{50}\left(l\right)\right)^2}{\left(Ca_0\right)_{max}\left(Ca_0^2+ECa_{50}^2\left(l\right)\right)}\right]^2 B\,C_t\left(l,t\right)\,e^{(B(l-l_0))}\right\}\frac{l_R}{\sqrt{2I_4+1}}\mathbf{M}_1. \quad (5.28)\end{aligned}$$

Note that the active constitutive tensor $\left(M_1\right)_{ij}\frac{\partial T_A}{\partial E_{kl}}$ is also symmetric about the

ij indices and the kl indices due to the symmetry of $\mathbf{M}_1$ and $\mathbf{E}$ respectively.

The variation of external work (the pressure term) can be calculated to be

$$\begin{aligned}\Delta\left[\int_{\partial\mathcal{B}_N} pJ\left(\mathbf{F}^{-T}\mathbf{N}\right)\cdot\delta\mathbf{u}dA\right] &= \int_{\partial\mathcal{B}_N} p\left(\frac{\partial J}{\partial F_{kl}}F^{-1}_{ji}+J\frac{\partial F^{-1}_{ji}}{\partial F_{kl}}\right)N_j\Delta u_{k,l}\delta u_i dA \\ &= \int_{\partial\mathcal{B}_N}\left(pJF^{-1}_{ik}F^{-1}_{ji}-pJF^{-1}_{jk}F^{-1}_{li}\right)N_j\Delta u_{k,l}\delta u_i dA.\end{aligned} \tag{5.29}$$

As mentioned in Section 5.1.5, the linearisation of the variational formulation with respect to displacement $\mathbf{u}$, often termed the second variation, results in a tangent matrix $\mathbf{K}(\mathbf{u})$ multiplied by a displacement increment $\Delta\mathbf{u}$ and a force vector $\mathbf{F}$. The contribution to the tangent matrix can be evaluated from the second term of eq. (5.22) by converting to index notation:

$$\begin{aligned}&\int_{\mathcal{B}}\Delta\mathbf{S}:\delta\mathbf{E}dV+\int_{\mathcal{B}}\mathbf{S}:\Delta\delta\mathbf{E}dV-\Delta\left[\int_{\partial\mathcal{B}_N}pJ\left(\mathbf{F}^{-T}\mathbf{N}\right)\cdot\delta\mathbf{u}dA\right]= \\ &\quad\int_{\mathcal{B}}\Delta S_{ij}\delta E_{ij}dV+\int_{\mathcal{B}}S_{ij}\Delta\delta E_{ij}dV-\Delta\left[\int_{\partial\mathcal{B}_N}pJF^{-1}_{ji}N_j\delta u_i dA\right].\end{aligned} \tag{5.30}$$

The mechanics problem should be solved for the displacement. For this consider the variational and linearised forms of the Green strain:

$$\delta E_{ij} = \frac{1}{2}\left(\delta u_{k,j}F_{ki}+\delta u_{k,i}F_{kj}\right), \tag{5.31}$$

$$\Delta E_{ij} = \frac{1}{2}\left(\Delta u_{k,j}F_{ki}+\Delta u_{k,i}F_{kj}\right), \tag{5.32}$$

$$\Delta\delta E_{ij} = \frac{1}{2}\left(\delta u_{k,i}\Delta u_{k,j}+\Delta u_{k,i}\delta u_{k,j}\right), \tag{5.33}$$

where a comma in the subscript denotes derivative with respect to the material coordinates, i.e. $\delta u_{i,j}=\partial u_i/\partial u_j$ noting that $\Delta\delta u_i=0$.

$$\begin{aligned}&\int_{\mathcal{B}}\Delta S_{ij}\delta E_{ij}dV+\int_{\mathcal{B}}S_{ij}\Delta\delta E_{ij}dV \\ &=\int_{\mathcal{B}}\left(\frac{\partial^2\psi_P}{\partial E_{ij}\partial E_{kl}}+(M_1)_{ij}\frac{\partial T_A}{\partial E_{kl}}\right)\Delta u_{m,l}F_{mk}\delta u_{n,j}F_{ni}+\int_{\mathcal{B}}\delta u_{k,i}S_{ij}\Delta u_{k,j} \\ &\quad-\int_{\partial\mathcal{B}_N}\left(pJF^{-1}_{ik}F^{-1}_{ji}-pJF^{-1}_{jk}F^{-1}_{li}\right)N_j\Delta u_{k,l}\delta u_i dA\end{aligned} \tag{5.34}$$

where symmetry of the constitutive tensor was used to simplify the expression. The tangent matrix was obtained from eq. (5.34) by discretising Δu_i and δu_j.

5.3.3 Incremental Loading

To solve the variational formulation of continuum mechanics for a specified load it is necessary to solve the equations for incrementally increasing load. This is because Newton's method will only converge if the initial guess, taken to be the solution at the previous load step, is close enough to the solution.

This was achieved by multiplying the pressure by a loading factor λ_n at step n. If the desired pressure is p_0 then the pressure at calculation step n is

$$p = \lambda_n p_0 \tag{5.35}$$

Clearly the loading factor should increase from zero to one over the calculation. The loading increment at each calculation step is the difference between the current loading factor and the previous loading factor i.e.

$$\Delta\lambda_n = \lambda_n - \lambda_{n-1}. \tag{5.36}$$

Each load step corresponded to an equivalent time step so that the temporal dynamics of the cardiac cycle could be analysed. Expressing the pressure as a loading factor multiplied by the desired pressure results in the following form of the pressure term in the variational formulation

$$\int_{\partial\mathcal{B}_N} pJ\mathbf{F}^{-T}\mathbf{N}\cdot\delta\mathbf{u}dA = \lambda_n\int_{\partial\mathcal{B}_N} p_0 J\mathbf{F}^{-T}\mathbf{N}\cdot\delta\mathbf{u}dA. \tag{5.37}$$

5.3.4 Isovolumetric Loading

During the isovolumetric contraction and isovolumetric relaxation phases of the cardiac cycle the cavity volume must remain zero due to closed valves. During these phases the non-zero active stress that tries to reduce the cavity volume by

contracting the ellipsoid whereas the non-zero cavity pressure seeks to increase the cavity volume (it is always positive). If these two forces balance then the cavity volume can be constrained.

The active stress is not known *a priori* as it is calculated implicitly from the strain. The magnitude of the pressure boundary condition on the other hand is not dependent on the deformation. It is therefore required to calculate the pressure needed to keep the cavity volume constant at each time step.

The requirement that $\Delta V = 0$ implies that at time step n and Newton iteration i the residual of the equation system is zero

$$\boldsymbol{\Psi}_n^i\left(\mathbf{u}_n^i\right) + \Delta\lambda_n^i \mathbf{f}_{ext} = \mathbf{K}_n^i \Delta\mathbf{u}_n^i = \mathbf{0} \tag{5.38}$$

where $\boldsymbol{\Psi}_n^i\left(\mathbf{u}_n^i\right)$ is the contribution of the material response, $\Delta\lambda_n^i$ is the increment of the loading factor and $\Delta\lambda_n^i \mathbf{f}_{ext}$ is the contribution from the external work vector (the discretisation of the applied forces) all at time step n and Newton iteration i.

Rearranging this equation

$$\begin{aligned} \Delta\mathbf{u}_n^i &= \left(\mathbf{K}_n^i\right)^{-1} \boldsymbol{\Psi}_n^i\left(\mathbf{u}_n^i\right) + \Delta\lambda_n^i \left(\mathbf{K}_n^i\right)^{-1} \mathbf{f}_{ext} \\ &= \Delta\mathbf{u}_{\boldsymbol{\Psi},n}^i + \Delta\lambda_n^i \mathbf{u}_{ext,n}^i = \mathbf{0} \end{aligned} \tag{5.39}$$

where $\mathbf{u}_{ext,n}^i$ can be interpreted as the displacement due to the reference external load with $\lambda_n = 1$, while $\Delta\mathbf{u}_{\boldsymbol{\Psi},n}^i$ may be interpreted as the displacement increment due to the internal forces of the material.

The volume change ΔV_n over a time step can be computed as

$$\Delta V_n = \sum_{k=0}^{i-1}\left[\Delta V_n^k\left(\Delta\mathbf{u}_n^k\right)\right] + \Delta V_n^i = 0 \tag{5.40}$$

where $\sum_{k=0}^{i-1}\left[\Delta V_n^k\left(\Delta\mathbf{u}_n^k\right)\right]$ is the accumulated volume change over the current time step i. Eq. (5.40) can be manipulated so that ΔV_n^i is in terms of the loading factor $\Delta\lambda_n^i$

$$\Delta V_n = \sum_{k=0}^{i-1}\left[\Delta V_n^k\left(\Delta\mathbf{u}_n^k\right)\right] + \left(\Delta\lambda_n^i \Delta V_{n,ext}^i\left(\mathbf{u}_{n,ext}\right) + \Delta V_n^i\left(\Delta\mathbf{u}_n^i\right)\right) = 0 \tag{5.41}$$

where $\Delta V^i_{n,ext}$ is the volume change due the reference external load and $\Delta V^i_n\left(\Delta \mathbf{u}^i_n\right)$ is the volume change from the preliminary displacement correction.

The loading factor can then be obtained from eq. (5.41) as

$$\Delta\lambda^i_n = \frac{\Delta V_n - \sum_{k=0}^{i-1}\left[\Delta V^k_n\left(\Delta \mathbf{u}^k_n\right)\right] - \Delta V^i_n\left(\Delta \mathbf{u}^i_n\right)}{\Delta V^i_{n,ext}\left(\mathbf{u}_{n,ext}\right)} \tag{5.42}$$

where ΔV_n is set . The loading factor computed is then used in the next Newton iteration as the new loading factor.

Note that for numerical reasons the incompressibility requirement on the cavity was relaxed so that $\Delta V_n \approx 0$. The loading factor was not changed if the change in volume divided by the change in pressure was less than a certain tolerance ${}^{\Delta V_n}/_{(\Delta\lambda_n p_0)} \leq tol$. This ensures the volume can only change by a maximum of $tol \times \Delta\lambda_n$ over a time step. This is so that if small pressure steps are taken, only a small volume change should be taken and if large pressure steps are taken, a larger volume change is allowed. In all simulations the cavity volume was constrained to change by a maximum of 1% of the cavity volume over each isovolumetric phase. If the initial cavity volume was V_0 and the pressure change over the phase was Δp then the tolerance was given by $tol = {}^{(0.01\times V_0)}/_{\Delta p}$.

5.4 Implementation

The eikonal diffusion equation and mechanics equations were solved using the in-house code SESKA. SESKA is a numerical code written in C++ to solve linear problems specifically in mechanics and electromechanics using meshless methods. SESKA is a large code of approximately 100 000 lines that is capable of modelling a number of different types of materials, constitutive laws and formulations.

The numerical formulation described above has been implemented in SESKA. Major parts of the code that were added to SESKA by the author for this thesis were:

- Eikonal diffusion model.
- Guccione active stress model.
- Fibre directions and prolate spheroidal support.

Being a parallel code SESKA can be run on large computing clusters. SESKA was run on the Centre for High Performance Computing SUN Computing Cluster using up to 64 cores as well as a in-house cluster.

Chapter 6

Results and Discussion

In this section the results of several electrophysiology and mechanics simulations are presented. First the electrophysiology is considered. The convergence of the numerical method was first demonstrated by comparing the exact solution of the eikonal diffusion equation to the numerical solution on coarse and fine meshes. The eikonal diffusion equation was then validated by comparison with two other computational studies. Calibration of the eikonal diffusion equation was performed by comparing numerical solutions in the ellipsoid model of the heart to experimental data.

The mechanics model was then investigated. The passive mechanical model was first validated with experimental pressure-volume data. The full cardiac cycle of the rat left ventricle was then simulated. The resulting pressure and volume relationships are discussed and validated with experimental data. Sarcomere length, representing the fibre strain, and active tension transients for a number of positions in the heart are presented and discussed.

Using the mechanics model the ischaemic phase of myocardial infarction was simulated for the full cardiac cycle. The infarction was modelled as being non-contractile and less stiff than the surrounding myocardium. Results from the infarcted model were then compared with experimental results.

6.1 Electrophysiology

6.1.1 Convergence of the Numerical Method

To show that the numerical solution found is accurate it was necessary to show convergence of the spatial discretisation and approximation scheme. The approximation scheme used was the MLS element free Galerkin method. Convergence was shown by solving an equation on the same domain with different levels of discretisation and showing that as the discretisation became finer the error decreased.

It was convenient to use the eikonal diffusion equation to achieve this since the exact solution of this equation is known for an infinite homogeneous domain (see Section 3.4.1). The eikonal diffusion equation was solved on a simple block geometry which served as an approximation to this infinite homogeneous domain. Three different particle distributions were produced with 400, 1450 and 3200 particles. Note that since the domain of the numerical solution was not identical to the domain of the exact solution some residual error was expected.

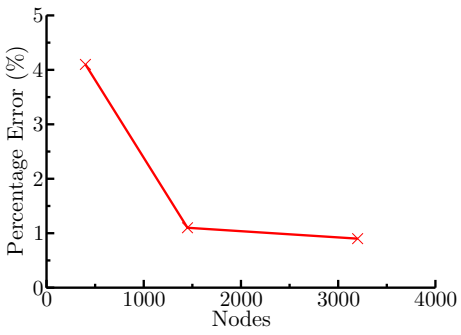

Figure 6.1: Error in numerical solution for 400, 1450 and 3200 particles.

The percentage error was determined by calculating the square of the difference between the numerical solution and the exact solution at each point, adding the contribution from each particle and dividing by the sum of the square of the exact solution at each node:

$$Error = \frac{\Sigma_{i=1}^{N} \left(u_i^{exact} - u_i^{approx}\right)^2}{\Sigma_{i=1}^{N} \left(u_i^{exact}\right)^2}, \tag{6.1}$$

where N is the number of particles, u_i^{exact} is the exact solution at particle i and u_i^{approx} is the numerical solution at particle i.

Fig. 6.1 shows the percentage error in the numerical solution. The error decreased successively from 4% for 400 particles to below 1% for 3200 particles. This shows the numerical solution tending to the exact solution for finer particle distributions.

6.1.2 Validation

The heart, however, is not homogeneous and fibre directions vary throughout. Noting this, numerical solutions of the eikonal diffusion equation were compared to those found in literature.

6.1.2.1 Myocardial Slab

The first study with which numerical solutions were compared was that of Colli-Franzone *et al.* [135]. Colli-Franzone numerically solved the eikonal diffusion equation using a finite difference scheme for a rectangular prism with sides $10mm$, $10mm$ and $3mm$. This is an idealisation of a slab of myocardium with the endocardium being on the plane $x_3 = 0$ and the epicardium on the plane $x_3 = 3mm$ (see Fig. 6.2).

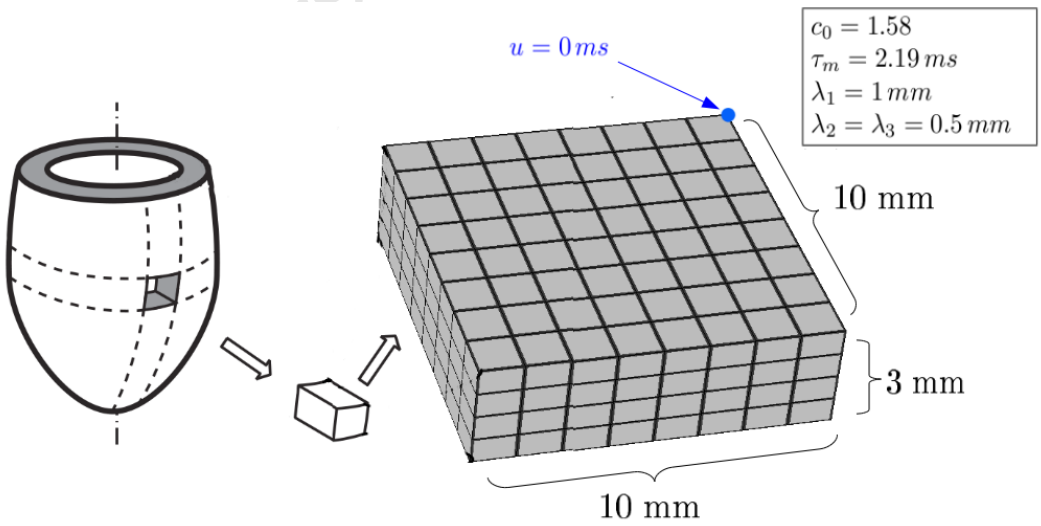

Figure 6.2: Myocardial slab geometry.

The fibre directions in [135] are given as

$$\mathbf{V}_1 = \mathbf{e}_1 \cos\alpha(r) + \mathbf{e}_2 \sin\alpha(r) \quad (6.2)$$

$$\mathbf{V}_2 = -\mathbf{e}_1 \sin\alpha(r) + \mathbf{e}_2 \cos\alpha(r) \quad (6.3)$$

$$\mathbf{V}_3 = \mathbf{e}_3 \quad (6.4)$$

where $\mathbf{e}_i$ are the Cartesian basis vectors, r is the normalised distance through the thickness of the slab from the endocardium ($r = 0$) to epicardium ($r = 1$) and

$$\alpha = {}^{2}/_{3}\pi(1 - r). \quad (6.5)$$

The form of the eikonal diffusion equation used in [135] was slightly different from the form used in this study, so the parameter values c_0 and τ_m were calculated. Parameter values $c_0 = 1.58$ and $\tau_m = 2.19ms$, with space constants $\lambda_1 = 1\,mm$ and $\lambda_2 = \lambda_3 = 0.5\,mm$ were calculated. This resulted in a plane wave velocity of $c_f = 0.72mm\,ms^{-1}$ in fibre direction and $c_s = 0.36mm\,ms^{-1}$ in the cross fibre direction. The units $mm\,ms^{-1}$ have been used to exemplify the characteristic length and time scales of the problem.

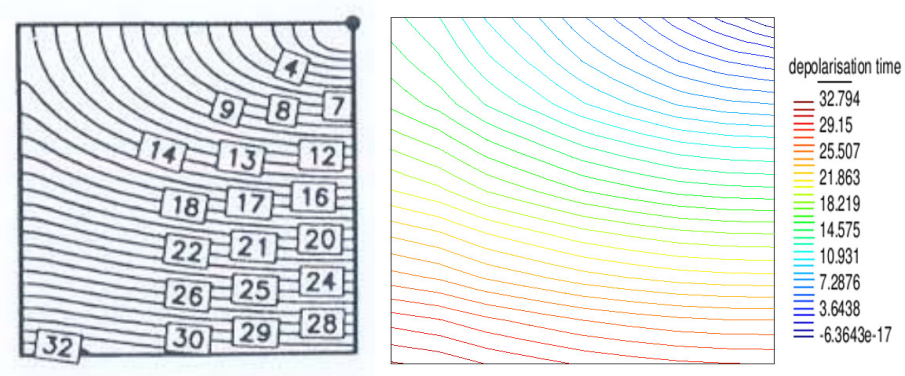

Figure 6.3: Solution to eikonal diffusion equation in the $z = 0$ plane for a myocardial slab with initial depolarisation in the upper right corner. On the left is the solution found in [135] and on the right is the solution obtained in this study. Units of depolarisation time are ms.

Fig. 6.3 shows the numerical solution and the solution of Colli-Franzone *et al.*. Notice how, due to the inhomogeneous fibre directions, the action potential propagated faster horizontally than vertically. In both this simulation and the Colli-Franzone simulation the action potential reached the bottom left corner in

approximately $33ms$. The slight difference between the solutions in the top right corner was due to the fact that Colli-Franzone used a small block as the depolarisation time boundary condition whereas in this simulation a more physiologically accurate point depolarisation time boundary condition was used.

To analyse the wave velocity of the numerical solution, consider the propagation of the wave in the horizontal direction from the point of stimulus. The wave took $\approx 14ms$ to reach the boundary $10mm$ away. The resulting wave velocity of $0.72mm\,ms^{-1}$ compared well with the calculated plane wave velocity of $c_f = 0.72mm\,ms^{-1}$. This was as expected since this wave has little curvature and is a good approximation of a plane wave. Similarly the wave travelling horizontally in the cross fibre direction reached the boundary $10mm$ away in $\approx 29ms$ resulting in a wave velocity of $0.35mm\,ms^{-1}$ compared to the calculated cross fibre plane wave velocity of $c_s = 0.36mm\,ms^{-1}$.

6.1.2.2 Annulus Geometry

The next geometry that was implemented was a thin cut through the heart wall, which resulted in a thin annulus (see Fig. 6.4). This was implemented to compare results with those of Tomlinson [98], where the eikonal diffusion equation was solved on a two dimensional annulus using FEM. While these geometries are not identical, they are very similar and a three dimensional geometry was significantly easier to implement with the existing code.

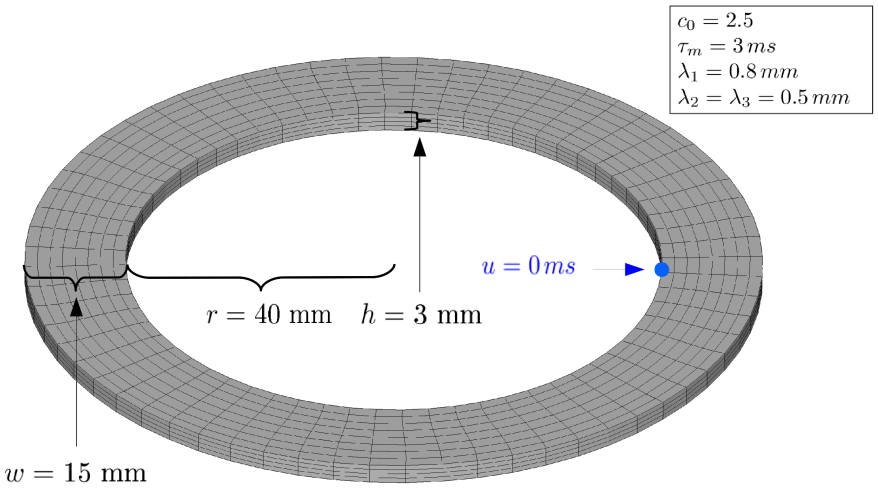

Figure 6.4: Thin annulus geometry used to compare results with Tomlinson.

The annulus has an inner radius of $40mm$, an outer radius of $55mm$, and a thickness of $3mm$, which corresponds to the dimensions of a human heart. Parameter values used were $c_0 = 2.5$, $\tau_m = 3ms$, $\lambda_l = 0.8mm$ and $\lambda_t = 0.5mm$. Circumferential fibre directions were used.

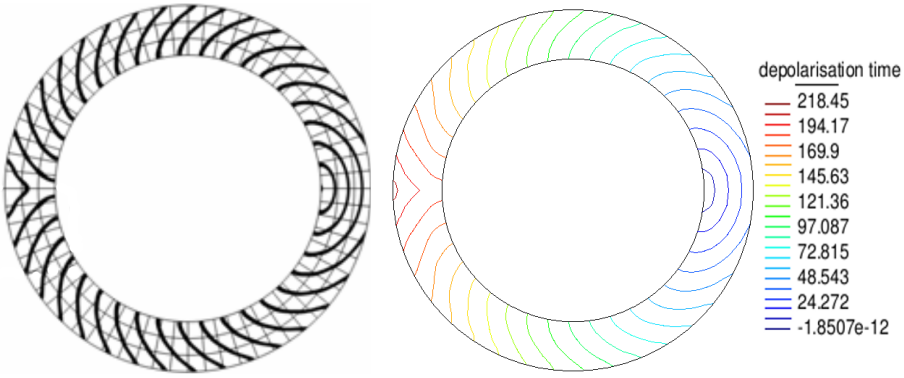

Figure 6.5: Solution to eikonal diffusion equation in the $z = 0$ plane for a thin annulus with initial depolarisation on the inner right-hand boundary. On the left is the solution found in [98] and on the right is the solution with this cardiac model. Intervals between contour lines are $10ms$ and units of depolarisation time are ms.

Fig. 6.5 shows the solution found by Tomlinson and the solution found in SESKA. The solutions were very similar as expected. The action potential reached the left wall in approximately $210ms$ for both simulations. In the Tomlinson solution the action potential propagation was slightly faster than in the SESKA solution, however this could be attributed to the fact that a three dimensional domain was used where additional diffusion can occur in the additional direction.

The exact plane wave propagation speed $c_f = 0.83mm\,ms^{-1}$ compared well with the numerical value found of $c_f = 0.75mm\,ms^{-1}$. The numerically found wave propagation speed was smaller due to the large curvature throughout the solution.

6.1.3 Calibration of Model

Once the accuracy of the numerical solution to the eikonal diffusion equation was shown the model was calibrated by comparing computational results with experimental results in the literature. Unfortunately detailed experimental data

of depolarisation times in rats is not available, so instead experimental depolarisation times of the human heart from Durrer *et al.* [9] were used to calibrate the spatial distribution of depolarisation times (see Fig. 3.7). Additionally, knowledge of the propagation speed found in rats was used to calibrate the propagation speed parameter of the eikonal equation [10].

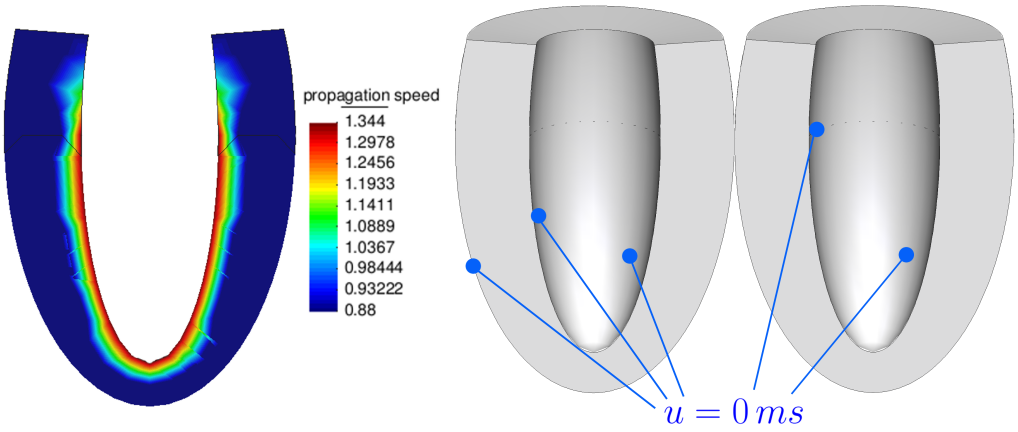

Figure 6.6: Problem configuration of electrophysiology model for the healthy left ventricle. Left: Propagation speed in the heart. Units used are $mm\,ms^{-1}$. Right: depolarisation time boundary conditions.

In the experimental depolarisation time map of Durrer (see Fig. 6.7) it can be seen that there are a number of points where the depolarisation wave is initiated. On the endocardium there are four distinct initiation points and there is an additional initiation point in the right ventricle on the wall of the septum that will affect the depolarisation times in the left ventricle (see Fig. 6.6). These five points were used as zero depolarisation time boundary conditions in the eikonal diffusion equation.

In Fig. 6.8 notice that the wave spreads much faster over the endocardium than through the heart wall from endocardium to epicardium. This is due to the Purkinje network that spreads over the endocardium. To simulate the Purkinje network the propagation speed on a thin strip about the endocardium was increased. As can be seen in Fig. 6.6 the propagation speed decreases transmurally through the heart wall from the endocardium to the epicardium. It was found that a propagation speed of $1.344 mm\,ms^{-1}$ over the endocardium gave ac-

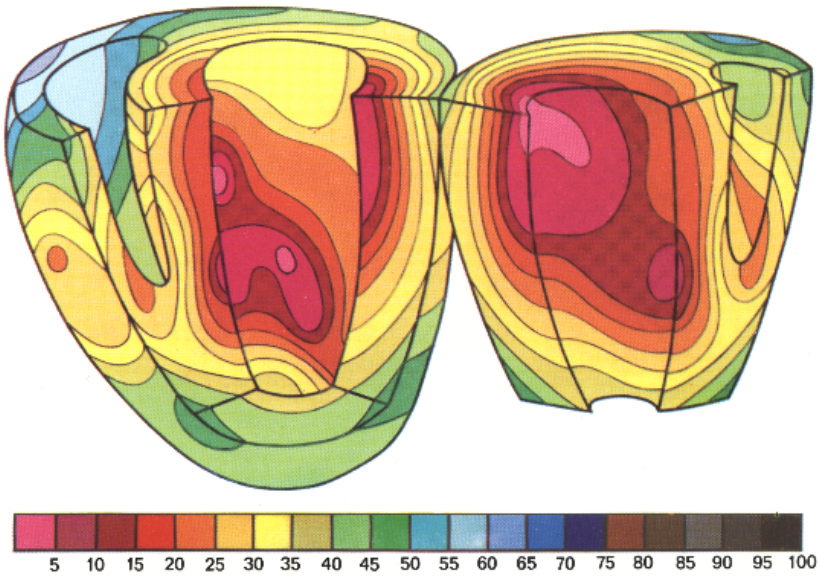

Figure 6.7: Depolarisation times in a human heart. Units are ms. Adapted from Durrer *et al.* [9].

curate results. Using these parameter values and boundary conditions the eikonal diffusion equation was solved numerically.

The propagation speed in the rat heart at body temperature has been found to be $\sim 0.9mm\,ms^{-1}$ [10]. It was found that, for simulations of the eikonal diffusion equation in this study, a value of $0.88mm\,ms^{-1}$ gave the best results.

Fig. 6.9 shows the depolarisation times on a cut through the equator of the ellipsoid. The cut goes through one of the initiation points that is situated on the equator. The solution was highly irregular and not symmetric, as expected, due to the irregular spatial positioning of the initiation points and the collisions of depolarisation waves propagating from the initiation points.

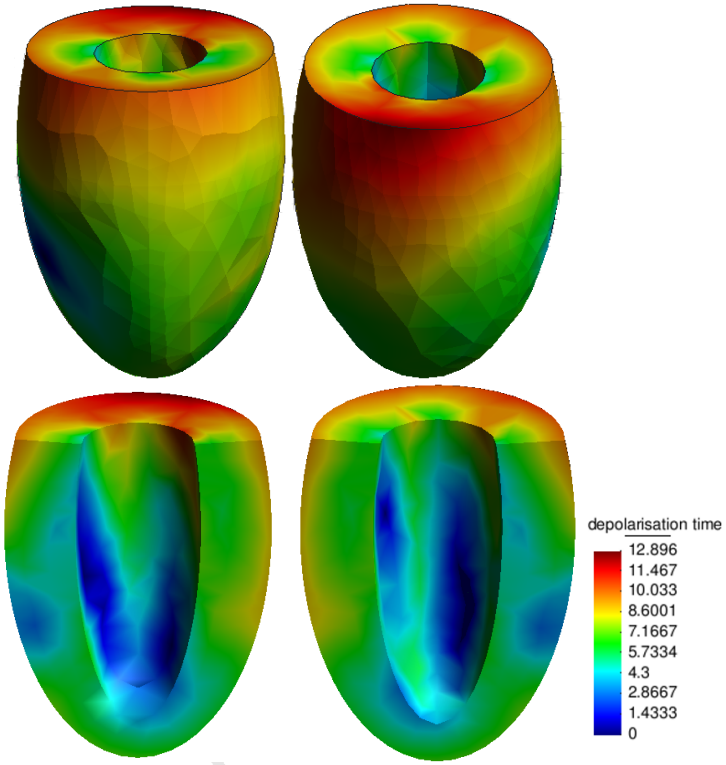

Figure 6.8: Depolarisation times of calibrated model . Top left: anterior (front) view. Top right: posterior (back) view. Bottom left: posterior half. Bottom right: anterior half. Units are in ms.

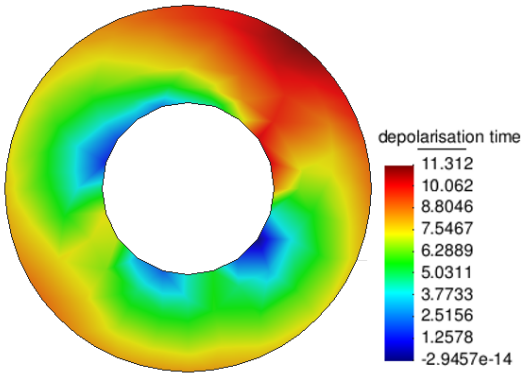

Figure 6.9: Depolarisation times on a cut through the equator of the ellipsoid. Units are in ms.

6.2 Mechanics Simulations

6.2.1 Validation

In order to validate the passive mechanical model a successively increasing pressure is applied to the endocardial wall of the ellipsoidal model of the left ventricle. The pressure was increased from $0kPa$ to $2kPa$ and results compared to experimental data.

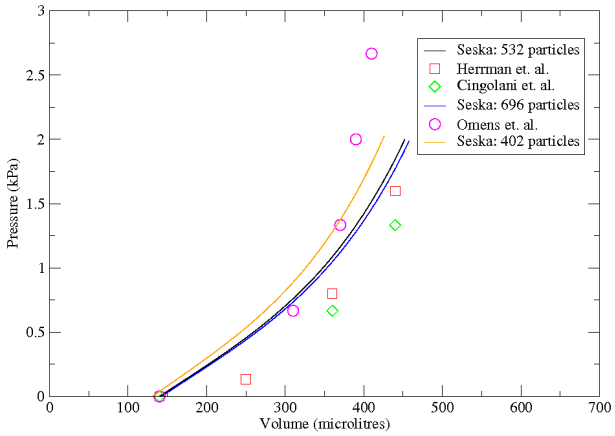

Figure 6.10: Volume pressure curve for diastolic filling. Experimental data was from in Herrman *et al.*, Cingolani *et al.* and Omens *et al.* [11–13].

Numerical solutions were calculated for particle distributions of 402, 532 and 696 particles. In Fig. 6.10 the left ventricle cavity pressure has been plotted against the cavity volume for each of the particle distributions as well as the experimental data found in Herrman *et al.*, Cingolani *et al.* and Omens *et al.* [11–13]. The shape of the numerical solution curves matches well with the trends in the experimental data. The numerical solutions are also within the range of the experimental data and so describe pressure volume relationships in this pressure range well.

As the density of the particle distribution increased from 402 to 696 particles the pressure-volume curve converged towards a fixed curve that was within experimental data. This suggested that particle distributions of 696 particles or more would provide accurate solutions.

6.2.2 Healthy Model

The full cardiac cycle of a rat left ventricle has been simulated. The geometry of a truncated ellipsoid was used to model the left ventricle using dimensions found in experimental data [13, 14]. Fibre directions from Rijcken *et al.* (see Section 4.5.2) were used to model the fibrous structure of the myocardium. The fibre directions in the ellipsoid as well as the applied boundary conditions are shown in Fig. 6.11. The mechanical model was not coupled to the eikonal diffusion equation. The depolarisation time at the end of diastole has been taken to be $1s$ at all points in the heart. The truncated ellipsoid representing the left ventricle was discretised to contain 731 particles. Results from the above validation study suggest that this number is sufficient for obtaining an accurate In Fig. solution to the mathematical equations.

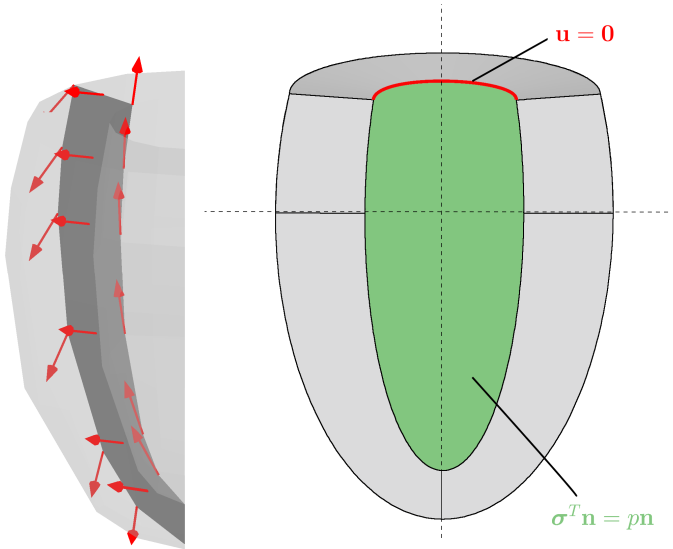

Figure 6.11: Problem configuration of mechanics simulation. Left: fibre directions in the ellipsoid. Right: boundary conditions applied to the ellipsoid.

Prior to the beginning of the cardiac cycle, the preload, the pressure on the endocardial wall was increased from $0kPa$ to $0.25kPa$. The cardiac cycle was separated into four phases. Nine representative time points have been selected from A-I and are shown in Fig. 6.12.

During the first phase, diastolic filling, a pressure was applied to the endocardial wall increasing from $0.25kPa$ to $1kPa$ in the $0s$ to $1s$ time interval. During

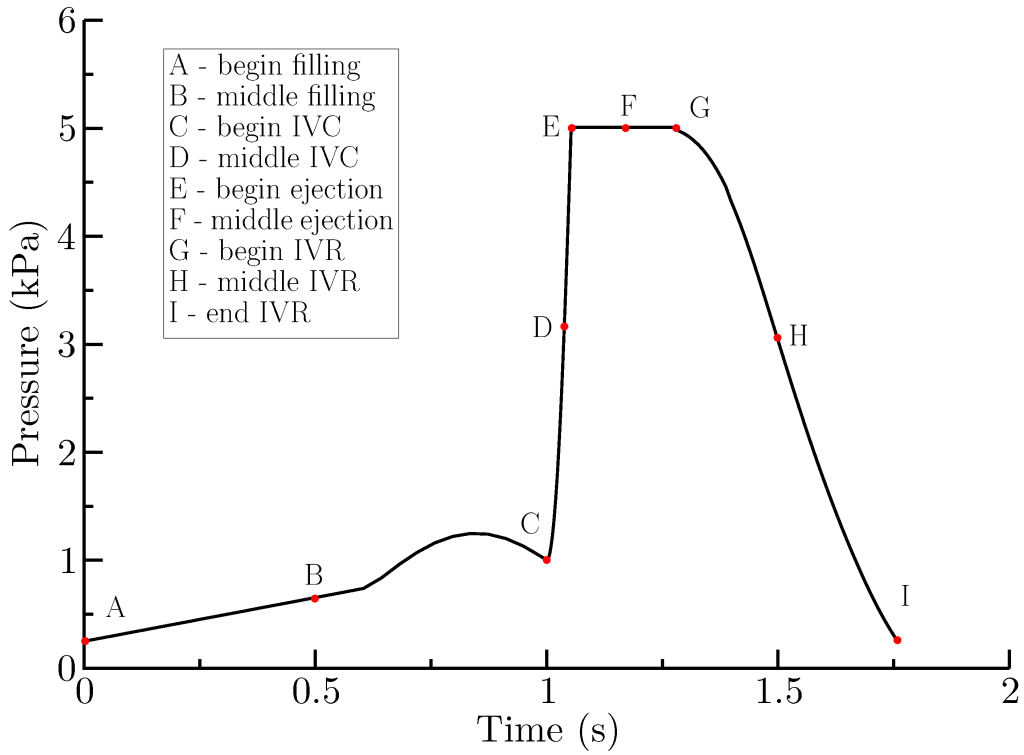

preload

Figure 6.12: Pressure-time curve for the healthy rat left ventricle. Representative time points in the cardiac cycle have been shown from A, the beginning of diastolic filling, to I, the end of isovolumetric relaxation.

the second phase, isovolumetric contraction, the cavity volume of the left ventricle was held constant while the active tension increased with each time step. The pressure on the endocardial wall correspondingly increased using the iterative cavity control algorithm. Once the pressure reached $5kPa$ the third phase, ejection, began. During ejection, the pressure was held constant at $5kPa$ while the active tension increased with each time step and cavity volume decreased. Once the cavity volume ceased to decrease, the last phase, isovolumetric relaxation, began. Here the cavity volume was held constant while the active tension in time decreased, and the pressure on the endocardial wall decreased.

Table 6.1 compares the results of the healthy simulation with experimental results of the healthy rat left ventricle. The end diastolic volume was found to be $348.02\mu L$ and the end systolic volume was $172.83\mu L$. This resulted in a stroke volume of $175.19\mu L$ and an ejection fraction of 50.34%. These results corresponded well with the experimental results of Faber *et al.* [15], where the

	Model Results	Experimental Data
EDV (μL)	348.02	397 ± 31 [14], 337 ± 26 [15], 450 ± 90 [16], 440 ± 53 [17], 299 ± 49 [18]
ESV (μL)	172.83	157 ± 18 [14], 172 ± 21 [15], 180 ± 30 [16], 190 [17], 194 ± 47 [18]
EDP (kPa)	1.0	1.19 ± 0.21 [17], 0.44 ± 0.17 [16], 2.0 ± 0.67 [18], 1.33 ± 0.27 [15]
ESP (kPa)	5.0	16.7 ± 0.93 [17], 12 ± 2.67 [16], 16.9 ± 1.12 [18], 12.4 ± 0.80 [15]
EF (%)	50.34	61 [14], 49 [15], 60 [16], 55 [17], 35 [18]

Table 6.1: Summary of healthy model results compared with experimental data. EDV - end diastolic volume, ESV - end diastolic pressure, ESP - end systolic pressure and EF - ejection fraction.

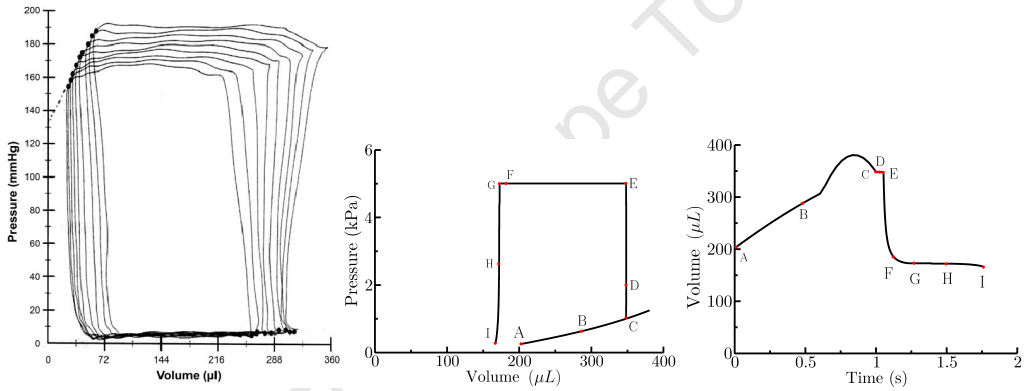

Figure 6.13: Basic metrics of cardiac function over the cardiac cycle. Left: Experimental pressure-volume loop [17]. Centre: Computational pressure-volume loop. Right: Volume-time curve.

end diastolic volume was $337 \pm 26 \mu L$, the end systolic volume $172 \pm 21 \mu L$ and the ejection fraction 49% . Other experimental studies report an ejection fraction of $49 - 60\%$ which is consistent with our results. The end diastolic volume and end systolic volume parameters vary greatly in the literature due to the variation in rat heart sizes [14–18].

Figs. 6.12 and 6.13 show the results of the simulation in the form of three graphs comparing the pressure, volume and time of the cardiac cycle. The first plot in fig. 6.13 shows an experimentally found pressure-volume loop in the rat left ventricle. This loop was compared to the second plot, showing the pressure-volume loop that was found in the mechanics simulation. The shape of the curves

are very similar with a characteristically flat top showing an almost constant pressure during ejection. The magnitude of the loops are very different however. The experimental loop reaches $\sim 160mmHg \approx 20kPa$ whereas the computational loop reaches $5kPa$.

The pressure-time curve shows the pressure transient during the cardiac cycle. The hump at $0.8s$ is the atrial systole (contraction of the atria) that pumps blood into the ventricles. In addition a small volume of blood returns to the left atrium during atrial systole, as the mitral valve is still open. The sharp upward curve following this shows the rapid increase in pressure that occurs during isovolumetric contraction. Isovolumetric contraction in this simulation had a period of $\sim 50ms$, which was consistent with the computational results of Niederer *et al.* [118]. Following this, during ejection, the volume decreases rapidly due to the increase in active tension, until the maximum tension is reached at $t = 1.25s$. Having the pressure remain constant is not fully physiological, but it is a good approximation to the relatively flat pressure-volume curves of rat left ventricles [18]. Ejection ends when the cavity volume stops decreasing, signalling the beginning of isovolumetric relaxation. During isovolumetric relaxation the active tension decreases from the maximum that occured at $t = 1.25s$. This continues until the pressure reaches $0.25kPa$. The timings of the different phases of the cardiac cycle are summarised in Table 6.2.

	A	B	C	D	E	F	G	H	I
t (s)	0	0.5	1.0	1.025	1.050	1.160	1.250	1.500	1.745

Table 6.2: Representative time point values for the healthy cardiac cycle.

Fig. 6.14 shows the sarcomere length distribution as well as the deformation of the ellipsoid for representative time points A-I during the cardiac cycle. The sarcomere length represents the fibre strain in the heart and is useful to assess areas in which there is overstretching or under-stretching. Note that the sarcomere length in the reference configuration varies transmurally from endocardium to epicardium because of the residual stress in the heart. Several cuts were made in the ellipsoid model at $z = 2, -2, -6$ to better elucidate the transmural gradients in sarcomere length. A vertical slice is also shown so that the torsion of the heart is visible.

During diastolic filling (plots A-C) the cavity volume can clearly be seen to

increase due to the increase in pressure. At point A the sarcomere length varies transmurally through the heart wall from $1.8\mu m$ to $1.95\mu m$. This increases up until the end of diastolic filling where the sarcomere length is at a maximum over the whole cardiac cycle. The large sarcomere lengths near the ring at the base of the ellipsoid can be attributed to the zero displacement boundary conditions prescribed. There is relatively little torsion during this phase, which may also be due to the boundary conditions applied.

During isovolumetric contraction (plots D and E) the rapid increase in active tension causes the ellipsoid to rapidly contract, while the cavity volume remains constant. The increase in active tension causes the heart to twist and the sarcomere lengths to shorten. This phase shows the torsion that occurs during the cardiac cycle due to the active tension acting in the fibre direction, which has a circumferential component. This torsion has been shown in a number of experimental studies [14, 136].

During ejection (plots F and G) the cavity volume is no longer constant and the cavity size decreases. The increase in active tension causes further torsion. The increased torsion in turn increases the displacement, however, as there is no volume constraint, the epicardium is free to move inwards significantly and reduce the radial displacement.

In the isovolumetric relaxation phase (plots H and I) the active tension decreases, causing the ventricle to relax towards its original state - the state it was in at the beginning of diastole. The sarcomere length gradually increases as the active tension decreases, while the heart relaxes and untwists. One would expect the sarcomere lengths at the end of isovolumetric relaxation to be the same as at the beginning of the simulation, however this is not the case. The reason for this is that there is still some residual active tension at the end of isovolumetric relaxation.

Fig. 6.15 shows the sarcomere length and active tension near the base, the middle and the apex of the ventricle. For each height the results are for endocardium and the epicardium at these heights.

During diastolic filling, from $t = 0\,s$ to $t = 1\,s$, the sarcomere lengths increase due to the pressure on the endocardial wall increasing the cavity size. Near the middle of the ventricle the sarcomere lengths at each transmural position increase at the same rate, while at the apex and base the sarcomere lengths at

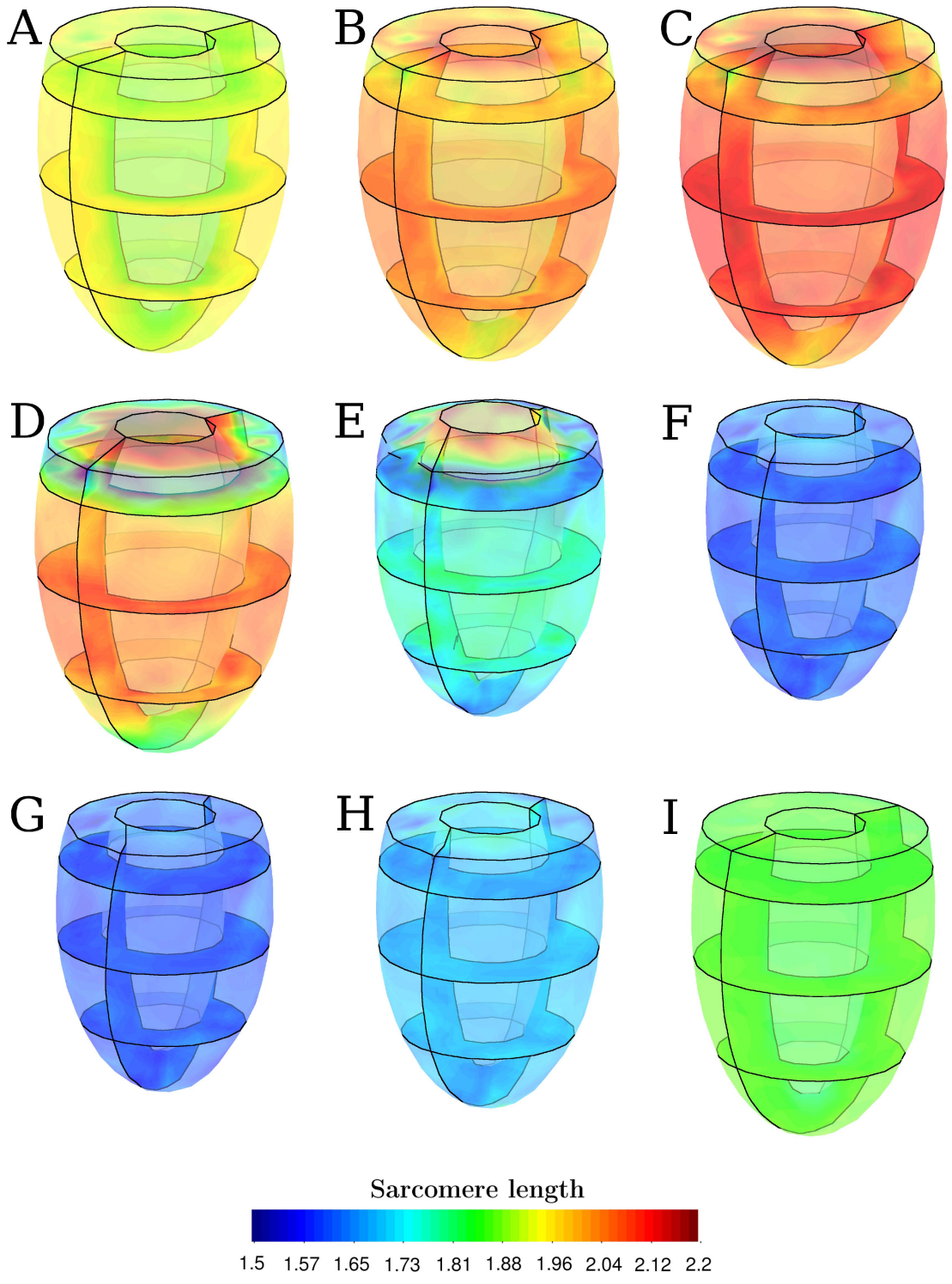

Figure 6.14: Sarcomere length distribution and deformation of the healthy rat left ventricle for representative time points A-I of the cardiac cycle. All plots share the same scale and orientation. Sarcomere length is measured in μm.

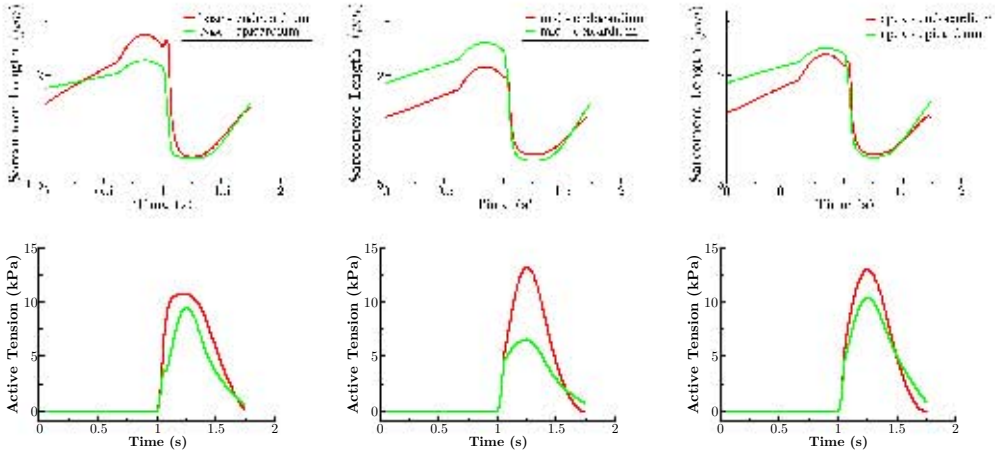

Figure 6.15: Sarcomere length and active tension plots for Left: particles near the base of the left ventricle, Centre: particles near the middle of the left ventricle and Right: particles near the apex of the left ventricle.

the endocardial position increase faster than at epicardial positions. The active tension during this phase is zero, as active tension is only introduced at the beginning of the next phase, isovolumetric contraction.

The sarcomere lengths drop rapidly during isovolumetric contraction due to the increase in active tension. This increase in active tension results in a compressive force that reduces sarcomere length. During this phase the active tension increases uniformly at all locations in the heart since the sarcomere lengths are not yet small enough for the length dependence of the active tension to be a major factor.

As ejection begins, the sarcomere lengths throughout the heart are similar. The sarcomeres at the epicardium shorten faster than at the endocardium, causing a lower active tension at the epicardium than at the endocardium. This demonstrates the dependence of active tension on sarcomere length. Consider the time at which active tension is maximum $t = 1.25s$. This is especially evident in the middle of the ventricle where a difference in sarcomere lengths of only $\sim 0.05\mu m$ between the endocardium and epicardium leads to a two fold increase in active tension.

The sharp notch present in the epicardial positions at the beginning of ejection can be attributed to the change in boundary conditions that occurs. The boundary conditions change from an increasing pressure that maintains the cav-

ity volume to a constant pressure with a cavity volume that is not constrained. As seen in Fig. 6.14, the sarcomere length quickly decreases during ejection, and the length dependence of the active tension causes a sharp reduction in the active tension amplitude.

During isovolumetric relaxation the active tension gradually decreases and the sarcomere lengths increase due to the decrease in compressive forces. The sarcomere lengths are similar throughout the heart. This causes the relaxation time of the active tension to be uniform throughout the heart, since the relaxation time is a function of sarcomere length (see eq. (4.20)).

6.2.3 Infarcted Model

The cardiac cycle for the rat left ventricle during the ischaemic phase of myocardial infarction was simulated. A truncated ellipsoid model of the rat left ventricle with a small posterior infarct was used as the geometry. This is shown in Fig. 6.16. The volume of the infarct was $99.77\mu L$ while the total wall volume was $641.70\mu L$. The volume fraction of the infarct is thus 15.5% of the wall volume.

To model the passive material properties of the myocardium during ischaemia the stiffness constant of the passive mechanical model in the infarcted region was decreased by half, to $A = 0.44\,kPa$. In the infarcted region there is no contractile force so the maximum active tension parameter was set to zero, $T_{max} = 0\,kPa$ (see Fig. 6.16). The cardiac cycle was controlled in the same way as for the healthy model, with the same boundary conditions.

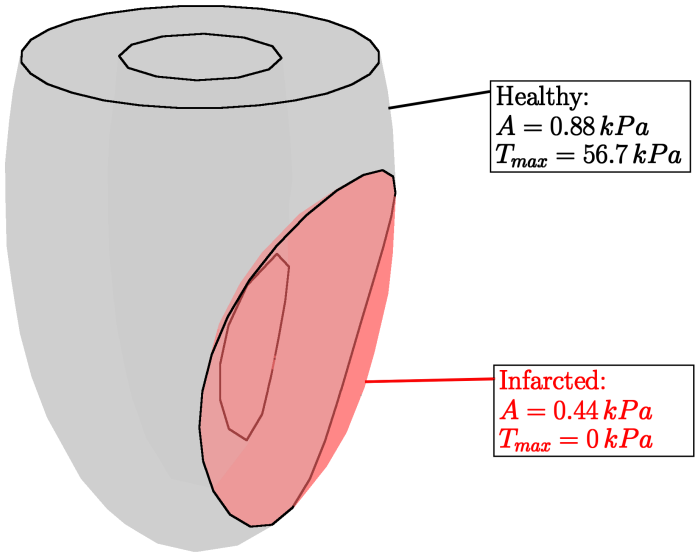

Figure 6.16: Ellipsoid geometry of infarcted left ventricle.

The end diastolic volume was found to be $356.19\mu L$, while the end systolic volume was $201.17\mu L$. This increase in end diastolic volume during ischaemia, as compared to $348.02\mu L$ for the healthy left ventricle, is expected since part of the myocardium is less stiff and undergoes greater deformation. Experimentally it has been found that with ischaemia there is a increase in end diastolic volume as

compared to the healthy end diastolic volume [19]. The increase in end systolic volume is also expected as a significant part of the heart is not contracting and therefore not attempting to reduce the cavity volume.

The ejection fraction was calculated as 43.52%, corresponding to a decrease in cardiac function. The stroke volume also decreased as compared with the healthy model to $155.02\mu L$. This decrease in stroke volume is critical as it means that 11.51% less blood is pumped to the body during a cardiac cycle.

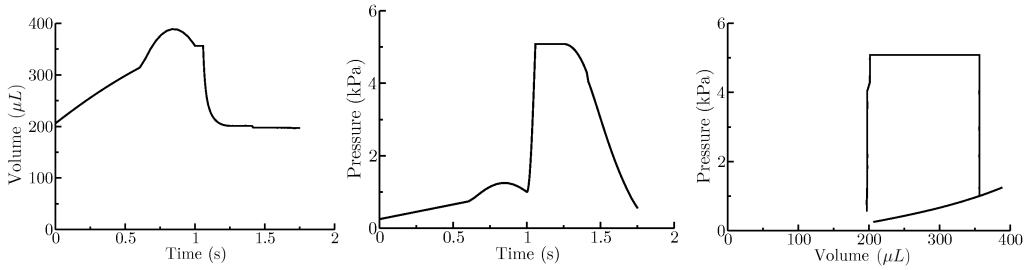

Figure 6.17: Basic metrics of cardiac function over the cardiac cycle of the infarcted left ventricle.

Fig. 6.17 shows the pressure, volume and time relationships of the infarcted left ventricle. They show qualitatively the same features of the healthy left ventricle because the cardiac cycle is still functional. Key differences, apart from the end diastolic and end systolic volumes, are noticeable when investigating the timing of the different phases of the cardiac cycle.

The period of diastolic filling was the same as with the healthy model since this was prescribed to begin at $0s$ and end at $1s$. Isovolumetric contraction on the other hand finishes at $1.055s$. This is $0.005s$ later than in the healthy model and can be attributed to the lack of contractile power in the infarct. This causes an overall reduction in contraction. Ejection occurs at the same time point as in the healthy model: again because the time of maximum active tension is prescribed to occur at $1.25s$. The isovolumetric relaxation phase however has a longer period in the infarcted model than in the healthy model. The timings of the different phases of the cardiac cycle are summarised in Table 6.3.

In Fig. 6.18 the sarcomere length distribution and deformation is plotted at representative time points A-I during the cardiac cycle. Note that the scaling of sarcomere length in this figure differs to that in the healthy model. This is to accommodate the increased sarcomere lengths that occur during the cardiac

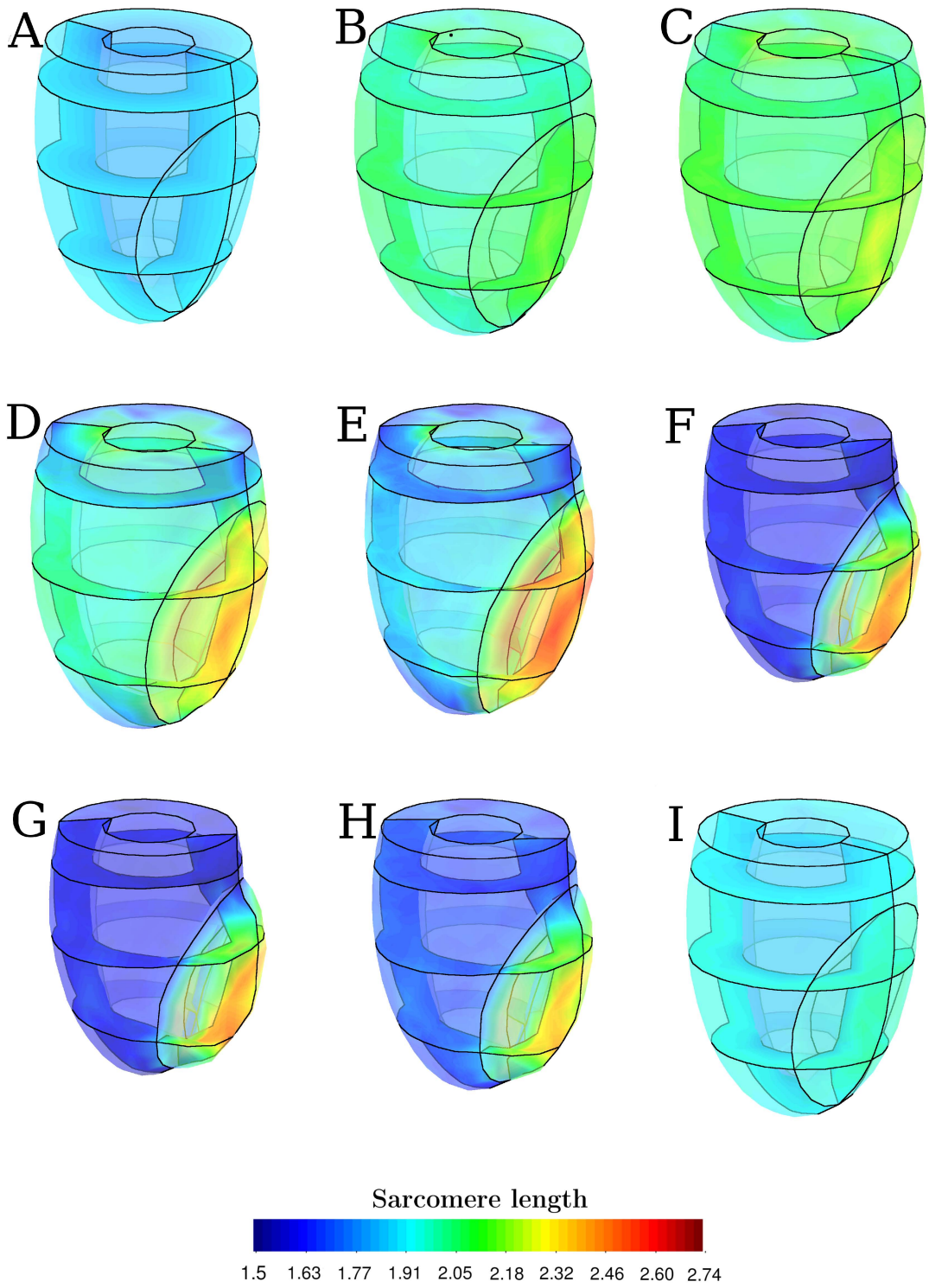

Figure 6.18: Sarcomere length distribution and deformation of the infarcted rat left ventricle for representative time points A-I of the cardiac cycle. All plots share the same scale and orientation. Sarcomere length is measured in μm.

	A	B	C	D	E	F	G	H	I
t (s)	0	0.5	1.0	1.030	1.055	1.160	1.250	1.600	1.855

Table 6.3: Representative time point values for the cardiac cycle of the infarcted left ventricle.

cycle of the infarcted model.

During diastole (plots A to C) the addition of the infarct does not greatly affect the sarcomere length. What can be observed is a slight increase in sarcomere length in the infarct. This is to be expected since the less stiff infarct should stretch more than the healthy myocardium under the same pressure force.

The effect of the infarct becomes important during isovolumetric contraction phase (plots D and E). The non-contractile nature of the infarcted region can clearly be seen, as instead of decreasing, the sarcomere length increases. In the infarcted region the sarcomere lengths increase up to $2.7\mu m$. Overstretching of sarcomeres in ischaemic tissue of the infarcted heart has been found experimentally by Crozatier *et al.* [20].

During ejection (plots F and G) the non-contractile nature of the infarct causes the the infarcted region to bulge out. The healthy myocardium contracts to decrease the cavity size, while the infarcted region is passive. During isovolumetric relaxation (plots H and I)the sarcomere length in the healthy region increases, while the sarcomere length in the infarcted region decreases from its overstretched state.

Chapter 7

Conclusion

7.1 Conclusion

A mathematical model of the rat left ventricle was developed to study myocardial infarction. The model describes the electrophysiological and mechanical function of the heart, together with boundary conditions that simulate the cardiac cycle. The geometry of the rat left ventricle was approximated using a truncated ellipsoid with dimensions consistent with experimental data. The accuracy of the healthy model was assessed through validation by experimental data. The first stage of myocardial infarction, ischaemia, was modelled with results comparing favourably to experimental results.

The eikonal diffusion equation was solved for a number of particle distributions with increasing particle number to analyse the error in the numerical solution. The error reduced for finer particle distributions, as was expected. To show the accuracy of numerical solutions to the eikonal diffusion equation, simulations presented by Colli-Franzone *et al.* [135] and Tomlinson [98] were reproduced.

The electrophysiology model was then calibrated so that physiologically accurate depolarisation times could be calculated for the rat left ventricle. This was achieved by comparing numerical results with the experimental results of Durrer *et al.* [9]. Five initial depolarisation points were identified from the experimental depolarisation time map. The five points were used as boundary conditions for the eikonal diffusion equation. It was found that isovolumetric relaxationa propagation speed of $c_0 = 1.344 mm\, ms^{-1}$ was required on a thin strip near the endocardium to simulate the Purkinje network while $c_0 = 0.88 mm\, ms^{-1}$ simu-

lated the propagation speed in the rest of the myocardium. The full depolarisation time map was produced and compared to that of Durrer *et al.*.

The passive mechanics of the heart was described by the transversely isotropic, nearly incompressible constitutive law of Usyk *et al.* [5]. This constitutive law was able to reproduce, qualitatively and quantitatively, the characteristic nonlinear pressure-volume curve for diastolic filling. The simulation results were well within the experimental results of Cingolani *et al.*, Usyk *et al.* and Herrmann *et al.* [5, 11, 12].

The full cardiac cycle of a healthy rat left ventricle was simulated. Basic metrics of cardiac function such as end diastolic cavity volume and end systolic cavity volume compared well with experimental data of Faber *et al.* [15]. During contraction the ellipsoid produces the characteristic torsion that has been found experimentally [136]. The contraction of the heart was modelled using the Guccione active stress model, where an active stress is added to the aforementioned passive stress [68]. The active tension showed typical dependence on sarcomere length.

Finally the rat left ventricle was modelled with a small posterior ischaemic myocardial infarct. The end diastolic volume was calculated and found to be larger than in the case of the healthy heart. This is consistent with experimental findings of increased end diastolic volume of the ischaemic left ventricle. In addition, significant stretching of the sarcomeres within the infarcted region during contraction, as found experimentally, was observed [19].

This model can be used to study the mechanical effects of myocardial infarction in more detail and can be developed further to study the effects of treatments of myocardial infarction. Results from these computational simulations can be used to inform the developments of these treatments and can even be used in a clinical setting.

7.2 Further Work

The model that has been developed considers the electrophysiology as well as the mechanics of the heart. But the precise haemodynamics in the heart also play an important role in regulating the pressure during ejection. Rather than assuming constant pressure during ejection, an appropriate model would be the

Windkessel model which models the blood pressure within the aorta. This could be coupled to the pressure boundary condition during ejection. Implementing this model would improve the active tension development during ejection as the compression near the endocardium would be reduced.

Another aspect that has not been studied is that of electromechanical coupling. This could be achieved by using the depolarisation times found using the eikonal diffusion equation as an input into the active stress model. This would more accurately model the contraction of the left ventricle which is not completely synchronous.

More realistic geometries based on MRI images should be implemented to study different types of infarct geometries in more detail. One would then have to be take consideration of the fibre directions within the geometry, as they are spatially dependent. More realistic geometries require finer particle distributions as there are more irregularities in the structure. This would increase the computational time required to solve the equations.

Bibliography

[1] K. Steyn, K. Sliwa, S. Hawken, P. Commerford, C. Onen, A. Damasceno, S. Ounpuu, and S. Yusuf. Risk factors associated with myocardial infarction in africa: The interheart africa study. *Circulation*, 112(23):3554–3561, December 6, 2005.

[2] M. Gheorghiade and R. O. Bonow. Chronic heart failure in the united states: a manifestation of coronary artery disease. *Circulation*, 97(3):282–289, 1998.

[3] D. Lloyd-Jones, R. J. Adams, T. M. Brown, M. Carnethon, S. Dai, G. De Simone, T. B. Ferguson, E. Ford, K. Furie, C. Gillespie, et al. Heart disease and stroke statistics-2010 update. *Circulation*, 121(7):e46–e215, 2010.

[4] J. P. Keener. An eikonal-curvature equation for action potential propagation in myocardium. *Journal of mathematical biology*, 29(7):629–651, 1991.

[5] T.P. Usyk, R. Mazhari, and A.D. McCulloch. Effect of laminar orthotropic myofiber architecture on regional stress and strain in the canine left ventricle. *Journal of Elasticity*, 61:143–164, 2000. 10.1023/A:1010883920374.

[6] J. M. Guccione and A. D. McCulloch. Mechanics of active contraction in cardiac muscle: Part i–constitutive relations for fiber stress that describe deactivation. *J Biomech Eng*, 115(1):72–81, Feb 1993.

[7] T. Belytschko, Y. Y. Lu, and L. Gu. Element-free galerkin methods. *International Journal for Numerical Methods in Engineering*, 37:229–256, 1994.

[8] G. J. Wagner and W. K. Liu. Application of essential boundary conditions in mesh-free methods: a corrected collocation method. *International Journal for Numerical Methods in Engineering*, 47(8):1367–1379, 2000.

[9] D. Durrer, D. Van, et al. Total excitation of the isolated human heart. *Circulation*, 41(6):899, 1970.

[10] W. Müller, H. Windisch, and HA Tritthart. Fast optical monitoring of microscopic excitation patterns in cardiac muscle. *Biophysical journal*, 56(3):623–629, 1989.

[11] K.L. Herrmann, A.D. McCulloch, and J.H. Omens. Glycated collagen cross-linking alters cardiac mechanics in volume-overload hypertrophy. *American Journal of Physiology-Heart and Circulatory Physiology*, 284(4):H1277–H1284, 2003.

[12] O.H. Cingolani, X.P. Yang, M.A. Cavasin, and O.A. Carretero. Increased systolic performance with diastolic dysfunction in adult spontaneously hypertensive rats. *Hypertension*, 41(2):249–254, 2003.

[13] J. H. Omens, D. A. MacKenna, and A. D. McCulloch. Measurement of strain and analysis of stress in resting rat left ventricular myocardium. *Journal of Biomechanics*, 26:665–676, 1993.

[14] R. G. Wise, C. L. H. Huang, G. A. Gresham, A. I. M. Al-Shafei, T. A. Carpenter, and L. D. Hall. Magnetic resonance imaging analysis of left ventricular function in normal and spontaneously hypertensive rats. *The Journal of physiology*, 513(3):873–887, 1998.

[15] M.J. Faber, M. Dalinghaus, I.M. Lankhuizen, P. Steendijk, W.C. Hop, R.G. Schoemaker, D.J. Duncker, J.M.J. Lamers, and W.A. Helbing. Right and left ventricular function after chronic pulmonary artery banding in rats assessed with biventricular pressure-volume loops. *American Journal of Physiology-Heart and Circulatory Physiology*, 291(4):H1580–H1586, 2006.

[16] D. Jegger, A.S. Mallik, M. Nasratullah, X. Jeanrenaud, R. da Silva, H. Tevaearai, L.K. von Segesser, and N. Stergiopulos. The effect of a myocardial infarction on the normalized time-varying elastance curve. *Journal of Applied Physiology*, 102(3):1123–1129, 2007.

[17] K.A. Connelly, D.L. Prior, D.J. Kelly, M.P. Feneley, H. Krum, and R.E. Gilbert. Load-sensitive measures may overestimate global systolic function in the presence of left ventricular hypertrophy: a comparison with

load-insensitive measures. *American Journal of Physiology-Heart and Circulatory Physiology*, 290(4):H1699–H1705, 2006.

[18] K. Uemura, T. Kawada, M. Sugimachi, C. Zheng, K. Kashihara, T. Sato, and K. Sunagawa. A self-calibrating telemetry system for measurement of ventricular pressure-volume relations in conscious, freely moving rats. *American Journal of Physiology-Heart and Circulatory Physiology*, 287(6):H2906–H2913, 2004.

[19] J.L. McCans and J.O. Parker. Left ventricular pressure-volume relationships during myocardial ischemia in man. *Circulation*, 48(4):775–785, 1973.

[20] B. Crozatier, M. Ashraf, D. Franklin, J. Ross, L. Nimmo, and D. Mckown. Sarcomere length in experimental myocardial infarction: Evidence for sarcomere overstretch in dyskinetic ventricular regions. *Journal of Molecular and Cellular Cardiology*, 9(10):785–797, 1977.

[21] O. Akinboboye, O. Idris, and O. Akinkugbe. Trends in coronary artery disease and associated risk factors in sub-saharan africans. *Journal of human hypertension*, 17(6):381–387, 2003.

[22] http://www.health-reply.com/risk-factors-myocardial infarction/. Health reply.

[23] S. A. Niederer, M. Fink, D. Noble, and N. P. Smith. A meta-analysis of cardiac electrophysiology computational models. *Experimental physiology*, 94(5):486–495, 2009.

[24] S. T. Wall, J. C. Walker, K. E. Healy, M. B. Ratcliffe, and J. M. Guccione. Theoretical impact of the injection of material into the myocardium. *Circulation*, 114:2627–2635, 2006.

[25] J. F. Wenk, S. T. Wall, R. C. Peterson, S. L. Helgerson, H. N. Sabbah, M. Burger, N. Stander, M. B. Ratcliffe, and J. M. Guccione. A method for automatically optimizing medical devices for treating heart failure: designing polymeric injection patterns. *Journal of biomechanical engineering*, 131:121011, 2009.

[26] J. J. Pilla, A. S. Blom, J. H. Gorman, D. J. Brockman, J. Affuso, L. M. Parish, H. Sakamoto, B. M. Jackson, M. A. Acker, and R. C. Gorman. Early postinfarction ventricular restraint improves borderzone wall thickening dynamics during remodeling. *Ann Thorac Surg*, 80(6):2257–2262, December 1, 2005.

[27] M. Sermesant, R. Chabiniok, P. Chinchapatnam, T. Mansi, F. Billet, P. Moireau, JM Peyrat, K. Wong, J. Relan, K. Rhode, et al. Patient-specific electromechanical models of the heart for the prediction of pacing acute effects in crt: A preliminary clinical validation. *Medical image analysis*, 2011.

[28] N. Smith, A. de Vecchi, M. McCormick, D. Nordsletten, O. Camara, A.F. Frangi, H. Delingette, M. Sermesant, J. Relan, N. Ayache, et al. euheart: personalized and integrated cardiac care using patient-specific cardiovascular modelling. *Interface Focus*, 1(3):349, 2011.

[29] R. C. P. Kerckhoffs, S. M. Narayan, J. H. Omens, L. J. Mulligan, and A. D. McCulloch. Computational modeling for bedside application. *Heart failure clinics*, 4(3):371–378, 2008.

[30] D. Noble. Modelling the heart: insights, failures and progress. *Bioessays*, 24:1155–1163, 2002.

[31] D. Noble. A modification of the hodgkin-huxley equations applicable to purkinje fibre action and pacemaker potentials. *The Journal of Physiology*, 160(2):317, 1962.

[32] R. C. P. Kerckhoffs. *Patient-Specific Modeling of the Cardiovascular System: Technology-Driven Personalized Medicine*. Springer Verlag, 2010.

[33] F. B. Sachse. *Computational Cardiology*. Springer, 2004.

[34] J. J. Rice and P. Kohl. *Electrical Diseases of the Heart: Genetics, Mechanisms, Treatment, Prevention*, chapter Mechanoelectrical Interactions and Their Role in Electrical Function of the Heart, pages 145–160. Springer, 2008.

[35] A. L. Hodgkin and A. F. Huxley. A quantitative description of membrane current and its application to conduction and excitation in nerve. *The Journal of physiology*, 117(4):500, 1952.

[36] G. W. Beeler and H. Reuter. Reconstruction of the action potential of ventricular myocardial fibres. *The Journal of physiology*, 268(1):177, 1977.

[37] C. Luo and Y. Rudy. A model of the ventricular cardiac action potential. depolarization, repolarization, and their interaction. *Circulation Research*, 68(6):1501, 1991.

[38] C. H. Luo and Y. Rudy. A dynamic model of the cardiac ventricular action potential. ii. afterdepolarizations, triggered activity, and potentiation. *Circulation research*, 74(6):1097, 1994.

[39] C. H. Luo and Y. Rudy. A dynamic model of the cardiac ventricular action potential. i. simulations of ionic currents and concentration changes. *Circulation Research*, 74(6):1071–1096, 1994.

[40] L. S. Gettes and H. Reuter. Slow recovery from inactivation of inward currents in mammalian myocardial fibres. *The Journal of physiology*, 240(3):703–724, 1974.

[41] J. F Spear and E. N. Moore. The effect of changes in rate and rhythm on supernormal excitability in the isolated purkinje system of the dog. *Circulation*, 50(6):1144–1149, 1974.

[42] D. R. Chialvo, D. C. Michaels, and J. Jalife. Supernormal excitability as a mechanism of chaotic dynamics of activation in cardiac purkinje fibers. *Circulation research*, 66(2):525–545, 1990.

[43] K. Ten Tusscher and A. V. Panfilov. Reentry in heterogeneous cardiac tissue described by the luo-rudy ventricular action potential model. *American Journal of Physiology-Heart and Circulatory Physiology*, 284(2):H542–H548, 2003.

[44] J. A. Trangenstein and C. Kim. Operator splitting and adaptive mesh refinement for the luo–rudy i model. *Journal of Computational Physics*, 196(2):645–679, 2004.

[45] D. Noble, A. Varghese, P. Kohl, and P. Noble. Improved guinea-pig ventricular cell model incorporating a diadic space, ikr and iks, and length- and tension-dependent processes. *The Canadian journal of cardiology*, 14(1):123, 1998.

[46] V. E. Bondarenko, G. P. Szigeti, G. C. L. Bett, S. J. Kim, and R. L. Rasmusson. Computer model of action potential of mouse ventricular myocytes. *American Journal of Physiology-Heart and Circulatory Physiology*, 287(3):H1378–H1403, 2004.

[47] S. V. Pandit, R. B. Clark, W. R. Giles, and S. S. Demir. A mathematical model of action potential heterogeneity in adult rat left ventricular myocytes. *Biophys J*, 81(6):3029–51, Dec 2001.

[48] P. B. Gharpure and C. R. Johnson. A cellular automaton model of electrical activation in canine ventricles: A validation study. *Annals of Biomed. Eng*, 1995.

[49] D. Wei, O. Okazaki, K. Harumi, E. Harasawa, and H. Hosaka. Comparative simulation of excitation and body surface electrocardiogram with isotropic and anisotropic computer heart models. *Biomedical Engineering, IEEE Transactions on*, 42(4):343–357, 1995.

[50] W. T. Miller and D. B. Geselowitz. Simulation studies of the electrocardiogram. i. the normal heart. *Circulation Research*, 43(2):301–315, 1978.

[51] L. Tung. *A bi-domain model for describing ischemic myocardial DC currents*. PhD thesis, PhD thesis, MIT, Cambridge, MA, 1978.

[52] R. Fitzhugh. Impulses and physiological states in theoretical models of nerve membrane. *Biophysical Journal*, 1(6):445–466, 1961.

[53] P. Colli Franzone and L. Guerri. Spreading of excitation in 3-d models of the anisotropic cardiac tissue. i. validation of the eikonal model. *Mathematical Biosciences*, 113(2):145 – 209, 1993.

[54] D. Nickerson, S. Niederer, C. Stevens, M. Nash, and P. Hunter. A computational model of cardiac electromechanics. In *Engineering in Medicine and*

Biology Society, 2006. EMBS '06. 28th Annual International Conference of the IEEE, pages 5311 –5314, 302006-sept.3 2006.

[55] H. Demiray. A note on the elasticity of soft biological tissues. *Journal of Biomechanics*, 5(3):309–311, 1972.

[56] R. F. Janz and A. F. Grimm. Deformation of the diastolic left ventricle:: I. nonlinear elastic effects. *Biophysical Journal*, 13(7):689–704, 1973.

[57] Y. C. Fung. Elasticity of soft tissues in simple elongation. *American Journal of Physiology - Legacy Content*, 213(6):1532–1544, 1967.

[58] J. M. Guccione, A. D. McCulloch, and L. K. Waldman. Passive material properties of intact ventricular myocardium determined from a cylindrical model. *Journal of Biomechanical Engineering*, 113:42, 1991.

[59] P. H. M. Bovendeerd, T. Arts, J. M. Huyghe, D. H. Van Campen, and R. S. Reneman. Dependence of local left ventricular wall mechanics on myocardial fiber orientation: a model study. *Journal of biomechanics*, 25(10):1129–1140, 1992.

[60] R. J. Okamoto, M. J. Moulton, S. J. Peterson, D. Li, M. K. Pasque, and J. M. Guccione. Epicardial suction: a new approach to mechanical testing of the passive ventricular wall. *Journal of biomechanical engineering*, 122:479, 2000.

[61] R. C. P. Kerckhoffs, P. H. M. Bovendeerd, J. C. S. Kotte, F. W. Prinzen, K. Smits, and T. Arts. Homogeneity of cardiac contraction despite physiological asynchrony of depolarization: A model study. *Annals of Biomedical Engineering*, 31:536–547, 2003. 10.1114/1.1566447.

[62] J.J. Rice, R.L. Winslow, and W.C. Hunter. Comparison of putative cooperative mechanisms in cardiac muscle: length dependence and dynamic responses. *American Journal of Physiology-Heart and Circulatory Physiology*, 276(5):H1734, 1999.

[63] P.J. Hunter, A.D. McCulloch, and H.E.D.J. ter Keurs. Modelling the mechanical properties of cardiac muscle. *Progress in Biophysics and Molecular Biology*, 69(2-3):289 – 331, 1998.

[64] V. Novak and J. Neumann. Mathematical model of the electromechanical heart contractile system - simulation results. *International Journal of Bioelectromagnetism*, 2, 2000.

[65] K. Glänzel, FB Sachse, G. Seemann, C. Riedel, and O. Dössel. Modeling force development in the sarcomere in consideration of electromechanical coupling. *Biomedizinische Technik/Biomedical Engineering*, 47(s1b):774–777, 2002.

[66] J.L. Greenstein, R. Hinch, and R.L. Winslow. Mechanisms of excitation-contraction coupling in an integrative model of the cardiac ventricular myocyte. *Biophysical journal*, 90(1):77–91, 2006.

[67] G. Seemann. *Modelling of Electrophysiology and Tension Development in the Human Heart*. PhD thesis, University of Karlsruhe, 2005.

[68] J. M. Guccione, L. K. Waldman, and A. D. McCulloch. Mechanics of active contraction in cardiac muscle: Part ii-cylindrical models of the systolic left ventricle. *ASME Journal of Biomechanical Engineering*, 115:82–90, 1993.

[69] P. Nardinocchi and L. Teresi. On the active response of soft living tissues. *Journal of Elasticity*, 88:27–39, 2007.

[70] F. Nobile, A. Quarteroni, and R. Ruiz-Baier. An active strain electromechanical model for cardiac tissue. *International Journal for Numerical Methods in Biomedical Engineering*, 28:52–71, 2012.

[71] D. F. Scollan, A. Holmes, R. Winslow, and J. Forder. Histological validation of myocardial microstructure obtained from diffusion tensor magnetic resonance imaging. *Am J Physiol*, 275(6 Pt 2):H2308–18, Dec 1998.

[72] D. F. Scollan, A. Holmes, J. Zhang, and R. L. Winslow. Reconstruction of cardiac ventricular geometry and fiber orientation using magnetic resonance imaging. *Annals of Biomedical Engineering*, 28:934–944, 2000.

[73] R. Kerckhoffs. *Depolarization wave and mechanics in the paced heart: model and experiment*. PhD thesis, Tehcnical University of Eindhoven, 2003.

[74] N. P. Smith, M. L. Buist, and A. J. Pullan. Altered t wave dynamics in a contracting cardiac model. *Journal of Cardiovascular Electrophysiology*, 14:S203–S209, 2003.

[75] M. P. Nash and A. V. Panfilov. Electromechanical model of excitable tissue to study reentrant cardiac arrhythmias. *Progress in Biophysics & Molecular Biology*, 85:501–522, 2004.

[76] E.J. Vigmond, R. Ruckdeschel, and N. Trayanova. Reentry in a morphologically realistic atrial model. *Journal of cardiovascular electrophysiology*, 12(9):1046–1054, 2001.

[77] H. J. Arevalo, P. A. Helm, and N. A. Trayanova. Development of a model of the infarcted canine heart that predicts arrhythmia generation from specific cardiac geometry and scar distribution. In *Computers in Cardiology, 2008*, pages 497–500. IEEE, 2008.

[78] J.C. Walker, M.B. Ratcliffe, P. Zhang, A.W. Wallace, B. Fata, E.W. Hsu, D. Saloner, and J.M. Guccione. Mri-based finite-element analysis of left ventricular aneurysm. *American Journal of Physiology-Heart and Circulatory Physiology*, 289(2):H692, 2005.

[79] R. Chabiniok, D. Chapelle, P. Lesault, A. Rahmouni, and J. Deux. Validation of a biomechanical heart model using animal data with acute myocardial infarction. In *CI2BM09 - MICCAI Workshop on Cardiovascular Interventional Imaging and Biophysical Modelling*, 2009.

[80] D. M. Nelson, Z. Ma, K. L. Fujimoto, R. Hashizume, and W. R. Wagner. Intra-myocardial biomaterial injection therapy in the treatment of heart failure: Materials, outcomes and challenges. *Acta Biomaterialia*, 7:1–15, 2011.

[81] T. P. Usyk and A. D. McCulloch. Electromechanical model of cardiac resynchronization in the dilated failing heart with left bundle branch block. *Journal of Electrocardiology*, 36:57–61, 2003.

[82] P. Wriggers. *Nonlinear finite element methods*. Springer Verlag, 2008.

[83] J. Bonet and R. D. Wood. *Nonlinear Continuum Mechanics for Finite Element Analysis*. Cambridge University Press, 2008.

[84] Y. Rudy and J.R. Silva. Computational biology in the study of cardiac ion channels and cell electrophysiology. *Quarterly reviews of biophysics*, 39(01):57–116, 2006.

[85] R.K. Hobbie and P.B. Kahn. Intermediate physics for medicine and biology. *American Journal of Physics*, 67:457, 1999.

[86] R.A. Luke and J.E. Saffitz. Remodeling of ventricular conduction pathways in healed canine infarct border zones. *Journal of Clinical Investigation*, 87(5):1594, 1991.

[87] A. D. McCulloch, B. H. Smaill, and P. J. Hunter. Regional left ventricular deformation in the passive dog heart. *Circulation Research*, 64:721–733, 1989.

[88] G. A. Holzapfel and R. W. Ogden. Constitutive modelling of passive myocardium: a structurally based framework for material characterization. *Philosophical Transactions of the Royal Society a-Mathematical Physical and Engineering Sciences*, 367(1902):3445–3475, Sep 13 2009.

[89] http://www.arthursclipart.org/. Arthur's clip art.

[90] D. Durrer, JP Roos, and J. Biiller. The spread of excitation in canine and human heart. In *International Symposium on the Electrophysiology of the Heart*, page 203. Symposium Publications Division, Pergamon Press, 1965.

[91] A.M. Scher, A.C. Young, A.L. Malmgren, and R.V. Erickson. Activation of the interventricular septum. *Circulation Research*, 3(1):56, 1955.

[92] A.M. Scher, A.C. Young, A.L. Malmghen, and R.R. Paton. Spread of electrical activity through the wall of the ventricle. *Circulation Research*, 1(6):539, 1953.

[93] J.T. Mortimer, R. Magnusson, and I. Petersen. Conduction velocity in ischemic muscle: effect on emg frequency spectrum. *American Journal of Physiology–Legacy Content*, 219(5):1324–1329, 1970.

[94] J. M. De Bakker, F. J. Van Capelle, M. J. Janse, S. Tasseron, J. T. Vermeulen, N. De Jonge, and J. R. Lahpor. Slow conduction in the infarcted human heart.'zigzag'course of activation. *Circulation*, 88(3):915–926, 1993.

[95] D. B. Geselowitz and 3rd Miller W. T. A bidomain model for anisotropic cardiac muscle. *Ann Biomed Eng*, 11(3-4):191–206, 1983.

[96] L. S. Green, B. Taccardi, P. R. Ershler, and R. L. Lux. Epicardial potential mapping. effects of conducting media on isopotential and isochrone distributions. *Circulation*, 84(6):2513–2521, 1991.

[97] A. Kamkin, I. Kiseleva, and G. Isenberg. Stretch-activated currents in ventricular myocytes: amplitude and arrhythmogenic effects increase with hypertrophy. *Cardiovascular research*, 48(3):409–420, 2000.

[98] K. A. Tomlinson. *Finite Element Solution of an Eikonal Equation for Excitation Wavefront Propagation in Ventricular Myocardium*. PhD thesis, University of Auckland, 2000.

[99] E.L. Allgower and K. Georg. Numerical continuation methods. *Springer Ser. Comput. Math*, 15, 1990.

[100] J.A. Sethian and A. Vladimirsky. Ordered upwind methods for static hamilton–jacobi equations. *Proceedings of the National Academy of Sciences*, 98(20):11069, 2001.

[101] R. C. Kerckhoffs, O. P. Faris, P. H. Bovendeerd, F. W. Prinzen, K. Smits, E. R. McVeigh, and T. Arts. Timing of depolarization and contraction in the paced canine left ventricle: model and experiment. *J Cardiovasc Electrophysiol*, 14(10 Suppl):S188–95, Oct 2003.

[102] J. Suzuki, H. Tsubone, and S. Sugano. Studies on the positive t wave on ecg in the rat-based on the analysis for direct cardiac electrograms in the ventricle. *Advances in Animal Cardiology*, 26(1):24–32, 1993.

[103] http://www.permanente.net/. Permanente.

[104] F. B. Sachse, G. Seemann, and M. B. Mohr. Electro-mechanics in biventricular models. In *Computers in Cardiology, 2004*, pages 537–540. IEEE, 2004.

[105] J. W. Holmes, T. K. Borg, and J. W. Covell. Structure and mechanics of healing myocardial infarcts. *Annual Review of Biomedical Engineering*, 7:223–253, 2005.

[106] G.M. Fomovsky and J.W. Holmes. Evolution of scar structure, mechanics, and ventricular function after myocardial infarction in the rat. *American Journal of Physiology- Heart and Circulatory Physiology*, 298(1):H221, 2010.

[107] J. S. Forrester, G. Diamond, W. W. Parmley, and H. J. Swan. Early increase in left ventricular compliance after myocardial infarction. *J Clin Invest*, 51(3):598–603, Mar 1972.

[108] W. Grossman, D. Jones, and L. P. McLaurin. Wall stress and patterns of hypertrophy in human left-ventricle. *Journal of Clinical Investigation*, 56:56–64, 1975.

[109] W. Grossman. Cardiac hypertrophy: useful adaptation or pathologic process? *The American journal of medicine*, 69(4):576–584, 1980.

[110] J. H. Omens and Y. C. Fung. Residual strain in rat left ventricle. *Circulation Research*, 66:37–45, 1990.

[111] E.K. Rodriguez, A. Hoger, and A.D. McCulloch. Stress-dependent finite growth in soft elastic tissues. *Journal of biomechanics*, 27(4):455–467, 1994.

[112] A. Rachev. Theoretical study of the effect of stress-dependent remodeling on arterial geometry under hypertensive conditions. *Journal of biomechanics*, 30(8):819–827, 1997.

[113] S. R. Summerour, J. L. Emery, B. Fazeli, J. H. Omens, and A. D. McCulloch. Residual strain in ischemic ventricular myocardium. *J Biomech Eng*, 120(6):710–4, Dec 1998.

[114] E.K. Rodriguez, J.H. Omens, LK Waldman, and AD McCulloch. Effect of residual stress on transmural sarcomere length distributions in rat left ventricle. *American Journal of Physiology-Heart and Circulatory Physiology*, 264(4):H1048, 1993.

[115] L.A. Taber, M. Yang, and W.W. Podszus. Mechanics of ventricular torsion. *Journal of biomechanics*, 29(6):745–752, 1996.

[116] T. P. Usyk, I. J. LeGrice, and A. D. McCulloch. Computational model of three-dimensional cardiac electromechanics. *Computing and Visualization in Science*, 4:249–257, 2002. 10.1007/s00791-002-0081-9.

[117] R.C.P. Kerckhoffs, S.N. Healy, T.P. Usyk, and A.D. McCulloch. Computational methods for cardiac electromechanics. *Proceedings of the IEEE*, 94(4):769 –783, 2006.

[118] S.A. Niederer and N.P. Smith. The role of the frank–starling law in the transduction of cellular work to whole organ pump function: a computational modeling analysis. *PLoS computational biology*, 5(4):e1000371, 2009.

[119] J. Kortsmit, N.H. Davies, R. Miller, J.R. Macadangdang, P. Zilla, and T. Franz. The effect of hydrogel injection on cardiac function and myocardial mechanics in a computational post-infarction model. 2012.

[120] S. A. Niederer, P. J. Hunter, and N. P. Smith. A quantitative analysis of cardiac myocyte relaxation: a simulation study. *Biophysical journal*, 90(5):1697–1722, 2006.

[121] A. M. Katz. Ernest henry starling, his predecessors, and the 'law of the heart'. *Circulation*, 106(23):2986–2992, 2002.

[122] B. D. Levine, L. D. Lane, J. C. Buckey, D. B. Friedman, and C. G. Blomqvist. Left ventricular pressure-volume and frank-starling relations in endurance athletes. implications for orthostatic tolerance and exercise performance. *Circulation*, 84(3):1016–1023, 1991.

[123] R.C.P. Kerckhoffs, P.H.M. Bovendeerd, F.W. Prinzen, K. Smits, and T. Arts. Intra- and interventricular asynchrony of electromechanics in the ventricularly paced heart. *Journal of Engineering Mathematics*, 47:201–216, 2003. 10.1023/B:ENGI.0000007972.73874.da.

[124] J. Rijcken, P. H. Bovendeerd, A. J. Schoofs, D. H. van Campen, and T. Arts. Optimization of cardiac fiber orientation for homogeneous fiber strain during ejection. *Ann Biomed Eng*, 27(3):289–97, May-Jun 1999.

[125] M. Abramowitz and I.A. Stegun. *Handbook of mathematical functions with formulas, graphs, and mathematical tables*, volume 55. Dover publications, 1964.

[126] P. M. F. Nielsen, I. J. LeGrice, B. H. Smaill, and P. J. Hunter. Mathematical model geometry and fibrous structure of the heart. *American Journal of Physiology*, 260:H1365–H1378, 1991.

[127] D.D. Streeter JR. Gross morphology and fiber geometry of the heart. *Handbook of physiology: a critical, comprehensive presentation of physiological knowledge and concepts. The cardiovascular system: Formerly Section 2: Circulation. The heart*, 1:61, 1979.

[128] G. Krishnamurthy, D.B. Ennis, A. Itoh, W. Bothe, J.C. Swanson, M. Karlsson, E. Kuhl, D.C. Miller, and N.B. Ingels Jr. Material properties of the ovine mitral valve anterior leaflet in vivo from inverse finite element analysis. *American Journal of Physiology-Heart and Circulatory Physiology*, 295(3):H1141–H1149, 2008.

[129] C. Seiler, T. Pohl, E. Lipp, D. Hutter, and B. Meier. Regional left ventricular function during transient coronary occlusion: relation with coronary collateral flow. *Heart*, 88(1):35–42, 2002.

[130] A. M. Katz. Physiology of the heart, 1977.

[131] P. Lancaster and K. Salkauskas. Surfaces generated by moving least squares methods. *Mathematics of computation*, 37(155):141–158, 1981.

[132] B. Nayroles, G. Touzot, and P. Villon. Generalizing the finite element method: diffuse approximation and diffuse elements. *Computational mechanics*, 10(5):307–318, 1992.

[133] S. Skatulla. *Computational aspects of generalized continua based on moving least square approximations*. PhD thesis, University of Adelaide, 2006.

[134] http://www.gid usa.com/. Gid: The personal pre and post processor.

[135] P. Colli Franzone, L. Guerri, and S. Rovida. Wavefront propagation in an activation model of the anisotropic cardiac tissue: asymptotic analysis and

numerical simulations. *Journal of Mathematical Biology*, 28:121–176, 1990. 10.1007/BF00163143.

[136] D.E. Hansen, G.T. Daughters, E.L. Alderman, NB Ingels, D.C. Miller, et al. Torsional deformation of the left ventricular midwall in human hearts with intramyocardial markers: regional heterogeneity and sensitivity to the inotropic effects of abrupt rate changes. *Circulation research*, 62(5):941–952, 1988.